

UNIVERSITÀ
DI PAVIA

Department of Biology e Biotechnology ‘‘L. Spallanzani’’

Master Degree in Neurobiology

A step towards a directed structural connectome of the human brainstem: from tracer-based anatomical evidence to diffusion tractography

Verso il connettoma direzionale del tronco encefalico umano: dall’anatomia dei traccianti alla trattografia.

Supervisor:
Prof.ssa Fulvia Palesi

Co-supervisors:
Dott.ssa Marta Gaviraghi,
Dott.ssa Eleonora Lupi

Experimental Thesis of
Elisavet Monogioudi

Academic Year 2025-2026

Contents

Abstract 4
Abstract (Italian version) 5

List of abbreviations for the brain regions **7**

1 Introduction **9**
1.1 Brainstem 9
1.1.1 Brainstem anatomy 9
1.1.2 Brainstem functional roles 10
1.2 Magnetic resonance imaging 11
1.3 Diffusion MRI 14
1.3.1 Tractography MRI 15
1.3.2 Limitations of tractography 17
1.4 Graph theory 17

2 Aim **19**

3 Materials and methods **20**
3.1 Study design 20
3.2 Literature review 20
3.2.1 Evidence criteria 20
3.2.2 Structural connectivity of the brainstem 21
3.2.2.1 Red nucleus: magnocellular and parvocellular red nuclei . . . 21
3.2.2.2 Tectum: superior colliculus and inferior colliculus 22
3.2.2.3 Pontine Nuclei: medial, lateral and dorsal pontine nuclei . . . 23
3.2.2.4 Inferior Olivary Complex: principal olive and accessory olives (MAO, DAO) 24
3.2.2.5 Vestibular Nuclei: superior, medial, lateral and inferior vestibular nuclei 25
3.2.2.6 Reticular Formation: midbrain reticular formation and pontis oralis 26

3.2.2.7 Basal Ganglia . . . 27
3.2.2.8 Cerebrum Subcortical Nuclei: amygdaloid complex, claustrum, septal nuclei . . . 28
3.2.2.9 Thalamus . . . 29
3.2.2.10 Hypothalamus . . . 30
3.2.2.11 Periaqueductal Gray . . . 30
3.2.2.12 Locus Coeruleus . . . 31
3.2.2.13 Ventral Tegmental Area . . . 31
3.2.3 Connectivity matrices . . . 31
3.3 Graph theory metrics . . . 35
3.4 Subjects and data . . . 38
3.5 Atlas definition and region segmentation . . . 38
3.6 Tractography extraction methods . . . 40
3.7 Tractography extraction methods comparison . . . 41
3.7.1 Evaluation metrics: Sensitivity, Precision, Specificity . . . 43
3.7.2 Overall performance measures . . . 44
3.7.3 Region volume as reconstruction failure predictor . . . 45

4 Results **46**
4.1 Structural connectivity matrices . . . 46
4.2 Graph theory results . . . 49
4.2.1 Effect of unpacking the pons . . . 50
4.2.2 Degrees and network hubs . . . 52
4.2.3 Betweenness centrality . . . 53
4.2.4 Clustering coefficient, coreness and trophic level . . . 54
4.3 Atlas and segmentation . . . 55
4.3.1 Brain Atlases at 1.5 mm and 0.8 mm isotropic resolution . . . 55
4.3.2 Volume analysis at 1.5 mm and 0.8 mm isotropic resolution . . . 57
4.4 Analysis and comparison across tractography configurations . . . 59
4.4.1 Deterministic tractography analysis . . . 60
4.4.2 No-ACT tractography analysis . . . 61
4.4.3 ACT tractography analysis . . . 62
4.4.4 Default cutoff tractography analysis . . . 63
4.4.5 0.06 cutoff tractography analysis . . . 64
4.4.6 Dynamic seed tractography analysis . . . 65
4.4.7 0.8 mm resolution tractography analysis . . . 66
4.4.8 Region volume as reconstruction failure predictor analysis . . . 68

5 Discussion **70**

5.1 Building an anatomically grounded brainstem connectome 71
5.2 Emerging nodes from graph theory 72
5.3 How resolution limits the definition of small brainstem nuclei 73
5.4 Choosing the proper tractography configuration based on performance 73
5.5 Limitations 74
5.6 Future perspectives 75

6 Conclusions **77**

Acknowledgements **78**

References **79**

Abstract

The brainstem is a structurally and functionally complex region of the human brain, containing numerous nuclei that give rise to widespread neuromodulatory and sensorimotor projections, reaching not only other brainstem nuclei but the whole brain, targeting cortical, subcortical and cerebellar regions. Its in-vivo connectivity can be investigated using diffusion MRI tractography that allows white-matter pathways to be reconstructed. However, the small size and dense packing of the brainstem nuclei make their connectivity challenging to reconstruct. Furthermore, an intrinsic limitation of tractography is that it is undirected, meaning that it is unable to identify the way a connection runs between two regions, resulting in symmetric connectivity matrices (i.e., connectomes). To address these limitations, this work aimed to build a directed, anatomically-informed, structural connectome of the brainstem and to use it as reference to quantify how faithfully diffusion tractography reconstructs brainstem connectivity.

To reach the first main goal, the reference structural connectome of the brainstem was assembled capturing intrinsic brainstem connectivity as well as its connectivity with other subcortical structures. The evidence used, derived from an extensive literature review of viral tracing studies conducted in humans, non-human primates and rodents. The resulting directed connectome of the brainstem was then characterized using graph theory measures, which demonstrated that it captures biologically meaningful roles, distinguishing neuromodulatory output hubs such as the locus coeruleus and relay hubs such as the periaqueductal gray and ventral tegmental area.

Furthermore, to evaluate the second aim and quantify the reliability of tractography reconstructions, a subject-specific atlas was built at two different isotropic resolutions (1.5 mm and 0.8 mm) and seven diffusion tractography configurations were compared against the previously assembled reference connectome. These seven configurations differed in their anatomical constraints and reconstruction parameters, such as the use of anatomical constraints (ACT vs no-ACT), the FOD amplitude threshold below which streamline tracking is terminated (0.05 vs 0.06), the seeding strategy (gray matter-white matter interface vs dynamic), the tracking algorithm (probabilistic vs deterministic) and the voxel resolution (1.5 vs 0.8 mm). Two tractography configurations stood out, depending on whether the goal was to recover the largest number of true connections or to achieve the best balance between true and false positive connections. The tractography configuration with the default cutoff (FOD = 0.05) recovered the largest number of true positive connections (63.89%). On the other side the configuration using dynamic seeding gave the best balance between true and false positive connections. Across all configurations, the smallest nuclei were continuously under-reconstructed, with region size emerging as a possible predictor of reconstruction failure.

Together, these results provide an anatomically grounded reference for the brainstem connectome preserving the connection directionality that tractography cannot recover and a quantitative assessment of how faithfully tractography reproduces it.

Abstract (Italian version)

Il tronco encefalico è una regione del cervello umano caratterizzata da un'elevata complessità strutturale e funzionale. Contiene numerosi nuclei da cui originano estese proiezioni neuromodulatorie e sensorimotorie, che raggiungono sia altri nuclei del tronco encefalico sia regioni corticali, sottocorticali e cerebellari. La sua connettività può essere studiata *in vivo* mediante la trattografia basata sulla risonanza magnetica di diffusione, che consente di ricostruire i tratti assonali della sostanza bianca. Tuttavia, le ridotte dimensioni dei nuclei del tronco encefalico e la loro stretta prossimità anatomica rendono difficoltosa la ricostruzione delle loro connessioni. La trattografia, inoltre, non consente di stabilire la direzione delle connessioni tra due regioni e restituisce quindi matrici di connettività simmetriche. Per affrontare queste limitazioni, il presente lavoro si è proposto di costruire un connettoma strutturale orientato del tronco encefalico, basato su evidenze anatomiche, e di utilizzarlo come riferimento per quantificare la fedeltà con cui la trattografia ricostruisce la connettività.

Per conseguire il primo obiettivo, è stato costruito un connettoma strutturale di riferimento che include sia le connessioni interne al tronco encefalico sia quelle con altre strutture sottocorticali. Le evidenze utilizzate sono state ricavate da un'ampia revisione della letteratura relativa a studi di tracciamento virale condotti nell'uomo, nei primati non umani e nei roditori. Il connettoma orientato così ottenuto è stato quindi caratterizzato mediante misure di teoria dei grafi. Queste analisi hanno mostrato che il connettoma riflette ruoli biologicamente significativi, distinguendo hub di efferenza neuromodulatoria, come il locus coeruleus, e hub di relais, come la sostanza grigia periacqueduttale e l'area tegmentale ventrale.

Per conseguire il secondo obiettivo e quantificare l'affidabilità della trattografia, è stato impiegato un atlante specifico per un soggetto a due diverse risoluzioni isotrope (1,5 mm e 0,8 mm), e sette configurazioni di trattografia sono state confrontate con il connettoma di riferimento precedentemente costruito. Le configurazioni differivano per i vincoli anatomici e i parametri di ricostruzione: la presenza o l'assenza di vincoli anatomici (ACT vs no-ACT), la soglia di ampiezza della distribuzione degli orientamenti delle fibre (FOD) al di sotto della quale viene interrotta la propagazione delle streamline (0,05 vs 0,06), la strategia di inizializzazione delle streamline, o seeding (interfaccia materia bianca-materia grigia vs dinamica), l'algoritmo di tracciamento (probabilistico vs deterministico) e la risoluzione dei voxel (1,5 mm vs 0,8 mm). Due configurazioni si sono distinte, a seconda che l'obiettivo fosse ricostruire il maggior numero di connessioni vere oppure ottenere il miglior equilibrio tra veri positivi e falsi positivi. La configurazione con la soglia FOD predefinita di 0,05 ha ricostruito il maggior numero di connessioni vere positive (63,89%). La configurazione con seeding dinamico ha invece mostrato il miglior equilibrio tra veri positivi e falsi positivi. In tutte le configurazioni, la connettività dei nuclei più piccoli è risultata sistematicamente sottorappresentata nelle ricostruzioni, e le dimensioni delle regioni sono emerse come un possibile fattore predittivo della mancata ricostruzione delle

connessioni anatomiche.

Nel complesso, questi risultati forniscono un connettoma di riferimento del tronco encefalico basato su evidenze anatomiche, che integra la direzionalità delle connessioni, non direttamente ricavabile dalla trattografia, e una valutazione quantitativa della capacità con cui la trattografia riproduce la connettività anatomica.

List of abbreviations for the brain regions

Brainstem

RN	Red Nucleus
RNp	Red Nucleus, parvocellular
RNm	Red Nucleus, magnocellular
SNc	Substantia Nigra pars compacta
SNr	Substantia Nigra pars reticulata
SC	Superior Colliculus
IC	Inferior Colliculus
PAG	Periaqueductal Grey
VTA	Ventral Tegmental Area
LC	Locus Coeruleus
mRT	Mesencephalic (Midbrain) Reticular Formation
PnO	Pontine Reticular Nucleus, oral part (Pontis Oralis)
PN	Basilar Pontine Nuclei
PNm	Pontine Nuclei, medial
PNl	Pontine Nuclei, lateral
PNd	Pontine Nuclei, dorsal
NRTP	Nucleus Reticularis Tegmenti Pontis
PPN	Pedunculopontine Tegmental Nucleus
LDT	Laterodorsal Tegmental Nucleus
PB	Parabrachial Nucleus
RNPON	Raphe Nucleus Pontis
CSR	Central Superior Raphe Nucleus
SOC	Superior Olivary Complex
ION	Inferior Olivary Nucleus
PO	Principal Olive
MAO	Medial Accessory Olive
DAO	Dorsal Accessory Olive
Ve	Vestibular Nuclei
VNs	Superior Vestibular Nucleus
VNm	Medial Vestibular Nucleus
VNl	Lateral Vestibular Nucleus
VNi	Inferior Vestibular Nucleus
CN	Cochlear Nucleus
TPS	Trigeminal Principal Sensory Nucleus

TM	Trigeminal Motor Nucleus
ABD	Abducens Nucleus
FM	Facial Motor Nucleus
SSal	Superior Salivatory Nucleus

Thalamus

Thal_AV	Anteroventral nucleus
Thal_LDP	Laterodorsal / Lateral Posterior (LD, LP)
Thal_VA	Ventral Anterior
Thal_VLA	Ventral Lateral Anterior
Thal_VLP	Ventral Lateral Posterior
Thal_VPL	Ventral Posterolateral
Thal_IntR	Intralaminar, rostral (CeM, CL)
Thal_IntC	Intralaminar, caudal (CM, PF)
Thal_MDm	Mediodorsal, medial magnocellular
Thal_MDl	Mediodorsal, lateral parvocellular
Thal_LGn	Lateral Geniculate nucleus
Thal_MSGn	Medial Geniculate / Suprageniculate
Thal_PulA	Pulvinar, anterior
Thal_PulI	Pulvinar, inferior
Thal_PulL	Pulvinar, lateral
Thal_PulM	Pulvinar, medial
Thal_MV(Re)	Reuniens (medioventral)
Thal_L-Sg	Limitans–Suprageniculate

Basal ganglia and other subcortical nuclei

Caud	Caudate Nucleus
Puta	Putamen
Pall	Pallidum
Gpi	Globus Pallidus, internal
Gpe	Globus Pallidus, external
Accu	Nucleus Accumbens
Subthal	Subthalamic Nucleus
Amyg	Amygdala
Hippo	Hippocampus
Claus	Claustrum
Septal	Septal Nuclei
Hypo	Hypothalamus

Cerebellum

Cbm	Cerebellum (cortical lobules I-X, Crus I-II, and vermis VI-X)
Dentate	Dentate nucleus
Interposed	Interposed nucleus
Fastigial	Fastigial nucleus

Chapter 1

Introduction

1.1 Brainstem

1.1.1 Brainstem anatomy

The brainstem is a structure located at the caudal portion of the brain which connects the cerebral hemispheres and diencephalon to the spinal cord and cerebellum [1]. It occupies the posterior cranial fossa and lies ventral to the cerebellum, to which it is joined by the superior, middle, and inferior cerebellar peduncles, and it continues rostrally to the diencephalon and caudally to the spinal cord at the level of the foramen magnum [2]. Despite its small volume, the brainstem contains a rather high density of functionally critical structures, including some of the nuclei of cranial nerves, the ascending and descending white matter tracts, and the reticular formation. Anatomically, the brainstem is typically divided into three main levels, that are depicted in Figure 1.1. The midbrain, alternatively known as mesencephalon, is the most rostral part of the brainstem. It includes the tectum, which contains the superior and inferior colliculi and the cerebral aqueduct, which connects the third and fourth ventricles, and is surrounded by the periaqueductal gray (PAG), and the tegmentum, which contains white matter tracts, the nuclei of the oculomotor (III) and trochlear (IV) cranial nerves, the substantia nigra, the red nucleus, the ventral tegmental area, and the reticular formation, which includes the raphe (dorsal raphe nucleus) and cuneiform nuclei.

The pons connects the cerebrum to the cerebellum, and it consists of a ventral basilar portion and a dorsal tegmentum. The ventral portion contains longitudinal fibres originating mainly from the corticospinal, corticobulbar and corticopontine tracts. The pontine nuclei are contained also in the ventral portion, forming the main link between the cerebral cortex and the contralateral cerebellum via the middle cerebellar peduncle [2][3].

The dorsal portion contains the nuclei of several cranial nerves including the trigeminal (V), abducens (VI), facial (VII) and vestibulocochlear (VIII) nerves, and the superior olivary complex.

Additionally, it is largely occupied by the pontine reticular formation, a structure that includes the parabrachial nuclei, nucleus reticularis pontis oralis, the laterodorsal tegmental nucleus, the raphe nuclei, the pedunculopontine tegmental nucleus and the locus coeruleus [2][3].

It also contains tracts of white matter including the medial longitudinal fasciculus, the medial lemniscus, the lateral lemniscus, the spinothalamic tract, the central tegmental tract, and the trapezoid body[4].

Lastly, the medulla oblongata, the most caudal segment, is classically divided into a ventral and a dorsal portion. The ventral part of the medulla oblongata includes the pyramids and the olives. The dorsal portion contains the nuclei of several cranial nerves. In detail the glossopharyngeal nerve (IX), the vagus nerve (X), the accessory nerve (XI), and the XII hypoglossal nerve (XII). This portion also contains the continuation of major ascending and descending white matter tracts, including the medial longitudinal fasciculus, the medial lemniscus, the spinothalamic tract, the central tegmental tract, and the spinocerebellar pathways [4].

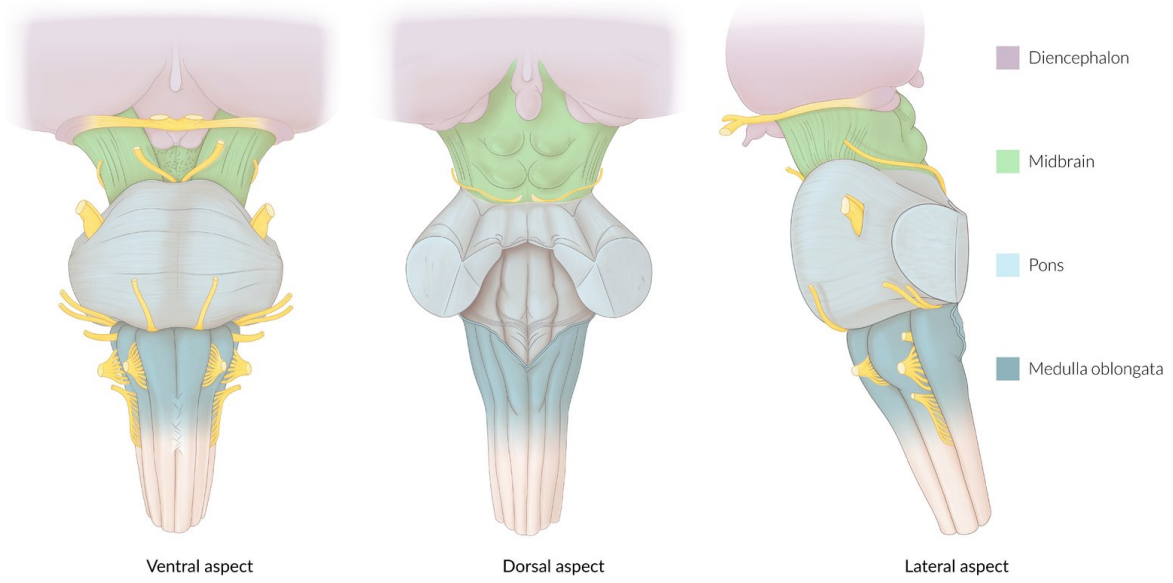


Figure 1.1: Anatomy of the human brainstem. Ventral, dorsal and lateral views of the brainstem, color-coded by subdivision: diencephalon with purple, midbrain with green, pons with light blue and medulla oblongata with teal. The attached cranial nerves are shown in yellow. Figure adapted from AMBOSS ”Brainstem”, https://www.amboss.com/us/knowledge/brainstem

1.1.2 Brainstem functional roles

Functionally, the brainstem acts both as a relay station and as an intrinsic control center [1]. As a relay station, it transmits ascending sensory information and descending motor commands exchanged between the cerebral cortex and the spinal cord. Through the cranial nerve nuclei, it also provides the sensory and motor innervation of the head and neck, mediating functions such as eye movements, facial expression, mastication, hearing, and balance [1]. Beyond these

functions, the brainstem contains centers that are essential for survival. Autonomic nuclei in the medulla and pons help regulate cardiovascular and respiratory activity, while the reticular formation controls arousal, the sleep-wake cycle, and the maintenance of consciousness through the ascending reticular activating system (ARAS) [1][5][6]. The brainstem is also the origin of the major neuromodulatory systems that shape the activity of the entire brain. More specifically, those modulatory systems include the dopaminergic neurons of the substantia nigra and ventral tegmental area, the noradrenergic neurons of the locus coeruleus, the serotonergic neurons of the raphe nuclei, and the cholinergic neurons of the pedunculopontine and laterodorsal tegmental nuclei [1] [5].

1.2 Magnetic resonance imaging

Magnetic resonance imaging (MRI) is a non-invasive biomedical imaging technique that produces detailed images of the subject's body without using ionizing radiation. It is widely used in both clinical diagnosis and neuroscience research. It exploits the magnetic properties of certain atomic nuclei that are present in biological tissues in the body. While many atomic nuclei can produce signal, the hydrogen nucleus, or proton, is the most commonly used nucleus due to its abundance in the human body. Approximately 70% of the human body consists of water molecules that are composed by one oxygen and two hydrogen atoms, making hydrogen a well distributed source of signal for the MRI [7].

Atomic nuclei consist of protons and neutrons and therefore carry a net positive charge, determined by the number of protons. Each proton possesses magnetic properties that arise from its electrical charge and its intrinsic angular momentum, known as spin. The magnitude of the spin depends on the spin quantum number that is specific for each nucleus. Nuclei with odd number of protons have non-null spin quantum number, that allows to induce a magnetic moment that locally interacts with other magnetic fields. In case of the proton, its spin quantum number is equal to ½ [7].

In the absence of an external magnetic field, the magnetic moments of the protons are randomly oriented, resulting in no net tissue magnetization. However, when the protons are exposed to a strong, static magnetic field, usually known as B_0, the magnetic moments tend to align with its direction, either parallel or anti-parallel to it. In the quantum-mechanical description, these two orientations correspond to the energy states. The parallel orientation corresponds to a slightly lower energy state and is marginally more populated, and this small excess of protons aligned with the field produces a net magnetization of the tissue along the direction of B_0 [7].

At the same time, the protons do not remain still but rotate, or precess, around the axis aligned to the magnetic field B_0, as shown in Figure 1.2. The frequency of this precession is called the Larmor frequency, and it depends on the strength of the applied magnetic field, according to

the Larmor equation: $\omega = \gamma B_0$, where γ is the gyromagnetic ratio, a constant specific to each nucleus [7]. This relationship is fundamental to MRI, because the protons can be selectively excited only by a signal oscillating at their own Larmor frequency.

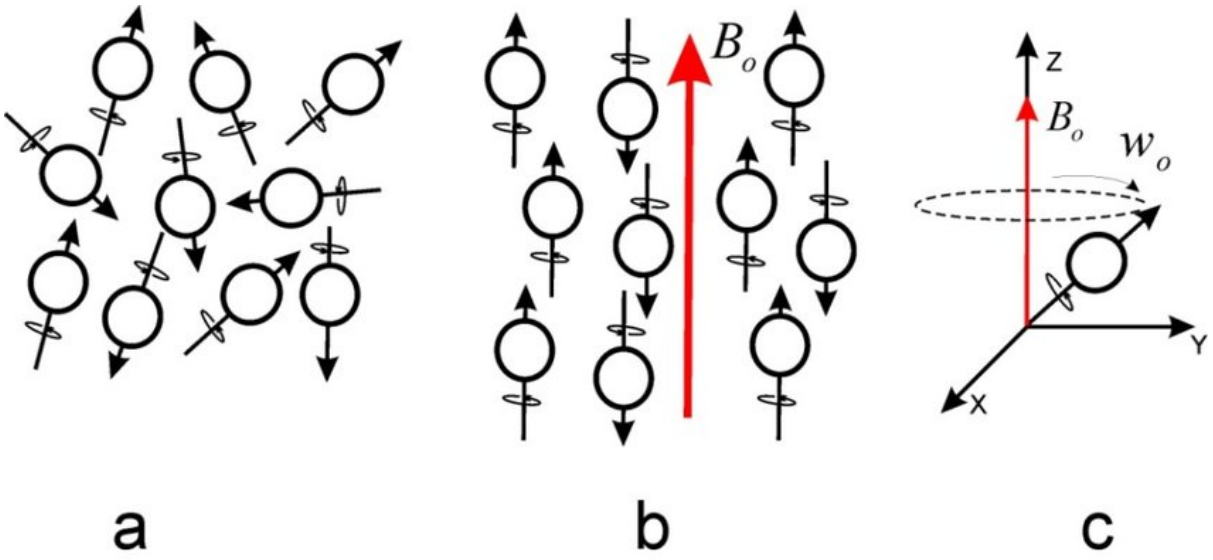


Figure 1.2: Behaviour of proton magnetic moments (spins) in a magnetic field. (a) In the absence of an external magnetic field, the magnetic moments are randomly oriented, producing no net tissue magnetization. (b) Under a strong static field B_0, the moments align either parallel or anti-parallel to it; the small excess in the lower-energy parallel state yields a net magnetization along B_0. (c) Each proton precesses around the axis of B_0 at the Larmor frequency ω_0.

To generate a measurable signal, a radiofrequency (RF) pulse tuned to the Larmor frequency is applied. The pulse excites the spins and tips the net magnetization away from the direction of B_0, into the transverse plane. Once the RF pulse is switched off, the protons gradually return to their original equilibrium state, and in doing so, they release the absorbed energy as a radiofrequency signal that is detected by the receiver coils of the scanner. The magnetization relaxation is described by two tissue-specific times. The longitudinal relaxation time, T1, describes how quickly the magnetization realigns with the direction of B_0, while the transverse relaxation time, T2, describes how quickly the transverse magnetization decays in the plane perpendicular to it [7]. Different tissues are characterized by different T1 and T2 values, and this difference is the main source of contrast between them. By adjusting the acquisition parameters on the scanner, the same anatomy can be represented with different weightings. For example, T1-weighted images provide sharp anatomical detail and a clear separation between grey and white matter. T2-weighted images are sensitive to the water content of tissues, so that fluids and many pathological lesions appear bright. FLAIR (Fluid-Attenuated Inversion Recovery) images suppress the signal from the cerebrospinal fluid, thus improving the visibility of lesions located near the ventricles or near the cortex. The visual differences can be seen in Figure 1.3.

Finally, in order to form an image, the spatial origin of the signal within the body must be identified and then encoded. This is achieved by applying magnetic field gradients, controlled

variations whose amplitude varies linearly with position along a chosen axis, on top of the main magnetic field. This causes the spins to precess at position-dependent frequencies. Because the frequency of the protons' precession is proportional to the magnetic field they experience, these gradients make protons at different positions precess at slightly different frequencies and eventually obtain different phases. In this way, the spatial position can be encoded into the frequency and phase of the emitted signal. The spatially encoded signals are not stored immediately into an image. Instead, they are recorded in an intermediate domain known as k-space. Then, an inverse Fourier transformation is applied to convert this frequency information into the final spatial image. K-space is a frequency domain in which each point corresponds to a particular spatial frequency of the image. The central points of k-space carry information about the broad, low-frequency structure of the image, while the outer points carry the fine detail. Once k-space has been filled, an inverse Fourier transform, a mathematical operation that converts frequency information into spatial information, is applied to reconstruct the final image. The reconstructed image is composed of a regular grid of elementary units called voxels, each representing a small three-dimensional volume of tissue. The signal intensity assigned to a voxel corresponds to the average magnetic resonance signal originating from all the protons contained within that volume [7].

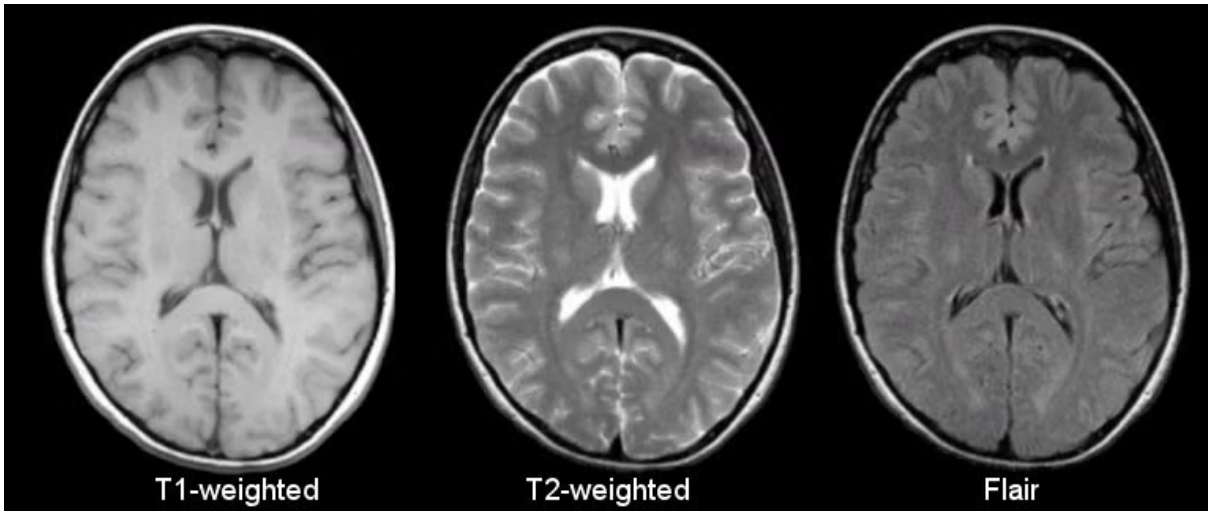


Figure 1.3: Example of different MRI contrasts of the same axial brain slice. From left to right: T1-weighted, T2-weighted and FLAIR images. The same anatomy appears markedly different depending on the acquisition parameters.

1.3 Diffusion MRI

Diffusion MRI (dMRI) is a magnetic resonance technique that generates image contrast based on the microscopic motion of water molecules within tissues, known as Brownian motions. Water molecules undergo displacements over distances of only a few micrometers and interact with tissue barriers, thus providing indirect information about tissue architecture at a scale below that of a voxel.

To make the signal sensitive to diffusion, a pair of diffusion sensitizing gradients are applied. The first gradient introduces a position-dependent phase shift in the precessing protons, marking their location, while the second gradient is designed to reverse this phase shift. Protons that have remained stationary between the two gradients experience no net phase change and contribute fully to the signal. In contrast, protons that have moved between the two gradients are no longer in the same position, so the reversal is incomplete, so they acquire a residual phase. These residual phases reduce the phase coherence within the voxel, and therefore attenuate the signal. The signal is reduced in proportion to the distance the water molecules have traveled, and the degree of this diffusion weighting is controlled by an acquisition parameter called the b-value [8].

With diffusion, we are able to distinguish different brain tissues. In cerebrospinal fluid, water diffuses equally in all directions (isotropic diffusion). In white matter, however, the axonal membranes and the myelin constrain the movement of water (anisotropic diffusion). The simplest model, the diffusion tensor imaging (DTI), represents the diffusion in each voxel as a tensor, visualized by an ellipsoid whose main axis indicates the dominant diffusion direction as shown in figure (1.4).

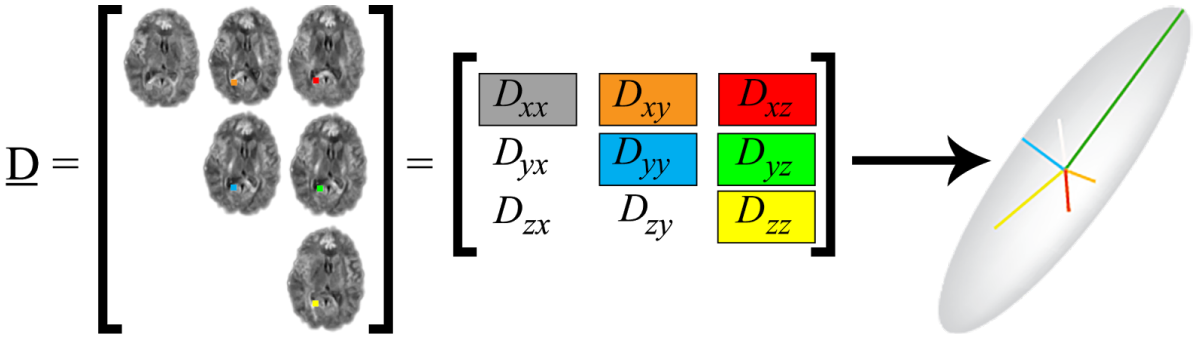


Figure 1.4: Diffusion tensor model: In each voxel the movement of the water is described by a 3×3 matrix, the diffusion tensor D, whose values measure how much water diffuses along and between the three directions in space. Solving this matrix gives three eigenvectors and eigenvalues, which can be drawn as an ellipsoid. Each eigenvector describes the direction of an axis and its eigenvalue describes the axis length. The longest axis points in the direction in which water moves most easily, which matches the main fiber direction inside that voxel.

However, the tensor model can represent only one fiber orientation per voxel and for this reason fails wherever fibers cross, merge, or diverge. To overcome this crucial problem, constrained spherical deconvolution (CSD) models have been introduced. Rather than representing diffusion

as a single tensor, CSD models estimate for each voxel, a fiber orientation distribution (FOD). FOD describes how fiber material is oriented within the voxel. FOD typically shows one or more distinct peaks. In detail, each peak of the FOD points along the orientation of one fiber population that passes through the voxel. Consequently, CSD models can identify multiple fiber orientations inside a single voxel, including in regions where fibers cross, which the simple tensor model could not [8].

1.3.1 Tractography MRI

Tractography is the computational process that uses the fiber orientation information contained from diffusion data to reconstruct the trajectories of white-matter pathways. Starting from a set of seed points, the algorithm follows the estimated fiber orientations, either from DTI or most commonly from CSD, from each voxel to another voxel, generating three-dimensional curves called streamlines that represent the plausible axonal bundles [8].

Two main strategies of tractography exist. Deterministic tractography follows the main direction of diffusivity for each voxel (i.e., the principal eigenvector of the tensor in DTI, or the dominant FOD peak in the CSD model), whereas probabilistic tractography repeatedly samples from the orientation distribution, better representing uncertainty and reconstructing complex or minor pathways.

Independently of the tractography method used, one main decision point is which fibres must be accepted and which discarded, but also where the fibers actually terminate. The main criteria that are used are: a minimal threshold to the fractional anisotropy signal, a local curvature below a certain threshold to avoid fibers' U-turn and lastly a binary tracking mask to exclude regions in which fibers cannot be present.

Anatomical information can also constrain the process through a technique called anatomically constrained tractography (ACT). From a T1-weighted image, tissue-type segmentation is obtained with the MRtrix3 command ‘‘5ttgen’’, which classifies brain tissue in four different types: white matter (WM), cortical and subcortical grey matter (GM), and cerebrospinal fluid (CSF). It is possible also to manually add a fifth tissue type constituted of pathological regions [9]. ACT starts from the prior that fibers should terminate in gray matter structures, except for those that pass through the brainstem to reach the spinal cord; therefore, they should never end within white matter, as well as enter cerebrospinal fluid. ACT terminates the fibers based on six principles, also shown in Figure 1.5:

1. If a streamline enters cortical gray matter, it has reached a valid termination point because gray matter is a biologically plausible termination site.

2. If a streamline enters cerebrospinal fluid (CSF), for example within the ventricles, it is rejected.

3. If a streamline exits the current diffusion image or a pre-determined tracking mask, it is

terminated and accepted. This criterion is used to project streamlines to spinal cord.

4. If a streamline terminates in a white matter region due to pre-determined thresholds for FA signal or allowed curvature, it is rejected, as termination within the white matter is not considered plausible .

5. If a streamline is terminated due to point 4 in sub-cortical gray matter, it is accepted in order to avoid its termination at the boundaries of sub-cortical structures.

6. If a streamline enters a sub-cortical structure, it is not allowed to exit.

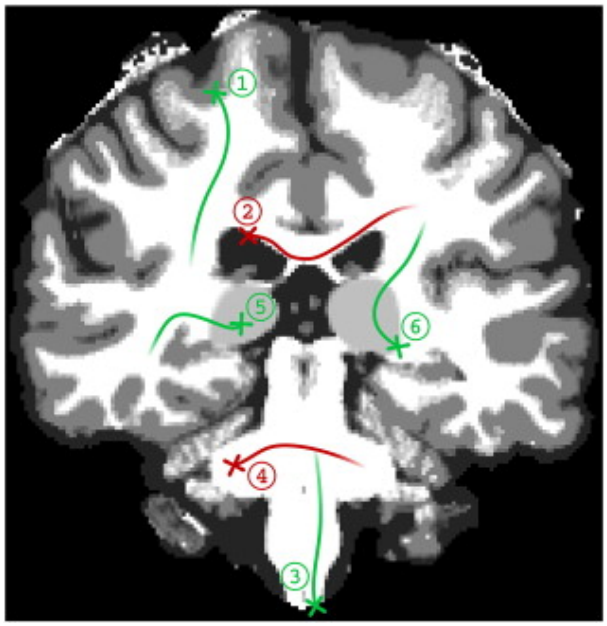


Figure 1.5: Visual demonstration of anatomical priors used for Anatomically Constrained Tractography (ACT) shown upon a coronal slice. Crosses indicate termination points of example streamlines. Green streamlines are accepted, red streamlines are rejected. The numbers refer to the ACT criteria explained in the text. Figure from [10]

Once a streamline is terminated and rejected, the outcome depends on the tractography algorithm used. In a deterministic tractography algorithm, each streamline follows a single fiber orientation at every step, meaning that it traces one predetermined trajectory. If a streamline is rejected, it is discarded entirely while no alternative path can be retrieved. Instead, with a probabilistic tractography, it is possible to back-track the fiber and re-evaluate the uncertainty to find a more suitable path. Therefore, when a streamline is rejected, the algorithm retraces its most recent segment and re-traces, repeating this until either all possible alternatives have been rejected or an anatomically valid path is eventually found [10].

By repeating this streamline generation process from a large number of seed points that are distributed throughout the brain, a whole set of streamlines is produced, also known as tractogram. Each streamline approximates the trajectory of an underlying white matter fiber bundle, and together they form a three dimensional reconstruction of the brain's structural pathways. Then these reconstructed tracts can be overlaid on the subject's anatomical (T1-weighted) image to visualize the pathways in their anatomical context, as shown in Figure 1.6.

Tractography results are organized into a structural connectivity matrix, representing the brain connectome. Each value in the matrix indicates the strength of connection between a pair of brain regions. The rows and columns correspond to the brain regions of interest, called nodes, while the intersections between columns and rows define the connections between the regions, called edges. The structural connectivity matrix can be labeled with a color code that weights the connections on the number of streamlines connecting pairs of nodes. Since on both columns and rows there are the same regions in the same order, the main diagonal corresponds to the connections between a region and itself and it contains all zeros.

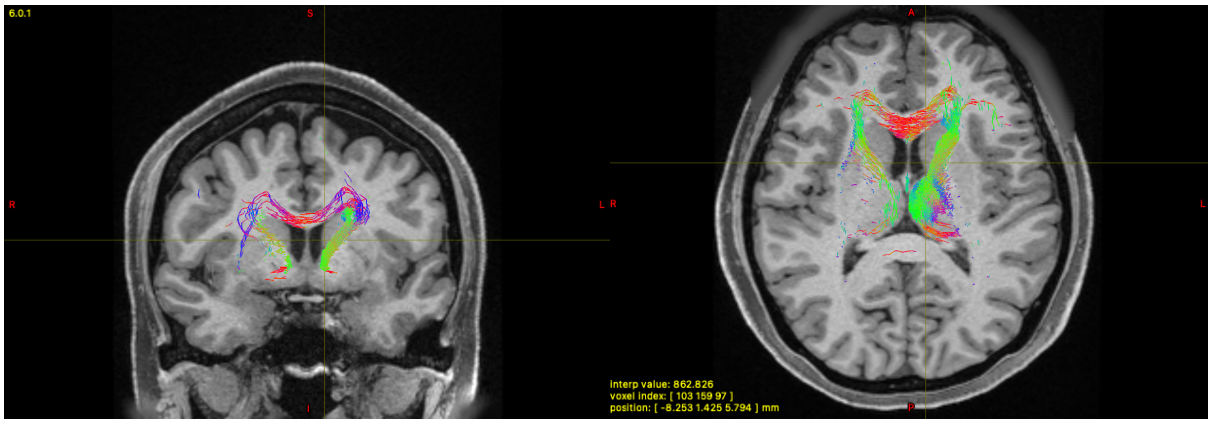


Figure 1.6: Example of reconstructed streamlines overlaid on the subject's T1-weighted image, shown in coronal (left) and axial (right) views. Each color represents an orientation of the fibers reconstructed between brain regions in MrView.

1.3.2 Limitations of tractography

Despite its foundational role, structural connectivity derived from tractography suffers from two limitations that are particularly important. The first limitation is symmetry: while diffusion MRI tractography is able to reconstruct white matter pathways, it does not provide information about the directionality of the pathway, so dMRI connectomes are intrinsically undirected and are represented as symmetric matrices, even though the underlying circuitry is asymmetric in fiber density, projections target and laterality. The second is poor specificity: whole brain tractography generates large numbers of false positive streamlines, and validation work has shown that anatomically implausible connections can be as frequent as true ones, dominating the reconstructed networks.

1.4 Graph theory

The reconstruction of the connections between brain regions ultimately produces a network, and in order to study a network in a quantitative way a dedicated mathematical formalism is needed. This formalism is provided by graph theory, a branch of mathematics that focuses on describing

systems made of many interacting elements. Graph theory has become a general framework for analyzing complex networks of every kind, from social and computer networks to biological systems. Its central idea is simple: any system of interconnected elements can be represented as a graph, in which the elements are called nodes and the links between them edges, Figure 1.7. Over the past two decades, this framework has been increasingly applied to the study of the brain, giving rise to the field of network neuroscience [11]. The main idea is that the brain is not a collection of independent regions but a deeply interconnected system, and many of its properties, under physiological and pathological conditions, arise from the pattern of connections rather than from any single region in isolation. By representing the brain as a graph, in which nodes correspond to anatomical regions and edges to the structural or functional connections between them, graph theory allows the organization of the brain to be studied quantitatively. In this context, the structural connectomes obtained from diffusion MRI tractography provide a natural input for graph-based analysis. Once the connections between regions have been reconstructed, they can be treated directly as the edges of a brain graph [12].

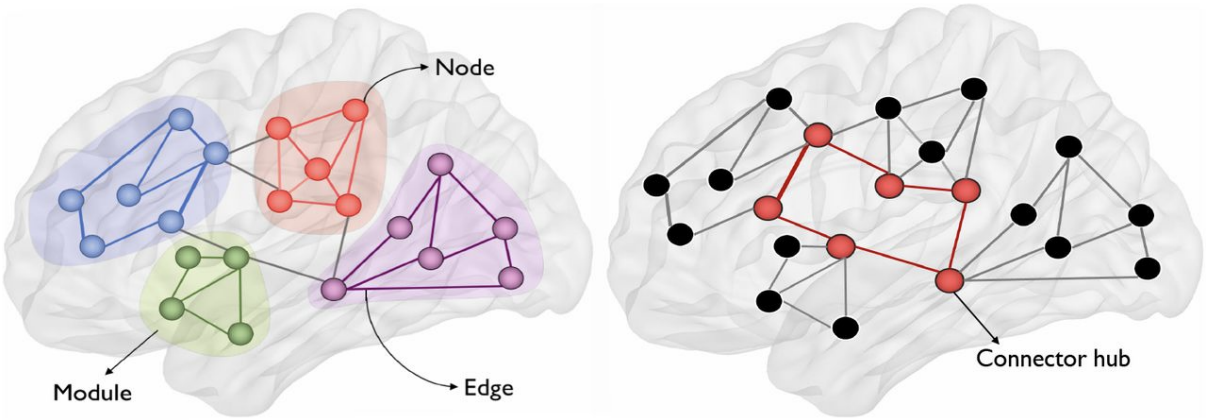


Figure 1.7: Brain representations as a graph. On the left, the brain is modeled as a set of nodes joined by edges and groups of densely interconnected nodes that form modules. On the right, a connector hub is a highly connected node that links different modules and integrates information across the whole network. Adapted from [13]

The value of this approach lies in the quantitative measures, or metrics, that graph theory provides. Rather than describing connectivity qualitatively, these metrics assign numerical values that summarize how the network is organized, either as a whole or region by region. They can reveal, for example, which regions act as highly connected hubs, Figure 1.7, which serve as relays between different parts of the network, and how the connections are distributed and integrated across the brain. This makes it possible to characterize a connectome objectively, to compare different networks with one another, and to detect how changes in connectivity are reflected in the overall organization of the brain [12].

Chapter 2

Aim

Most of the existing brain connectivity models assume symmetry of structural connections among different brain areas. This is an oversimplification of the true structural organization of the human brain. In fact, structural connectivity is asymmetric, indicating differences in fiber density, tract length, and inter-region projections. It is thus essential to capture and map out this asymmetry in order to build a matrix that is both biologically and structurally accurate and realistic. The main purpose of this work is to create a non-symmetric connectivity matrix that accurately depicts the direct connections between various brain areas, focusing on the brainstem.

The second aim of this work is to use this anatomically derived matrix as a reference in order to evaluate different diffusion MRI tractography configurations. Since tractography is prone to reconstructing anatomically implausible connections, especially in a region as small and densely organized as the brainstem, several tractography configurations are compared to determine which most faithfully reproduces the reference connectivity, both across the whole brain and within the brainstem specifically, and to identify which structures remain difficult to reconstruct.

Together, these two scopes will provide a directed anatomically accurate model of the brainstem connectivity and an assessment of how reliably current diffusion tractography can recover it. This is a step towards establishing a foundation for more anatomically informed connectome reconstruction and, potentially for more reliable biophysical modeling of whole-brain dynamics.

Chapter 3

Materials and methods

3.1 Study design

This thesis work aimed to develop a computational pipeline that combines literature based anatomical references with diffusion MRI tractography data, firstly in order to produce an anatomically accurate and directed structural connectivity matrix and secondly to evaluate and compare the anatomical accuracy of different tractography strategies for reconstructing the connectivity of the brainstem. The study was organized into three parts. In the first part, a systematic literature review of tracer-based anatomical studies was carried out, with the purpose to define the connections between the regions of interest and to encode them into a binary directed connectivity matrix, which then served as the anatomical reference. Then, from the resulting matrix, several graph-theory metrics were computed. In the second part, diffusion MRI data from a healthy subject were used in order to reconstruct the tracts between several brainstem regions. Several different tractography configurations were tested, differing in their parameters such as the seeding strategy, the use of anatomical constraints, or the stopping criteria. In the third part, the tractography-derived connectomes were compared by quantifying the connections missing with respect to the anatomical reference, in order to assess how faithfully each configuration reproduced the expected connectivity.

3.2 Literature review

3.2.1 Evidence criteria

A systematic literature search was conducted on various databases with scientific papers such as PubMed and Google Scholar while using keywords such as ‘‘structural connectivity’’, ‘‘tractography’’, ‘‘anatomical projections’’, ‘‘human’’, and the region of interest for instance ‘‘pontine nuclei’’, ‘‘red nucleus’’ or ‘‘substantia nigra’’. Only studies providing direct anatomical evi-

dence were included; diffusion-based findings were considered solely as supporting evidence. Preference was given to human studies or primate data; rodent data were used when higher-level evidence was missing. For consultation about the anatomical structure of the brainstem region, many classical neuroanatomy references were used.

3.2.2 Structural connectivity of the brainstem

The structural connectivity matrix is binary and each connection in the matrix was defined as follows: the number 1 was used to indicate a present structural connection while with 0 were marked where no evidence of structural connection existed. In the matrix, rows represent structures that send projections, while columns indicate structures that receive them. Regions that send projections are characterized as efferent projections. Regions that receive projections are characterized as afferent projections. The subcortical interconnections are not considered in this work. Moreover the abbreviations mentioned throughout this work are named in the appendix.

3.2.2.1 Red nucleus: magnocellular and parvocellular red nuclei

Red nucleus (RN) is a midbrain structure with two well-distinct subdivisions. It is divided into I) the magnocellular Red Nucleus (RNm), located in the caudal region and composed mainly of large neurons; II) the parvocellular Red Nucleus (RNp), located in the rostal region of the RN and composed of small to medium sized neurons. The parvocellular division of the RN is particularly prominent in the adult human brain and may play a role in cognitive-motor function, while the magnocellular RNn demonstrates functional relevance in early development through primitive movements and becomes less functionally significant with aging [14].

Efferent projections from the RN

RNp projects to the ipsilateral inferior olivary complex including principal olive (PO), medial accessory olive (MAO) and dorsal accessory olive (DAO), through the central tegmental tract. These connections form part of the Guillain-Mollaret triangle, responsible for motor learning and coordination [2][15]. RNm sends ipsilateral efferent projections to the midbrain reticular formation (mRT), through the rubroreticular fibers [16]. Additionally, the parvicellular part of the RN directly projects to the vestibular nuclei (VN) [17] while both parvocellular and magnocellular parts of the RN project contralaterally to the pontis oralis (POr) [18]. Connectivity with the thalamus (Th) has been disputed, with mammals not showing any direct projections from the RN to the Th. Lastly, the RNm projects directly and bilaterally to the Ventral Tegmental Area (VTA) through anatomical tracer studies run in mice models. These studies showed that glutamatergic neurons innervate VTA dopamine neurons, as a part of behavioral rewarding system [19].

Afferent projections to the RN

The RN receives direct ipsilateral input from the SC, primarily through tectorubral fibers originating from the deep layers of the tectum (Tt) [20].

3.2.2.2 Tectum: superior colliculus and inferior colliculus

The tectum (Tt) is located in the dorsal part of the midbrain and is divided into two structures: I) the Superior Colliculus (SC), situated beneath the pineal gland and above the cerebral aqueduct and II) the Inferior Colliculus (IC) which is located directly below the SC. Both subdivisions of the Tt serve as a major sensory motor integration center. SC is related to visual processing and movements of orientation and its evolutionarily conserved among all vertebrates [21], while IC is the principal auditory relay station in the midbrain and contributes to reflex movements in response to acoustic stimuli.

Efferent projections from the Tt

SC and IC have documented reciprocal direct projections, and more specifically from the deep layers of the SC the projections terminate in the IC and vise versa that are bilateral [22]. The IC receives strong commissural input from the contralateral IC, via the highly myelinated intercollicular commissure [23]. The SC sends ipsilateral direct efferent projections, known as tectopontine fibers, to the basilar PN and primarily the peduncular, dorsolateral, and ventrolateral pontine regions. These projections originate from the deep layers of the SC and contribute to the visuomotor coordination [2][24][25][26]. The IC additionally projects ipsilaterally to the dorsolateral pontine nuclei as shown in cat studies [27]. The SC also directly projects contralaterally to the IO complex [28]. The SC also sends bilateral efferent projections to the RF, including both mRT and PnO, and these projections play a role in forming the gaze control circuit [2][29], while the IC projects ipsilaterally to the mRT and passes without terminating from regions in the pontine tegmentum that include PnO and they are involved in the auditory startle and orienting reflexes [30]. The SC also sends direct excitatory projections to the subthalamic nucleus (Subthal) of the BG providing a pathway for sensory information for the modulation of movement [31] and to the ipsilateral SNc [32]. The SC sends predominantly ipsilaterally, direct efferent projections to various thalamic nuclei mainly to the pulvinar group, the intralaminar nuclei and to the LGN including in total the Thal_CeM, Thal_CL, Thal_LD, Thal_LP, Thal_LGN, Thal_PF, Thal_PuA, Thal_PuL, Thal_PuI and Thal_PuM [2][33][34]. In contrast, IC projects bilaterally with ipsilateral dominance to the Thal_MGN in the thalamus and this constitutes the major ascending auditory pathway, and to the posterior thalamic group including the Thal_L-Sg and to lesser extend to intralaminar nuclei that include the central lateral (Thal_CL), central medial (Thal_CM), and parafascicular (Thal_Pf) [2][35]. From the deep and intermediate layers of the SC begin direct efferent projections that terminate at the PAG bilaterally, as shown in non-human primate tracer studies [36][29]. Lastly, the SC projects predominantly ipsilaterally

to the VTA [37] and to hypothalamic regions [36][29] while the IC terminates directly to PAG [38][39][40].

Afferent projections to the Tt

Only the SC receives contralateral afferent projections from the medial and inferior subdivisions of the VN, primarily to its intermediate and deep layers [41] as it is demonstrated in non-human primate studies. The SC also receives direct predominantly ipsilateral projections from the RF, including the mRT [42]. The SC receives direct ipsilateral projections from the SNr, that is part of the basal ganglia circuit [29]. The IC receives direct ipsilateral projections and from the Globus Pallidus (GP) [23]. Regarding direct projections from thalamic nuclei, the SC and IC present different patterns. The SC receives direct bilateral projections from the midline and intralaminar thalamic nuclei, including the Thal_CL, Thal_CM, Thal_CeM, Thal_Pf, and Thal_MV(Re) [43][44]. In contrast, IC receives bilateral afferent projections from Thal_CL, Thal_CM, Thal_L-Sg, Thal_MGN and Thal_PF. The Hypo projects directly to the SC as it is demonstrated by cat studies bilaterally with ipsilateral dominance [45]. Additionally, PAG and SC have reciprocal connections, meaning that PAG directly projects contralaterally to the SC [29]. The IC also receives ipsilateral afferent projections from the PAG, the LC and non-dopaminergic projections from the SNr [22][23]. The SC receives direct predominantly ipsilateral projections from the LC as it is a vital pathway for sensory processing modulation [29].

3.2.2.3 Pontine Nuclei: medial, lateral and dorsal pontine nuclei

The Pontine Nuclei (PN) are clusters of gray matter situated in the basilar pons, between the midbrain and the medulla, anterior to the cerebellum. They are distributed across the ventral component of the pons and subdivided into medial, lateral, and dorsal sectors (PNm, PNl, PNd). The PN are the main relay of the cortico-ponto-cerebellar loop, supporting the planning and execution of movement, timing, error correction, and motor control.

Efferent projections from the PN

The PN are pre-cerebellar relay nuclei [46]. Their main efferent projection is the pontocerebellar projection, which decussates and enters the contralateral cerebellum through the middle cerebellar peduncle [2]. There is no evidence supporting direct efferent projections from the PN to any brainstem region of interest.

Afferent projections to the PN

The cerebral cortex provides massive inputs to the pontine nuclei although these cerebral regions were not considered in this matrix and thus the connections were not marked. Besides cortical input, the pontine nuclei receive minor ipsilateral contributions from the SC for coordinating visual and vestibular signals with cerebellar processing, while the IC sends ipsilateral projections to the dorsolateral PN [24][47]. Some deep SC fibers synapse in the pontine nuclei to convey

visual orienting information to the cerebellum. There is evidence that support thalamic projections to the PN that originate from the ipsilateral Thal_LGN nucleus of the thalamus [48][49]. The Hypo also directly projects bilaterally to the PN, all subdivisions included, representing diencephalic modulation of cerebellar processing [48]. Moreover, the PN receive bilateral input with ipsilateral dominance from the LC, which is involved in autonomic functions [48]. Lastly, the PN receive ipsilateral modulatory direct projections from the subthalamic nucleus (Subthal) of the basal ganglia (BG) as part of the bi-synaptic connection between the Subthal and the cerebellum, through the PN [50].

3.2.2.4 Inferior Olivary Complex: principal olive and accessory olives (MAO, DAO)

The Inferior Olivary complex (IO), is located in the rostral medulla and it is subdivided into three parts: 1) Principal Olive (PO) 2) Medial Accessory Olive (MAO) and 3) Dorsal Accessory Olive (DAO). This nuclei complex is important for motor coordination, learning, and timing. Its neurons give rise to climbing fibers that decussate and then enter the contralateral cerebellum, through the inferior cerebellar peduncle, forming a precise olivo-cerebellar map [51].

Efferent projections from the IO

The inferior olivary complex has no significant efferent projections outside the cerebellum. Its exclusive role is to convey error signals and timing information to the cerebellum, enabling motor learning and coordination. Therefore, in the matrix, the inferior olivary complex nodes (PO, MAO, DAO) do not send outputs to other listed brain regions. This strict olivo-cerebellar specialization is supported by anatomical studies [51].

Afferent projections to the IO

The IO complex, although it has a single output target, receives a diverse array of afferent inputs that modulate its activity. The IO receives inputs from the RNp as already mentioned in previous paragraphs. The fibers from the RNp descend through the central tegmental tract to end in the ipsilateral inferior olivary complex, to all its subdivisions [52]. Additionally, it receives ipsilateral input from the PAG [52] and from the VTA [28]. A key input comes from the vestibular nuclei (VN). Recent work demonstrated that the VN provide GABAergic and glycinergic bilateral inputs to the IO [53]. In detail, the VNi projects bilaterally with ipsilateral dominance to the IO complex, while the VNs, VNm and VNl project to the contralateral MAO. The IO complex receives modulatory afferent projections from the BG and more specifically, excitatory inputs from the zona incerta of the subthalamic region as shown by rodent data [54]. Retrograde tracing studies show that neurons in the nucleus reticularis pontis oralis (PnO) provide bilateral projections to the IOC, indicating a widespread reticulo-olivary connectivity [55]. Lastly the mRT sends bilateral projections, with ipsilateral dominance to the ipsilateral medial accessory nucleus of the IO [56].

3.2.2.5 Vestibular Nuclei: superior, medial, lateral and inferior vestibular nuclei

The Vestibular Nuclei (VN) are located beneath the floor of the fourth ventricle in the dorsolateral caudal pons and the rostral medulla. They have four classical subdivisions: 1) superior Vestibular Nuclei (VNs); 2) inferior Vestibular Nuclei (VNi); 3) medial Vestibular Nuclei (VNm); and 4) lateral Vestibular Nuclei (VNl). Their primary role is to contribute to the vestibulo-ocular reflex, which stabilizes the gaze during motion of the head and modulation of the posture.

Efferent projections from the VN

The VN, as it is already mentioned project to the IO complex and VNi send direct efferent projections to the PnO bilaterally with ipsilateral dominance [57]. These connections influence autonomic and respiratory responses to motion and contribute to the integration of vestibular and somatosensory signals for balance reflexes [58][59][60]. Additionally, the VNs and VNm send major efferent projections to various thalamic nuclei. In detail the thalamic nuclei are CL, CM, PF, VA, Vla, VLp and VPL, forming the major vestibulo-thalamocortical pathway that relays vestibular information to cortical areas. These projections are mostly ipsilateral in mammals but contralateral in cat studies[61][62][63]. Direct vestibuloreticular projections from the VN to the mRT have been demonstrated, with contributions from all four VN [57][58]. Finally, the geniculate bodies (Thal_MGN, Thal_LGN, SGN) receive inputs from dorsal, superior and medial VN [64]. These thalamic projections relay vestibular signals to cortical areas for conscious perception of head orientation. Lastly, VN send also direct bilateral projections to LC with contralateral dominance [65].

Afferent projections to the VN

The main direct afferent projections described between VN and brainstem regions are the projections from the RF, both mRT and PnO, to all divisions of the VN, integrating autonomic limbic context with vestibular processing [58][59][60]. It has been observed limited hypothalamic input to the VN, through modern viral tracing studies [17]. The VN also receive direct noradrenergic inputs from the LC, as demonstrated by classical catecholaminergic tracer studies. Evidence for a direct PAG to VN projection is sparse in the classical tracer literature. However, recent mouse cell type specific viral tracing suggests a small direct pathway may exist [17][66][67]. Recent cell-type specific viral tracing studies have highlighted direct ipsilateral projections, with small bilateral components, from the SN and VTA to VN GABAergic neurons, including the VNm, revealing a previously unrecognized dopaminergic influence on vestibular processing [17].

Interconnections of the VN

The VN on the two sides operate as an integrated bilateral network, as the different VN subdivisions are interconnected by extensive intrinsic and commissural connections, including projections to the respective contralateral homologous nucleus. The medial VN receive contralateral projections from the superior and inferior VN. The inferior VN receive fibers from

the superior and medial VN. The superior VN receive contralateral projections from the medial and inferior VN. There are also connections between ipsilateral VN. The superior VN receive projections from the lateral, medial and inferior VN, the lateral VN from the median and inferior VN, the medial VN from the superior VN and the inferior VN from the medial VN [68][69][70]).

3.2.2.6 Reticular Formation: midbrain reticular formation and pontis oralis

The Reticular Formation (RF) is the isodendritic core of the brainstem and serves as a major integration and relay center. In this chapter it was treated as two functional subdivisions: 1) the midbrain reticular formation (mRT) which participates in arousal regulation, orientation, nociceptive regulation and visuomotor integration and 2) the nucleus reticularis Pontis Oralis (PnO) a rostral pontine reticular region strongly implicated in respiratory patterning, locomotor initiation, and autonomic somatic coupling as well as in the sleep-wake cycle, and specifically in the rapid eye movement phase. In the present work, the medial RF referred to in the following paragraphs corresponds anatomically to the mRT described, and the two terms are used for the same anatomical area.

Efferent projections from the RF

As mentioned in previous paragraphs, mRT sends direct efferent projections to the SC to the IO and to the VN. The mRT projects bilaterally with ipsilateral dominance to the PnO [71]. Regarding the BG, specific neuronal subpopulations of the mRT directly project to BG targets including the GP, SN and Subthal bilaterally with ipsilateral dominance [72]. Additionally, mRT projects directly to the thalamic nuclei. In detail, it projects bilaterally to Thal_MV(Re) and Thal_CeM, and ipsilaterally to Thal_PF, Thal_CL and to Thal_LGN mostly for modulatory activity [73] [74]. The mRT projects ipsilaterally to the more caudal levels of the IO complex, where MAO is located, while it also projects bilaterally to the PAG with ipsilateral dominance [56]. Additionally, the mRT projects directly to the ipsilateral Amyg [74]. Both mRT and PnO send direct ipsilateral projections to nuclei of the Hypo [75][76]. PnO sends bilateral projections with ipsilateral dominance to the LC. PnO directly projects to the ipsilateral subthalamus and to ipsilateral thalamic nuclei. In detail, the intralaminar nuclei including parafascicular, paracentral, central lateral, lateral part of the mediodorsal, and the central medial and the midline nuclei rhomboid, reunions, and paraventricular and sparsely the ventromedial nucleus, the posterior nucleus, and the lateral posterior nucleus of the thalamus. PnO projects directly to the ipsilateral VTA and SN. Lastly the PnO projects bilaterally to the mRT, PAG and IO nuclei.

Afferent projections to the RF

As mentioned in previous paragraphs, mRT receives input from the RNm, the VN, and the Tt. The mRT receives direct projections from the ipsilateral amygdala [77]. Regarding the BG nuclei, mRT receives direct projections from the ipsilateral SNr, GPi and Subthal as part of a well-established and documented limbic-diencephalic-brainstem regulatory system [78][79][80]. mRT

receives bilateral projections from the PnO while also receiving contralateral projections from the opposite mRT[71]. PnO receives glutamatergic inputs from the ipsilateral central nucleus of the Amyg [81]. SNr also sends direct bilateral projections with contralateral dominance to the PnO [82]. SNc and LC also project bilaterally to the PnO while the LC projects ipsilaterally to the mRT. There are two well documented pathways that connect directly and bilaterally with ipsilateral dominance the hypothalamic nuclei to both mRT and PnO, the lateral hypothalamic orexin projections to RF hubs and the descending fibers through the dorsal longitudinal fasciculus [75]. Classical anterograde tracer studies in non-human primates demonstrate that the PAG sends dense ipsilateral descending projections to mRT and to PnO [83]. Cell-type specific viral tracing demonstrates that VTA sends direct projections to the pontine reticular formation, including the PnO and to the mRT ipsilaterally [84]. The PnO receives direct ipsilateral inputs from the SC and from the mRT and bilateral with ipsilateral dominance from the VN.

3.2.2.7 Basal Ganglia

Regarding the BG, they include four main components: 1) the striatum (caudate nucleus (Caud), putamen (Puta) and nucleus accumbens (Accu)) 2) the globus pallidus (external and internal) (GPe, GPi) 3) the substantia nigra (SN) which is composed by two subdivisions, Substantia Nigra pars reticullaris (SNr) and Substantia Nigra pars compacta (SNc) and 4) the subthalamic nucleus (Subthal). The role of the BG is to select and shape movements through alternate inhibition and disinhibition through the thalamocortical motor circuits.

Efferent projections from the BG

In review from previous paragraphs, different BG nuclei send direct efferent projections to SC, and to RF predominantly ipsilaterally. Additionally, BG nuclei project to different thalamic nuclei. More specifically, the GPi sends direct ipsilateral efferent projections to the Thal_VA, Thal_VL, Thal_PF and Thal_MD, while the SNr projects directly to the ipsilateral Thal_VA, Thal_VL and Thal_MD) [85][86]. The SNr projects directly and ipsilaterally to the PAG [87] while both SNr and SNc project to the VTA bilaterally [88]. This is a major GABAergic descending output pathway of the basal ganglia that modulates pain and defense behaviors [89]. The ventral striatum, which is the Accu has direct bilateral anatomical connections with the VTA, ipsilateral with the Hypo, and ipsilateral with the PAG [90]. Subthal projects bilaterally with ipsilateral dominance to the PAG [91].

Afferent projections to the BG

In review from previous paragraphs, different BG nuclei receive direct afferent projections from RF and ipsilateral SC. Additionally, AC projects directly to the striatum, which consists of the Put, Accu and Caud [92][90]. The Cl also sends direct ipsilateral projections to the Put and to the Caud as shown by recent non-human primate studies [93]. The Caud and Put also receive bilateral with ipsilateral dominance input from the LC [94][95]. The Accu receives

direct projections from the ipsilateral lateral septal nucleus [96]. The Accu has many anatomical connections with different nuclei. In detail, it receives direct inputs from the VTA neurons bilaterally with ipsilateral dominance, the LC nucleus bilaterally, the PAG bilaterally, and from the Hypo mainly ipsilaterally [90], while also receiving afferents from the Septal [97]. The thalamus sends direct ipsilateral glutamatergic inputs to the Accu. These projections arise from the midline and intralaminar nuclei and more specifically the Thal_MD, Thal_CeM and Thal_PF nuclei[90]. Recent studies in mammals underline that LC sends direct bilateral axonal projections to the dopaminergic neurons of the SN [98]. SNc receives input from the anterior thalamic nuclei and from the AC. Subthal also receives direct input from the PAG [91]. Lastly, the SNc receives ipsilateral projections from the VTA.

Interconnections of the BG nuclei

The BG nuclei have major interconnections, that form the direct (D1) and indirect (D2) pathways. The intrinsic connections of the basal ganglia are predominantly ipsilateral. The SNc projects to the striatum, providing dopaminergic modulation essential for regulating D1 and D2 medium spiny neuron activity. The striatum projects to the GPi and SNr, delivering GABAergic inhibition that shapes the BG output and influences both motor and oculomotor circuits. In the indirect pathway, the striatum projects to the GPe, which in turn modulates downstream nuclei through widespread inhibitory projections, including major outputs to the Subthal, the GPi, and back to the striatum through arkypallidal neurons. The Subthal projects to the GPi and SNr, providing the main excitatory drive that increases inhibitory output toward the thalamus, and also sends reciprocal excitatory projections back to the GPe, forming a key oscillatory loop. Additionally, the GPi and GPe project to the SNc, influencing dopaminergic neuron excitability, while the SNr projects to the Subthal, completing an inhibitory feedback loop within the BG network [99][100][101]. The Accu directly projects to the SNr and SNc and SubTh while receiving direct projections from the SNc [90].

3.2.2.8 Cerebrum Subcortical Nuclei: amygdaloid complex, claustrum, septal nuclei

This section incorporates forebrain subcortical structures that are not included in the brainstem regions but are anatomically and functionally connected with brainstem nuclei, through subcortical and thalamic pathways. These connections have major influence on motor, autonomic and modulatory systems through direct or indirect connections. The three structures are the Amygdaloid Complex (Amyg) the Claustrum (Claus) and the Septal Nuclei (Septal). The Amyg is located in the medial temporal lobe, anterior to the hippocampus. Its main function is the assignment of emotional value to stimuli, and it drives autonomic and defensive responses through the hypothalamus and the brainstem. The CL is a thin sheet of gray matter located between the insula and the putamen and acts as a hub of coordination of cortical networks. The Septal, are located in the basal forebrain, just beneath the corpus callosum near the septum pellucidum. Their main function is the linkage of the hippocampus and the hypothalamus.

Efferent projections from the CSN

The Amyg directly project to the ipsilateral CL [102] and to the ipsilateral Septal [103]. The Amyg also sends direct efferent projections to PAG ipsilaterally based on non-human primate studies [104] and to VTA bilaterally as mentioned in studies [105]. In mammals the GABAergic neurons in the central amygdala project to the LC bilaterally with ipsilateral dominance, modulating its neuronal activities [98]. The Claus projects ipsilaterally to the LC [106] and to the VTA bilaterally [107]. Lastly, the Septal directly project to the VTA and PAG as shown by mice studies [97][96]. These projections are ipsilateral, except with the VTA that are bilateral.

Afferent projections to the CSN

The AC, in addition to the already mentioned connections, also receives direct afferent projections from the VTA and the LC, bilaterally with ipsilateral dominance [108][109][110][111]. Amyg also receives predominantly ipsilateral input from the PAG [87]. It is worth mentioning that the central nucleus of the Amyg and the PAG are extensively and reciprocally interconnected through a network of highly organized rostrocaudal projections [104]. Lastly Septal receives direct efferent projections from the PAG ipsilaterally [112], LC bilaterally with ipsilateral dominance [113], and VTA bilaterally with ipsilateral dominance [114].

3.2.2.9 Thalamus

The thalamus (Th) is a pair of oval-shaped structures in the diencephalon, located above the brainstem on either side of the third ventricle. It is characterized as the brain's main relay hub, directing most of the sensory information to the proper interpretation areas. The main role of the Th is the coordination of motor signals and the support to attention, arousal and the management of the sleep-wake cycles.

Efferent projections from the thalamus

Most efferent projections from the thalamic nuclei have been described in detail in the previous paragraphs. Moreover, in classical anatomy atlases, PAG direct projections are well described, but recent work has shown bidirectional connectivity of these nuclei. Direct thalamic projections to the PAG arise from the Pf and intralaminar nuclei Thal_CM, Thal_CL and Thal_CeM, and to the VTA arise primarily from Pf. These projections are bilateral with a predominance on the ipsilateral side.

Afferent projections to the thalamus

Most of the afferent projections that terminate in different thalamic nuclei have been described in detail in the previous paragraphs. PAG to Th pathways modulate autonomic, nociceptive, and behavior related forebrain circuits associated with defense and emotional responses. Each PAG column sends a distinct but overlapping projection pattern to midline and intralaminar thalamic nuclei, with the ventrolateral and lateral PAG providing the most extensive inputs, especially to

the Thal_MD, Thal_MV(Re), Thal_CL, Thal_CM and Thal_PF, as shown in cat studies [115]. The Thal_LGN receives a dense, bilateral, widespread norepinephrine projection from the LC [116]. The LC also sends bilateral direct projections to the midline and intralaminar thalamic nuclei, and more specifically the Thal_MD, Thal_MV(Re), Thal_CL, Thal_CM and Thal_PF [115]. Finally, the VTA sends direct projections to the Thal_MV(Re), Thal_CeM and Thal_MD [117].

3.2.2.10 Hypothalamus

The hypothalamus (Hypo) is an evolutionarily conserved region of the diencephalon that forms the ventral wall of the third ventricle, extending from the optic chiasm to the mammillary bodies and lying just above the pituitary. Functionally, it integrates neural and blood borne signals to maintain homeostasis by coordinating endocrine autonomic, and behavioral outputs.

Efferent projections from the Hypothalamus

Moreover, the Hypo directly projects to the PAG predominantly ipsilaterally [2][118], to the ipsilateral LC [119] and to the VTA ([120].

Afferent projections to the Hypothalamus

Additionally, the Hypo receives direct projections from the PAG [121], and from the LC predominantly ipsilaterally [122].

3.2.2.11 Periaqueductal Gray

The Periaqueductal Gray (PAG) is also known as central gray and is the gray matter that is located around the cerebral aqueduct within the tegmentum of the midbrain. It is an essential region for pain control, autonomic functions, and defense behaviors.

Efferent projections from the Periaqueductal Gray

Most of the PAG efferent and connections have been described in detail in the previous paragraphs. In summary, PAG sends direct efferent projections to the Tt, RF, BG, Amyg, Septal, IO, Th and Hypo. Moreover, the PAG also projects to LC and VTA bilaterally as it is documented in tract-tracing studies in non-human primates [123][124].

Afferent projections from the Periaqueductal Gray

Most of the PAG afferent and connections have been described in detail in the previous paragraphs. In summary, PAG receives direct afferent projections from the Tt, BG, Th, Amyg and HTh. PAG also receives from the ipsilateral LC and from the VTA bilaterally as it is demonstrated by tract-tracing studies in non-human primates [125][126].

3.2.2.12 Locus Coeruleus

The Locus Coeruleus (LC) is a small and compact noradrenergic nucleus, that is located in the dorsal pontine tegmentum. The LC is a vertebrate specific nucleus and is the brain's main source of norepinephrine, while it modulates arousal, attention, stress response, learning processes, and pain. Regardless its small size, the LC's broad axonal projections enable it to communicate and regulate nearly the entire brain in both non-mammalian and mammalian vertebrates. LC demonstrates evolutionarily conserved features, with both non-mammalian vertebrates and mammalian vertebrates possessing conserved ascending and descending pathways.

Efferent projections from the Locus Coeruleus

LC sends direct projection to various regions mentioned in previous paragraphs. In review, the LC projects directly to VN, BG, RF, PN, Septal, Amyg, Th, Hypo, and Tt. The LC also projects to the contralateral LC. Finally, noradrenergic projections from the LC terminate in the ipsilateral VTA, where they influence dopaminergic neurons and modulate reward-related circuits [111].

Afferent projections to the Locus Coeruleus

In review from previous paragraphs, the LC receives direct input from the RF, VN, Amyg, Claus and Hypo. The LC also receives direct dopaminergic projections from the VTA bilaterally with more prominent the contralateral projections, forming a reciprocal loop that integrates arousal and motivational states [111]. The LC contributes to endogenous descending pain control through its noradrenergic inputs to the SC and in return, it receives afferent inputs from the PAG [98].

3.2.2.13 Ventral Tegmental Area

The Ventral Tegmental Area (VTA) is a brainstem nucleus that is located in the ventromedial mesencephalic tegmentum. It contains dopaminergic, GABAergic, and glutamatergic neurons. It is considered a crucial region in the midbrain, central to the brain's reward system, producing dopamine to influence motivation, pleasure, learning, and addiction.

All the efferent and afferent projections from and to the VTA have been mentioned in detail in the previous paragraphs. In a quick summary, VTA projects to RF, BG, to subcortical regions, to some thalamic nuclei, to PAG and lastly to LC, while it receives direct inputs from the RN, BG, from subcortical regions, from some thalamic nuclei and from the LC, PAG and HTh.

3.2.3 Connectivity matrices

The literature review conducted for this thesis resulted in a connectivity matrix of 104 regions of interest (including left and right divisions), limited to brainstem and subcortical structures (Matrix A), without taking into account intra-subcortical connections, reflecting the anatomical

scope of the present work. As this thesis is part of a larger collaborative project encompassing the whole brain, this brainstem-brainstem and brainstem–subcortical matrix was integrated with two further region sets developed independently within the project: a cerebellum-brainstem matrix, a cerebellar matrix and finally a cortex-brainstem matrix. During this integration, some regions originally kept as separate divisions were collapsed together, for example some of the finer thalamic subdivisions defined in Matrix A were merged, reducing the 21 thalamic nuclei per hemisphere to 16. All regions that were merged are shown in Table 3.2.

Region in Matrix A	Region in Matrices B and C
RNp	RN
RNm	
PNm	Pons
PNl	
PNd	
PO	ION
MAO	
DAO	
VNs	Ve
VNm	
VNl	
VNi	
Gpi	Pall
Gpe	
Thal_LD	Thal_LDP
Thal_LP	
Thal_VPl	Thal_VPL
Thal_Vla	
Thal_VLp	
Thal_CeM	Thal_IntR
Thal_CL	
Thal_CM	Thal_IntC
Thal_PF	
Thal_MGN	Thal_MSGN
Thal_L-Sg	

Table 3.2: Correspondence between Matrix A regions and their single representation in Matrices B and C.

The brainstem connectivity defined in Matrix A was combined with the independently developed cerebellar and cortical connections, so that the resulting whole-brain matrix retains the complete brainstem connectivity of Matrix A together with the added cerebellar and cortical connections. This integrated parcellation was used in two versions with the only difference being the representation and segmentation of the pons. In Matrix B which consists of 112 regions, the pons is instead represented as a single region, because it was not individually segmented in the brain atlas used. This matrix was used to perform the analysis between different tractography configurations. In Matrix C which consists of 139 regions, the pons is subdivided into 14 distinct

sub-regions per hemisphere. This fully segmented, binary matrix was used to compute the graph-theory metrics, so that pontine connections could be resolved in full depth.

Matrix A (104)		Matrix B (112)		Matrix C (139)	
RNp_L	RNp_R	PFC_L	PFC_R	PFC_L	PFC_R
RNm_L	RNm_R	M1_L	M1_R	M1_L	M1_R
SC_L	SC_R	PMSMA_L	PMSMA_R	PMSMA_L	PMSMA_R
IC_L	IC_R	Hypo_L	Hypo_R	Hypo_L	Hypo_R
PNm_L	PNm_R	Thal_AV_L	Thal_AV_R	Thal_AV_L	Thal_AV_R
PNl_L	PNl_R	Thal_LDP_L	Thal_LDP_R	Thal_LDP_L	Thal_LDP_R
PNd_L	PNd_R	Thal_VA_L	Thal_VA_R	Thal_VA_L	Thal_VA_R
PO_L	PO_R	Thal_VLA_L	Thal_VLA_R	Thal_VLA_L	Thal_VLA_R
MAO_L	MAO_R	Thal_VLP_L	Thal_VLP_R	Thal_VLP_L	Thal_VLP_R
DAO_L	DAO_R	Thal_VPL_L	Thal_VPL_R	Thal_VPL_L	Thal_VPL_R
VNs_L	VNs_R	Thal_IntR_L	Thal_IntR_R	Thal_IntR_L	Thal_IntR_R
VNm_L	VNm_R	Thal_IntC_L	Thal_IntC_R	Thal_IntC_L	Thal_IntC_R
VNl_L	VNl_R	Thal_MDm_L	Thal_MDm_R	Thal_MDm_L	Thal_MDm_R
VNi_L	VNi_R	Thal_MDl_L	Thal_MDl_R	Thal_MDl_L	Thal_MDl_R
mRT_L	mRT_R	Thal_LGn_L	Thal_LGn_R	Thal_LGn_L	Thal_LGn_R
PnO_L	PnO_R	Thal_MSGn_L	Thal_MSGn_R	Thal_MSGn_L	Thal_MSGn_R
SNc_L	SNc_R	Thal_PulA_L	Thal_PulA_R	Thal_PulA_L	Thal_PulA_R
SNr_L	SNr_R	Thal_PulI_L	Thal_PulI_R	Thal_PulI_L	Thal_PulI_R
Caud_L	Caud_R	Thal_PulL_L	Thal_PulL_R	Thal_PulL_L	Thal_PulL_R
Puta_L	Puta_R	Thal_PulM_L	Thal_PulM_R	Thal_PulM_L	Thal_PulM_R
Accu_L	Accu_R	Caud_L	Caud_R	Caud_L	Caud_R
Subthal_L	Subthal_R	Puta_L	Puta_R	Puta_L	Puta_R
Gpi_L	Gpi_R	Pall_L	Pall_R	Pall_L	Pall_R
Gpe_L	Gpe_R	Accu_L	Accu_R	Accu_L	Accu_R
Amyg_L	Amyg_R	Hippo_L	Hippo_R	Hippo_L	Hippo_R
Cla_L	Cla_R	Amyg_L	Amyg_R	Amyg_L	Amyg_R
Septal_L	Septal_R	Septal_L	Septal_R	Septal_L	Septal_R
Thal_AvN_L	Thal_AvN_R	Subthal_L	Subthal_R	Subthal_L	Subthal_R
Thal_CeM_L	Thal_CeM_R	Cla_L	Cla_R	Cla_L	Cla_R
Thal_CL_L	Thal_CL_R	RN_L	RN_R	RN_L	RN_R
Thal_CM_L	Thal_CM_R	SNc_L	SNc_R	SNc_L	SNc_R
Thal_LD_L	Thal_LD_R	SNr_L	SNr_R	SNr_L	SNr_R
Thal_LGN_L	Thal_LGN_R	SC_L	SC_R	SC_L	SC_R
Thal_LP_L	Thal_LP_R	IC_L	IC_R	IC_L	IC_R
Thal_L-Sg_L	Thal_L-Sg_R	mRT_L	mRT_R	mRT_L	mRT_R
Thal_MDl_L	Thal_MDl_R	LC_L	LC_R	LC_L	LC_R
Thal_MDm_L	Thal_MDm_R	ION_L	ION_R	ION_L	ION_R
Thal_MGN_L	Thal_MGN_R	Ve_L	Ve_R	Ve_L	Ve_R
Thal_MV(Re)	Thal_MV(Re)	PnO_L	PnO_R	PnO_L	PnO_R
PF_L	PF_R	VTA		VTA	

continued on next page

Matrix A (104)		Matrix B (112)		Matrix C (139)	
Thal_PuA_L	Thal_PuA_R	PAG		PAG	
Thal_PuL_L	Thal_PuL_R	Pons		PN_L	PN_R
Thal_PuI_L	Thal_PuI_R	Cbm_Left_I_IV	Cbm_Right_I_IV	NRTP_L	NRTP_R
Thal_PuM_L	Thal_PuM_R	Cbm_Left_V	Cbm_Right_V	PPN_L	PPN_R
Thal_VA_L	Thal_VA_R	Cbm_Left_VI	Cbm_Right_VI	PB_L	PB_R
Thal_VLa_L	Thal_VLa_R	Cbm_Left_CrusI	Cbm_Right_CrusI	LDT_L	LDT_R
Thal_VLp_L	Thal_VLp_R	Cbm_Left_CrusII	Cbm_Right_CrusII	TPS_L	TPS_R
Thal_VPl_L	Thal_VPl_R	Cbm_Left_VIIb	Cbm_Right_VIIb	TM_L	TM_R
Hypo_L	Hypo_R	Cbm_Left_VIIIa	Cbm_Right_VIIIa	ABD_L	ABD_R
PAG_L	PAG_R	Cbm_Left_VIIIb	Cbm_Right_VIIIb	FM_L	FM_R
LC_L	LC_R	Cbm_Left_IX	Cbm_Right_IX	Ssal_L	Ssal_R
VTA_L	VTA_R	Cbm_Left_X	Cbm_Right_X	CN_L	CN_R
		Left_Dentate	Right_Dentate	RNPON_L	RNPON_R
		Left_Interposed	Right_Interposed	CSR_L	CSR_R
		Left_Fastigial	Right_Fastigial	SOC_L	SOC_R
		Cbm_Vermis_VI		Cbm_Left_I_IV	Cbm_Right_I_IV
		Cbm_Vermis_VII		Cbm_Left_V	Cbm_Right_V
		Cbm_Vermis_VIII		Cbm_Left_VI	Cbm_Right_VI
		Cbm_Vermis_IX		Cbm_Left_CrusI	Cbm_Right_CrusI
		Cbm_Vermis_X		Cbm_Left_CrusII	Cbm_Right_CrusII
				Cbm_Left_VIIb	Cbm_Right_VIIb
				Cbm_Left_VIIIa	Cbm_Right_VIIIa
				Cbm_Left_VIIIb	Cbm_Right_VIIIb
				Cbm_Left_IX	Cbm_Right_IX
				Cbm_Left_X	Cbm_Right_X
				Left_Dentate	Right_Dentate
				Left_Interposed	Right_Interposed
				Left_Fastigial	Right_Fastigial
				Cbm_Vermis_VI	
				Cbm_Vermis_VII	
				Cbm_Vermis_VIII	
				Cbm_Vermis_IX	
				Cbm_Vermis_X	

Table 3.3: Regions included in the three connectivity matrices (left/right divisions). Matrix A: literature-based brainstem–subcortical matrix (104 regions); Matrix B: integrated whole-brain matrix with the pons as a single region (112 regions); Matrix C: as Matrix B but with the pons subdivided into 14 subnuclei per hemisphere (139 regions).

3.3 Graph theory metrics

To characterize the organization of the connectivity Matrix C, a set of graph theory metrics was computed. The matrix was treated as a directed graph, in which the nodes correspond to the regions of interest, and the edges represent the connections between them along with their direction. Because the reference matrix is binary, encoding only the presence or absence of a connection, only metrics defined for binary and directed graphs were used, and weighted measures were excluded.

If A is defined as the connectivity matrix used (Matrix C) of size $N \times N$, where N is the number of regions, then $A_{ji} = 1$ is the presence of a connection from region j to i, and consequently $A_{ji} = 0$ is the absence of such connection. Self-connections were also excluded. The metrics computed were the following.

The *in-degree,* referring to the number of connections a region receives, calculated by the formula:

$$k_i^{\text{in}} = \sum_j A_{ji} \tag{3.1}$$

where $A_{ji} = 1$ marks a connection directed from region j to region i, so the sum counts the inputs arriving at region i.

The *out-degree,* referring to the number of projections it sends, calculated by the formula:

$$k_i^{\text{out}} = \sum_j A_{ij} \tag{3.2}$$

where $A_{ij} = 1$ marks a connection directed from region i to region j, so the sum counts the outputs leaving region i.

The *total degree*, corresponds to the sum of the previous two metrics.

$$k_i = k_i^{\text{in}} + k_i^{\text{out}} \tag{3.3}$$

Local reciprocity was also computed to quantify the proportion of a regions' connections that are bidirectional. It is calculated as:

$$r_i = \frac{\sum_j A_{ij} A_{ji}}{\sum_j max(A_{ij}, A_{ji})}, \tag{3.4}$$

where the numerator $A_{ij}A_{ji} = 1$ only when a connection exists in *both* directions between regions i and j, while the denominator $max(A_{ij}, A_{ji}) = 1$ whenever a connection exists in *at least one* direction. Thus r_i is the fraction of region i's connections that are bidirectional.

In addition, a set of complementary metrics were computed to describe the role of each region within the network for example how central a region is to the network communication, how strongly it is embedded in interconnected clusters and where it lies along the network's source-sink hierarchy.

In detail, the metrics include the *betweenness centrality*, expressing how often a region lies on the shortest paths between other regions. In a binary and directed network, betweenness centrality uses the term shortest path to describe the route using the least connections. High values mark regions as bridge or relay nodes whose removal would most disrupt communication. It is calculated by the formula:

$$b_i = \sum_{s \neq i \neq t} \frac{\sigma_{st}(i)}{\sigma_{st}} \tag{3.5}$$

where σ_{st} is the total number of shortest paths from region s to region t, and $\sigma_{st}(i)$ is the number of those paths that pass through region i. The values were normalized to the range $[0, 1]$ by dividing by $(N-1)(N-2)$, where N is the number of regions.

The directed *clustering coefficient* quantifies the tendency of a region's neighbors to also be interconnected. For a binary matrix is calculated by the formula:

$$C_i = \frac{\frac{1}{2}\left[(A + A^{\mathsf{T}})^3\right]_{ii}}{k_i^{\text{tot}}\left(k_i^{\text{tot}} - 1\right) - 2k_i^{\leftrightarrow}} \tag{3.6}$$

where k^{tot} is the total degree of node i and k is the number of bidirectional edges involving the node i.

The *trophic level* describes the geometrical positions of each region in the directed network. The trophic level thus orders the regions from sources to sinks. Lower values correspond to nodes that are drivers/sources, high values correspond to nodes that receivers/sinks, mostly incoming projections. It is obtained by solving a linear system:

$$\Lambda\, h = v \tag{3.7}$$

with

$$\Lambda = diag(u) - (A + A^{\mathsf{T}}), \qquad u_i = k_i^{\text{in}} + k_i^{\text{out}}, \qquad v_i = k_i^{\text{in}} - k_i^{\text{out}} \tag{3.8}$$

Lastly, the *coreness* quantifies how deeply a region is embedded within the densely interconnected cores of the network. It is based on the k-core decomposition.

A k-core is the largest group of regions in which each region is connected to at least k others within that same group. It is obtained by repeatedly removing all regions whose total degree is below k, until only regions with degree $\geq k$ remain. It is represented by the formula:

$$k\text{-core} = \text{largest subnetwork with } k_i^{\text{in}} + k_i^{\text{out}} \geq k \text{ for every region } i. \tag{3.9}$$

The coreness of a region is then the largest value of k for which that region still belongs to the k-core:

$$coreness(i) = max\{\, k : i \in k\text{-core} \,\}. \tag{3.10}$$

Increasing the k isolates progressively denser cores. A region that remains in the network at high values of k has high coreness and lies in the most tightly interconnected structural core. Because the total degree combines incoming and outgoing connections, coreness reflects both together, rather than the two separately.

All metrics were computed using the Brain Connectivity Toolbox (http://www.brain-connectivity-toolbox.net, [12]) in MATLAB R2025b (MATLAB - MathWorks Inc., Natick, Massachusetts, USA), using the binary directed implementation of each measure. In detail the previous mathematical formulas were implemented as follows in Listing 3.1:

```
% -- in-degree, out-degree, reciprocity -- %
[id, od, deg] = degrees_dir(A);
recip = zeros(n,1);
for i = 1:n
    out_i = A(i,:) > 0; in_i = A(:,i)' > 0; either = sum(out_i | in_i);
    if either > 0, recip(i) = sum(out_i & in_i)/either; end
end

% -- betweenness (raw + normalized), clustering, coreness -- %
BC = betweenness_bin(A);
BCnorm = BC(:) / ((n-1)*(n-2));
C = clustering_coef_bd(A);
coreness = kcoreness_centrality_bd(A);

% -- trophic level (custom, needs to be validated on example graphs) -- %
u = id(:) + od(:); v = id(:) - od(:);
L = diag(u) - (A + A');
L(1,:) = 0; L(1,1) = 1; v(1) = 0;
h = L \ v; h = h - min(h);
```

Listing 3.1: MATLAB code used to compute the graph-theory metrics (Brain Connectivity Toolbox).

3.4 Subjects and data

The work of this thesis is based on data that were obtained from the Lifespan Human Connectome Project-Aging (HCP-A) dataset [127][128]. All data are publicly available and de-identified, and no new acquisition is required. The data set provides information about two different modalities. More specifically, the structural T1, used for anatomical segmentation and as the reference space for the analysis, and the diffusion-MRI that was used for fiber orientation estimation and tractography. The HCP-A diffusion data were acquired on a 3T Siemens Prisma scanner equipped with high-performance magnetic field gradients (80 mT/m), allowing a 1.5 mm isotropic spatial resolution in human dMRI which is higher than the 2 mm typically used for conventional diffusion MRI. This provides an advantage for resolving the reconstruction of the small nuclei of the brainstem. The acquisition parameters are summarized in the Table 3.5.

Parameter	Value
Acquisition	
Diffusion scheme	Multishell
b-values	1500 and 3000 s/mm^2
Diffusion sampling directions	93 and 92 (respectively)
In-plane resolution	1.5 mm
Slice thickness	1.5 mm

Table 3.5: Diffusion MRI acquisition parameters.

The analysis that was conducted in this thesis was carried out on the data of a single representative healthy subject HCA6053758 (female, age in months: 437), with the aim of identifying the best-performing tractography extraction method before applying it to the full cohort.

3.5 Atlas definition and region segmentation

The regions used for analysis in this work were defined by a dedicated anatomical atlas, developed to include all the brainstem regions of interest together with additional structures connected to them. Since no single tool could segment all of these regions, the atlas was constructed by combining subject-specific segmentations with labels derived from existing anatomical atlases. Where suitable subject-specific segmentation tools were available, the segmentations were performed on each subject's T1 weighted image. Whenever a method relied on an external atlas, its labels were registered to the same T1-weighted image using ANTs registration [129]. The only exception was the dentate nucleus, which was segmented in the diffusion space (DWI). The individual segmentations were eventually merged and formed the single subject-specific labeled atlas. The complete atlas consisted of 112 regions, including lateralized regions in both

hemispheres and two midline structures: the ventral tegmental area and the periaqueductal gray. Each region was assigned a unique integer label, from 1 to 112. The labeled atlas was generated at two isotropic resolutions: 0.8 mm, and 1.5 mm.

The following Table 3.7 summarizes the segmentation approach used for each region.

Anatomical structure	Tool / Atlas
Cortex (PFC, M1, PMSMA)	Brodmann-based atlas (MNI space)
Cerebellar cortex	FastSurfer, CerebNet
Thalamic nuclei (AV, LDP, VA, VLA, VLP, VPL, IntR, IntC, MDm, MDl, LGn, MSGn, PulA, PulI, PulL, PulM)	FreeSurfer, recon-all and segmentThalamicNuclei.sh
Basal Ganglia (Caud, Put, Pall, Accu), Hippocampus (Hippo), Amygdala (Amyg)	FSL FIRST, run_first_all
Hypothalamus (Hypo)	FreeSurfer, mri_segment_hypothalamic_subunits
Septal nuclei (Septal)	FreeSurfer, mri_sclimbic_seg
Subthalamic nucleus (Subthal)	https://www.nature.com/articles/s41597-020-00644-6
Claustrum (Cla)	https://github.com/MezerLab/ClaustrumSegmentation
Brainstem (pons)	FreeSurfer, segmentBS.sh
Arousal structures (mRT, PnO, LC, VTA, PAG)	FreeSurfer, SegmentAAN.sh
Brainstem (RN, SNc, SNr)	https://www.nature.com/articles/sdata201863
Superior colliculus (SC), inferior colliculus (IC), inferior olivary nucleus (ION), vestibular nuclei (Ve)	Navigator_152
Interposed nucleus (IN), fastigial nucleus (FN)	Atlante cerebellare SUIT
Dentate nucleus (DN)	https://github.com/marta-gaviraghi/segmentDN

Table 3.7: Segmentation tool or atlas used for each anatomical structure.

From each resolution, the volumes of each region were collected using the command "$fslstats -V$ ", which returns the volume in mm^3 of each labeled region, computed as the number of voxels assigned to it multiplied by the voxel volume. For each region of the atlases, the percentage volume difference between the two resolutions was computed relative to the mean of the two measurements:

$$\%\Delta V = \frac{V_{1.5} - V_{0.8}}{(V_{1.5} + V_{0.8})/2} \times 100 \tag{3.11}$$

where $V_{1.5}$ and $V_{0.8}$ are the regional volumes at 1.5 mm and 0.8 mm isotropic resolution,

respectively. A positive value indicates a larger volume at 1.5 mm.

The agreement between the two resolutions was assessed with a Bland–Altman plot, reporting the mean percentage difference (bias) and its 95% limits of agreement (bias ± 1.96 SD). The assessment of the relationship between volume differences and region size was quantified using Spearman's rank correlation coefficient (ρ) using the "corr" function in MATLAB, that is based on the formula:

$$\rho = 1 - \frac{6 \sum_{i=1}^{n} d_i^2}{n\left(n^2 - 1\right)}, \tag{3.12}$$

where d_i is the difference between the ranks of the two variables for region i and n is the number of regions. Region size was defined as the mean of the two volume measurements (1.5 mm and 0.8 mm), $\bar{V} = (V_{1.5} + V_{0.8})/2$. Both the absolute ($mm^3$) and the relative (%) differences were examined.

3.6 Tractography extraction methods

Fiber orientation distributions were estimated from the preprocessed diffusion data with 1.5mm isotropic resolution and then were used to perform whole-brain probabilistic and deterministic tractography. To evaluate how the reconstruction strategy affects the resulting connectivity, and particularly its anatomical accuracy, several tractography configurations were used and then compared. These configurations differed in many respects, whether anatomical constraints were applied, the seeding strategy, and different FOD amplitude cutoff value as the stopping criteria.

Because standard 5TT segmentation does not reliably classify the brainstem and deep cerebellar nuclei as deep gray matter (GM), streamlines that terminate in these structures are at risk of being incorrectly deleted under a standard ACT framework. To address this, the 5TT image was modified by adding a mask that consists of all the brainstem regions and deep cerebellar nuclei, derived from the atlas segmentation described in the previous paragraph, to the subcortical gray matter tissue volume. This modified 5TT image was used to compute the gray matter-white matter interface, that is the boundary surface between gray and white matter, which served as the seeding mask for the tractography configurations described below. In detail, the streamlines were seeded at the interface rather than at random points, since this reflects more accurately the biological origin of white matter fibers. Streamline propagation was constrained by ACT meaning that the tracts were constrained to follow anatomically plausible trajectories, with streamlines terminated precisely at the interface. Where a streamline's proposed termination failed ACT's criteria, the algorithm was permitted to backtrack and resume tracking from an earlier point rather than terminating the streamline earlier than needed.

Streamline propagation was also constrained by a fiber orientation distribution (FOD) amplitude cutoff, below which the tracking was terminated. The amplitude cutoff, essentially sets the minimum FOD value that must be present for the tracking to continue. When a streamline

reaches a point at which the FOD amplitude falls below this threshold, the orientation is then considered too weak to be trusted and the streamline is terminated. The threshold therefore controls how far the reconstruction of the tract is allowed to proceed into regions of low of fiber orientation. To conclude lower cutoff values allow the formation of tracts to continue into regions of lower anisotropy while higher values enforce stricter, more conservative termination.

The following configurations were produced to examine which extraction configuration showed more accurate results:

1. **Deterministic tractography:** The simplest tractography algorithm, in which the single most likely fiber orientation is followed at each step, rather than sampling probabilistically from the orientation distribution or any anatomical constrains.
2. **No-ACT**: Probabilistic whole-brain tractography performed without anatomically constrained tractography, used as a baseline in which no tissue-based anatomical priors restrict the streamlines.
3. **ACT traditional:** A standard anatomically constrained tractography configuration, without 5TT modified.
4. **ACT + seed at the gray-white matter interface + default cutoff:** Anatomically constrained tractography, with streamlines seeded from the gray-white matter interface and the default FOD amplitude cutoff of 0.05.
5. **ACT + seed at the gray-white matter interface + 0.06 cutoff:** The same configuration as above, but with a modified FOD amplitude cutoff of 0.06, to assess the effect of the stopping threshold on the reconstructed connections.
6. **ACT + dynamic seeding + default cutoff:** Anatomically constrained tractography with dynamic seeding, in which seed points are distributed according to the fiber density [], combined with the default cutoff.
7. **ACT + seed at the gray-white matter interface + default cutoff + 0.8 resolution:** The same default configuration but it was performed on diffusion data resampled to a 0.8 mm voxel resolution, with the aim to assess the effect of spatial resolution on the reconstructed connections.

3.7 Tractography extraction methods comparison

In order to evaluate how accurately each tractography extraction method reconstructed the expected anatomical connectivity, a validation framework was needed. More specifically, the literature derived connectivity matrix (Matrix B) was used as the ground truth, in two different sets of regions. The reason behind this choice, was because the parcellation of the matrix B

regions, matches the atlas in which the tractography was performed. Matrix C was therefore unsuitable, as pons is subdivided into 14 regions per hemisphere, while the atlas takes pons as one region. Matrix A covers only brainstem-brainstem and brainstem-subcortical connections. The first set comprised of the whole 112 region connectome, while the second set comprised of 75 regions, with brainstem, thalamic and subcortical regions. For the second set, a connection was taken into account when at least one of its endpoints was a brainstem region, with both endpoints belonging to the 75-region set, so that only brainstem–brainstem and brainstem–subcortical connections were considered. The 75 regions were: Hypo, Thal_AV, Thal_LDP, Thal_VA, Thal_VLA, Thal_VLP, Thal_VPL, Thal_IntR, Thal_IntC, Thal_MDm, Thal_MDl, Thal_LGn, Thal_MSGn, Thal_PulA, Thal_PulI, Thal_PulL, Thal_PulM, Caud, Puta, Pall, Accu, Hippo, Amyg, Septal, Subthal, Cla, RN, SNc, SNr, SC, IC, mRT, LC, ION, Ve, PnO, both left and right, together with three midline structures VTA, PAG and the Pons.

The possible number of total connections comes from the number of regions in Matrix B. For a matrix that consists of 112 regions, so $R = 112$, there are R^2 connections. Removing the self-connections of the regions, the possible connections are $R(R-1)$. From this total, intra-cortical and intra-subcortical connections were excluded, as they were not the main scope of this work.

$$N = (R^2 - R) - N_{\text{intra-cortical}} - N_{\text{intra-subcortical}} = 9750 \tag{3.13}$$

where N, is the total number of possible directed connections. Matrix B contained $P = 1119$ existing connections, and $N - P = 8631$ absent connections. For the second set, the number of possible connections was $N_{\text{Brainstem}} = 2898$. In this set the existing connections were $P_{\text{Brainstem}} = 608$, thus giving $N_{\text{Brainstem}} - P_{\text{Brainstem}} = 2290$ absent connections.

For each configuration a confusion matrix was created with four values:

- **True positives (TP)**: connections present in both the Matrix B and the tractography.
- **False positives (FP)**: connections reconstructed by the tractography but that are absent from the Matrix B.
- **False negatives (FN)**: connections present in the Matrix B but not reconstructed by the tractography.
- **True negatives (TN)**: connections that are absent from the Matrix B and did not get reconstructed either.

Consequently, the reference connections can be expressed as TP+FN $= P$ and TP+FP equals the total number of connections reconstructed by the configuration, while TN $= N -$ TP $-$ FP $-$ FN.

To impose an anatomical order on the whole connectome, the 112 regions were grouped into five systems (cortex, thalamus, subcortical, brainstem and cerebellum), as detailed in Table 3.9.

System	N	Regions
Cortex	6	PFC, M1, PMSMA
Thalamus	32	Thal_AV, Thal_LDP, Thal_VA, Thal_VLA, Thal_VLP, Thal_VPL, Thal_IntR, Thal_IntC, Thal_MDm, Thal_MDl, Thal_LGn, Thal_MSGn, Thal_PulA, Thal_PulI, Thal_PulL, Thal_PulM
Subcortical	20	Hypo, Caud, Puta, Pall, Accu, Hippo, Amyg, Septal, Subthal, Cla
Brainstem	23	RN, SNc, SNr, SC, IC, mRT, LC, ION, Ve, PnO plus the midline VTA, PAG and Pons
Cerebellum	31	Cortical lobules I–X and vermis VI–X; deep nuclei dentate, interposed, fastigial

Table 3.9: Grouping of the 112 Matrix B regions into five anatomical systems.

3.7.1 Evaluation metrics: Sensitivity, Precision, Specificity

The *sensitivity*, also called recall, quantifies the proportion of the ground truth connections that a configuration successfully reconstructed, using the formula:

$$\text{Sensitivity} = \frac{\text{TP}}{\text{TP} + \text{FN}}. \tag{3.14}$$

A high sensitivity indicates that few anatomically expected connections were missed. The complementary metric *false-negative rate* is $\text{FNR} = \text{FN}/(\text{TP} + \text{FN}) = 1 - \text{Sensitivity}$.

The *precision*, quantifies the proportion of the connections reconstructed by a configuration that are genuinely present in the Matrix B:

$$\text{Precision} = \frac{\text{TP}}{\text{TP} + \text{FP}}. \tag{3.15}$$

A high precision indicates few false connections.

Sensitivity and precision are reported together because they are able to capture opposite kinds of failure. For example a configuration may recover many true connections at the cost of many false ones, or vice versa.

The *specificity*, quantifies the proportion of absent connections that are correctly identified as absent, using the formula:

$$\text{Specificity} = \frac{\text{TN}}{\text{TN} + \text{FP}}, \tag{3.16}$$

3.7.2 Overall performance measures

Two single-value measures were used to rank the tractography configurations. The *F1 score*, which is is the harmonic mean of precision and sensitivity and therefore summarizes how well a configuration balances recovering true connections and avoiding false ones. It is calculated by the formula:

$$\mathrm{F1} = 2 \cdot \frac{\mathrm{Precision} \cdot \mathrm{Sensitivity}}{\mathrm{Precision} + \mathrm{Sensitivity}} = \frac{2\,\mathrm{TP}}{2\,\mathrm{TP} + \mathrm{FP} + \mathrm{FN}}. \tag{3.17}$$

The F1 score does not take true negatives into account, which is appropriate when the interest lies in the correctly and incorrectly reconstructed connections rather than in the correctly rejected ones.

The *Matthews correlation coefficient* (MCC) was additionally used as an overall measure, because it is regarded as the most informative single score for imbalanced binary classification. It incorporates all four values of the confusion matrix for each configuration and reaches a high value only when the classifier performs well on both classes simultaneously. The formula used is:

$$\mathrm{MCC} = \frac{\mathrm{TP} \cdot \mathrm{TN} - \mathrm{FP} \cdot \mathrm{FN}}{\sqrt{(\mathrm{TP} + \mathrm{FP})(\mathrm{TP} + \mathrm{FN})(\mathrm{TN} + \mathrm{FP})(\mathrm{TN} + \mathrm{FN})}}. \tag{3.18}$$

The MCC ranges from -1 to $+1$ indicating perfect disagreement, chance-level agreement, and perfect agreement between the reconstructed and the ground truth connectome at at A value of +1 means every connection was classified correctly, 0 corresponds to a performance no better than random guessing, and −1 indicates complete disagreement.

To identify which parts of the network were most affected by incomplete reconstruction of the tracts, the missing connections were broken down by anatomical system. Each missing connection was attributed to a single anatomical system according to its source region. For each system, a pie chart was created, that reports the number of missing connections originating from that system and the corresponding percentage of all missing connections based on the formula:

$$\mathrm{percentage}_{\mathrm{system}} = \frac{\text{missing connections from system}}{\text{total missing connections (FN)}} \times 100 \tag{3.19}$$

3.7.3 Region volume as reconstruction failure predictor

In order to test whether false negative tracts are associated with region's volume, a linear regression was used to model the proportion of each region's literature connections that tractography failed to reconstruct as a function of the region's volume. The regression model was performed using the best performing tractography configuration.

For each of the 112 regions, the miss proportion was computed as the number of missed connections (i.e., literature connections that tractography failed to reconstruct) divided by the total number of literature connections (counted either as targets or sources of a connection in Matrix B), giving a value between 0 and 1. Region volume was taken from the atlas segmentation at 1.5 mm isotropic resolution and $\log_{10}$-transformed, because volumes spanned more than three orders of magnitude. The relationship was estimated using ordinary least-squares linear regression model:

$$p_{\text{miss}} = \beta_0 + \beta_1 \, log_{10}(V) + \varepsilon,$$

Where p_{miss}, the proportion of a region's literature connections that were not reconstructed using tractography, is the dependent variable, and $log_{10}(V)$, the log-transformed region's volume, is the only independent variable. The intercept β_0 represents the predicted miss proportion when $log_{10}(V) = 0$, setting the baseline height of the regression line. The slope β_1 describes how the miss proportion changes as volume increases and ε is the error (residual) term, which captures the deviation of each region's observed miss proportion from the value predicted by its volume. A negative value indicates that larger regions have lower predicted miss proportions. The slope and its p-value were also calculated together with the coefficient of determination R^2, which represents the fraction of variation in miss proportion explained by volume. The regression was performed in MATLAB R2025b using the "fitlm" function.

Chapter 4

Results

4.1 Structural connectivity matrices

The brainstem matrix, Figure 4.1, Matrix A comprised 104 regions and included 796 connections, excluding projections between subcortical regions.

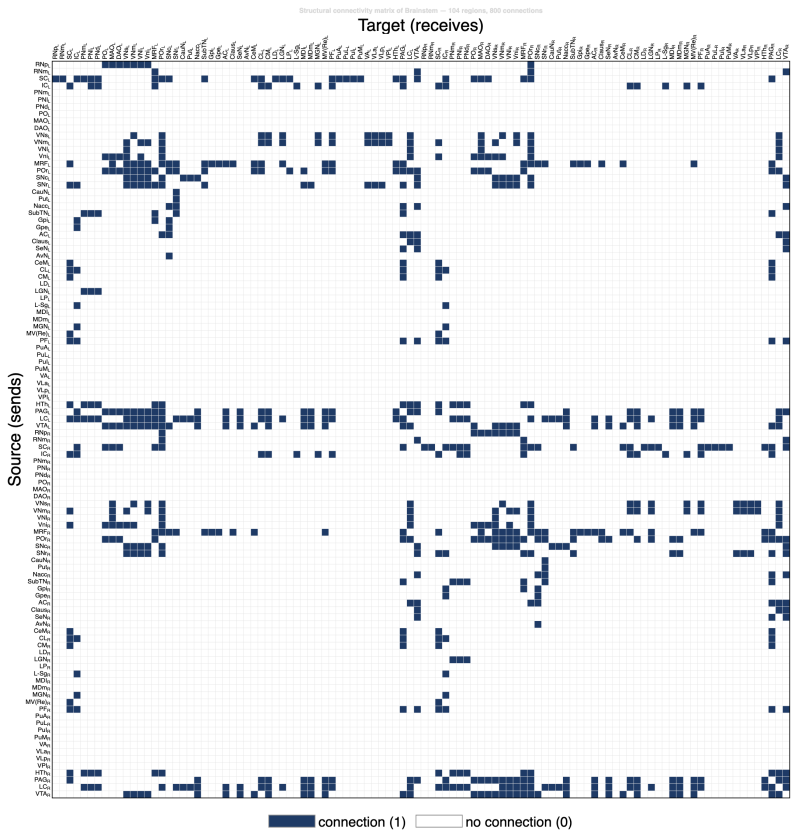


Figure 4.1: Matrix A: Brainstem and subcortical directed structural connectivity based on literature. Out of the 796 connections, 306 were ipsilateral, reaching only same-side target regions, 50 were contralateral projection, reaching only opposite-side target regions and 220 were bilateral, reaching both ipsilateral and contralateral target regions.

Following the integration of connections involving cerebellar and cortical regions, the combined matrix, Figure 4.2, Matrix B contained 112 regions and 1119 directed connections.

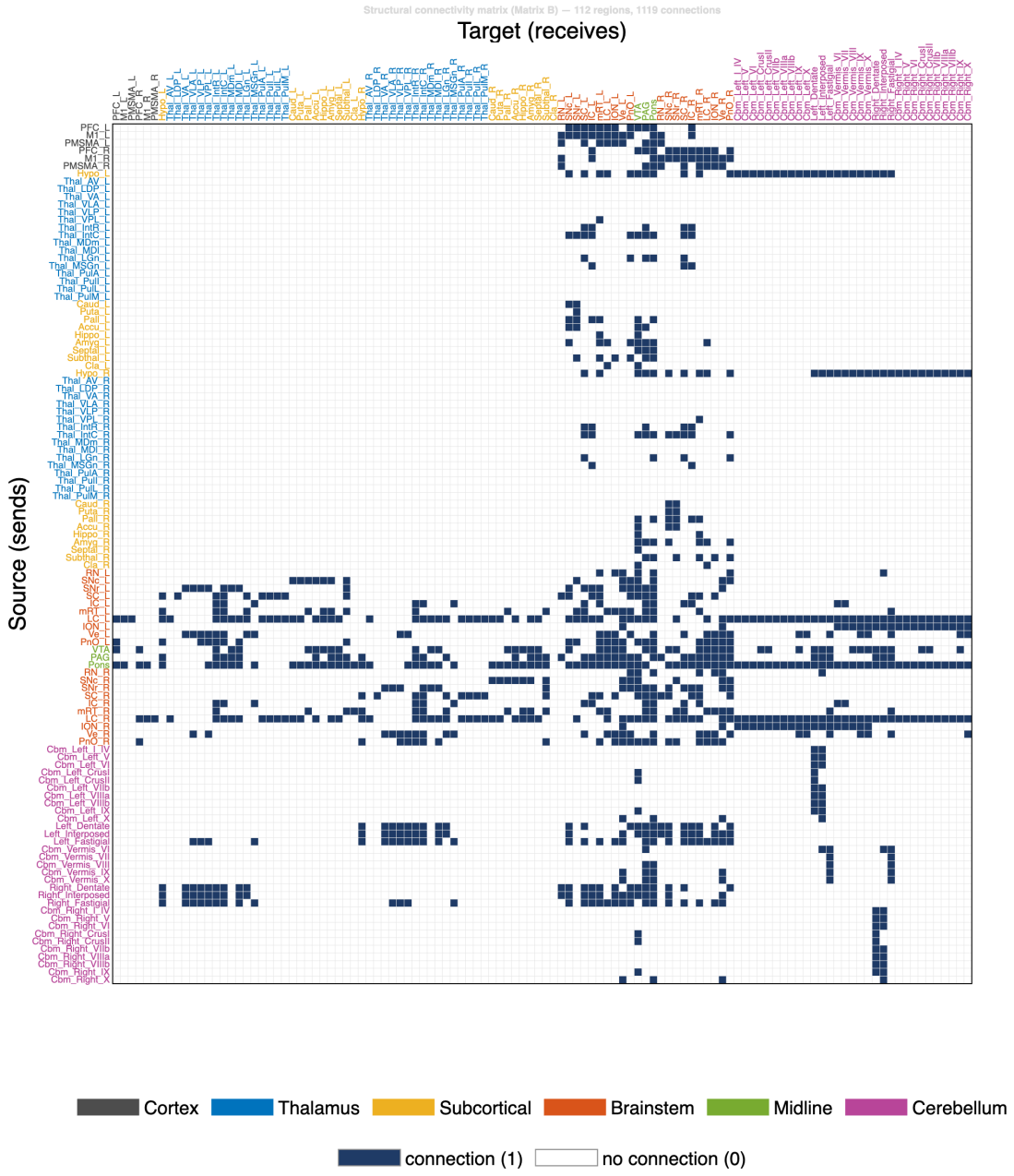


Figure 4.2: Matrix B: all-region connectome matrix, with pons as one region. Out of the 1119 connections, 296 were ipsilateral, reaching only same-side target regions, 120 were contralateral projections, reaching only opposite-side target regions, and 174 were bilateral, reaching both ipsilateral and contralateral target regions. 355 connections involved a midline structure (VTA, PAG, Pons and the five vermis lobules) as source or target. Region labels are color-coded by anatomical system: cortex (grey), thalamus (blue), subcortical (gold), brainstem (orange), midline (green) and cerebellum (magenta)

In the final matrix, Figure 4.3, in which the pons was subdivided into 14 subregions, the network consisted of 139 regions and 1876 directed connections.

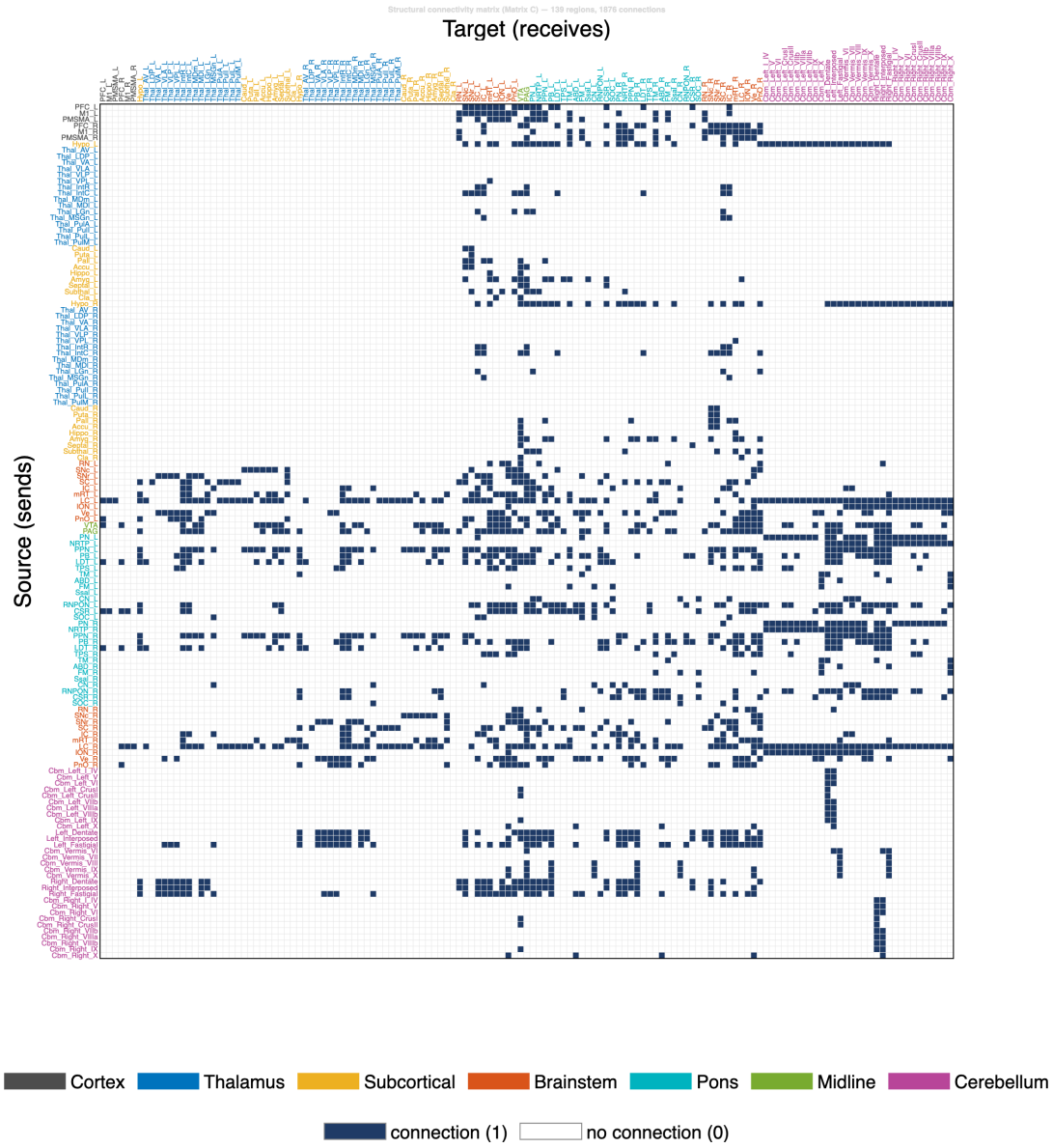


Figure 4.3: Matrix C: all-region connectome matrix with pons segmented into its subnuclei. Out of the 1876 connections, 496 were ipsilateral, reaching only same-side target regions, 192 were contralateral projections, reaching only opposite side target regions, and 441 were bilateral, reaching both ipsilateral and contralateral target regions. 306 connections involved a midline structure (VTA, PAG and the five vermis lobules) as source or target. Region labels are colour-coded by anatomical system: cortex (grey), thalamus (blue), subcortical (gold), brainstem (orange), pons (cyan), midline (green) and cerebellum (magenta)

4.2 Graph theory results

The metrics were derived from the 112-region matrix (Matrix B) and then from the whole 139-region matrix (Matrix C) in order to highlight the significance of treating the pons as a segmented region and the importance of subdividing it into its 14 subnuclei. The results that are reported here focus on the brainstem and the subcortical regions of interest, Tables 4.1 and Table 4.2. For each region, the in-degree, out-degree and total degree, local reciprocity, betweenness centrality, directed clustering coefficient, coreness and trophic level were calculated. In the Table 4.1 the metrics are obtained while considering the pons as one region, while in the Table 4.2 the pons is subdivided, and the metrics are recalculated based on the pons parcellation. The two hemispheres are largely symmetrical in their projections and for this reason, only the left-hemisphere and midline regions are reported in the tables that follow.

Region	In	Out	Tot	Recipr.	Betw.	Clust.	Core	Trophic
Hypo_L	9	32	41	0,281	0,0083	0,311	20	0,761
Thal_AV_L	2	0	2	0,000	0,0000	1,000	2	1,731
Thal_LDP_L	1	0	1	0,000	0,0000	0,000	1	2,408
Thal_VA_L	5	0	5	0,000	0,0000	0,200	5	2,275
Thal_VLA_L	7	0	7	0,000	0,0000	0,333	7	2,269
Thal_VLP_L	7	0	7	0,000	0,0000	0,310	7	2,267
Thal_VPL_L	9	1	10	0,000	0,0000	0,578	10	2,061
Thal_IntR_L	15	5	20	0,250	0,0007	0,624	20	1,794
Thal_IntC_L	14	10	24	0,412	0,0014	0,613	20	1,456
Thal_MDm_L	6	0	6	0,000	0,0000	0,867	6	2,058
Thal_MDl_L	10	0	10	0,000	0,0000	0,711	10	2,143
Thal_LGn_L	6	5	11	0,100	0,0002	0,657	11	1,351
Thal_MSGn_L	6	3	9	0,286	0,0000	0,632	9	1,714
Thal_PulA_L	3	0	3	0,000	0,0000	0,500	3	1,957
Thal_PulI_L	3	0	3	0,000	0,0000	0,500	3	1,957
Thal_PulL_L	3	0	3	0,000	0,0000	0,500	3	1,957
Thal_PulM_L	3	0	3	0,000	0,0000	0,500	3	1,957
Caud_L	4	2	6	0,200	0,0000	0,714	6	1,437
Puta_L	4	1	5	0,000	0,0000	0,750	5	1,643
Pall_L	5	6	11	0,571	0,0003	0,657	11	1,209
Accu_L	6	4	10	0,429	0,0001	0,762	10	1,371
Hippo_L	5	2	7	0,400	0,0000	0,763	7	1,631
Amyg_L	7	8	15	0,875	0,0003	0,786	15	1,063
Septal_L	5	3	8	0,600	0,0000	1,000	8	1,330
Subthal_L	8	6	14	0,556	0,0002	0,744	14	1,424
Cla_L	2	2	4	0,000	0,0000	0,833	4	1,082
RN_L	8	7	15	0,071	0,0004	0,433	13	1,117
SNc_L	20	14	34	0,308	0,0113	0,329	19	1,406

continued on next page

Region	In	Out	Tot	Recipr.	Betw.	Clust.	Core	Trophic
SNr_L	14	18	32	0,231	0,0185	0,352	18	1,300
SC_L	24	21	45	0,250	0,0298	0,306	20	1,408
IC_L	21	14	35	0,458	0,0121	0,355	20	1,561
mRT_L	27	21	48	0,412	0,0221	0,350	20	1,357
LC_L	16	80	96	0,171	0,0548	0,142	20	0,727
ION_L	18	20	38	0,152	0,0125	0,233	18	1,237
Ve_L	26	28	54	0,385	0,0251	0,294	20	1,315
PnO_L	25	22	47	0,424	0,0118	0,396	20	1,320
VTA	42	47	89	0,508	0,1150	0,182	20	1,265
PAG	41	41	82	0,577	0,0584	0,270	20	1,279
Pons	49	87	136	0,462	0,2046	0,151	20	1,045

Table 4.1: Graph-theory metrics for Matrix B, with pons as one segmented single region, highlighted in orange. Left-hemisphere and midline regions are shown. Abbreviations: In, in-degree; Out, out-degree; Tot, total degree; Recip., reciprocity; Betw., normalized betweenness centrality; Clust., clustering coefficient; Core, coreness; Trophic, trophic level.

4.2.1 Effect of unpacking the pons

In the Table 4.1 the pons emerged as the single largest hub of the network with total degree of 136, out-degree of 87, and betweenness of 0.204, exceeding the results of any other region. When the Pons was subdivided into its 14 sub-regions per hemisphere (left and right), Table 4.2, this apparent hub status of the pons was redistributed across the segmented nuclei. The high total degree and betweenness measured for the whole pons were not a property of the structure as a unique region, but the combined contribution of the underlying pontine nuclei, which the representation as a singe node had merged into one artificially dominant region.

Region	In	Out	Tot	Recipr.	Betw.	Clust.	Core	Trophic
Hypo_L	16	45	61	0,298	0,0083	0,298	24	0,826
Thal_AV_L	4	0	4	0,000	0,0000	0,417	4	1,774
Thal_LDP_L	1	0	1	0,000	0,0000	0,000	1	2,323
Thal_VA_L	5	0	5	0,000	0,0000	0,200	5	2,272
Thal_VLA_L	7	0	7	0,000	0,0000	0,333	7	2,269
Thal_VLP_L	7	0	7	0,000	0,0000	0,310	7	2,275
Thal_VPL_L	10	1	11	0,000	0,0000	0,482	11	2,040
Thal_IntR_L	22	5	27	0,174	0,0006	0,486	24	1,767
Thal_IntC_L	20	11	31	0,348	0,0026	0,467	24	1,429
Thal_MDm_L	7	0	7	0,000	0,0000	0,643	7	1,983
Thal_MDl_L	13	0	13	0,000	0,0000	0,558	13	2,045
Thal_LGn_L	6	5	11	0,100	0,0001	0,574	11	1,343
Thal_MSGn_L	9	3	12	0,200	0,0004	0,367	12	1,809
Thal_PulA_L	3	0	3	0,000	0,0000	0,500	3	1,958

continued on next page

Region	In	Out	Tot	Recipr.	Betw.	Clust.	Core	Trophic
Thal_PulI_L	3	0	3	0,000	0,0000	0,500	3	1,958
Thal_PulL_L	3	0	3	0,000	0,0000	0,500	3	1,958
Thal_PulM_L	3	0	3	0,000	0,0000	0,500	3	1,958
Caud_L	5	2	7	0,167	0,0000	0,575	7	1,478
Puta_L	5	1	6	0,000	0,0000	0,600	6	1,652
Pall_L	7	6	13	0,444	0,0003	0,432	13	1,256
Accu_L	7	4	11	0,375	0,0001	0,606	11	1,378
Hippo_L	6	2	8	0,333	0,0000	0,577	8	1,608
Amyg_L	11	13	24	0,500	0,0012	0,507	21	1,008
Septal_L	10	3	13	0,300	0,0000	0,587	13	1,463
Subthal_L	9	8	17	0,308	0,0007	0,443	17	1,308
Cla_L	1	2	3	0,000	0,0000	0,667	3	0,756
RN_L	8	8	16	0,067	0,0004	0,345	16	1,096
SNc_L	24	14	38	0,267	0,0099	0,316	23	1,436
SNr_L	16	20	36	0,200	0,0158	0,302	22	1,235
SC_L	29	27	56	0,244	0,0332	0,254	24	1,323
IC_L	24	18	42	0,448	0,0146	0,255	24	1,492
mRT_L	34	25	59	0,341	0,0224	0,321	24	1,326
LC_L	21	90	111	0,168	0,0547	0,140	24	0,779
ION_L	21	20	41	0,139	0,0081	0,229	22	1,344
Ve_L	33	39	72	0,358	0,0340	0,257	24	1,281
PnO_L	33	25	58	0,349	0,0133	0,357	24	1,321
PN_L	28	29	57	0,118	0,0208	0,168	24	1,320
NRTP_L	24	20	44	0,158	0,0120	0,173	22	1,419
PPN_L	23	56	79	0,317	0,0265	0,210	24	0,881
PB_L	25	45	70	0,522	0,0175	0,328	24	0,970
LDT_L	14	37	51	0,308	0,0063	0,298	24	0,789
TPS_L	8	18	26	0,083	0,0016	0,311	19	0,935
TM_L	16	6	22	0,100	0,0012	0,308	16	1,478
ABD_L	9	4	13	0,444	0,0003	0,419	13	1,745
FM_L	18	6	24	0,143	0,0030	0,293	16	1,673
Ssal_L	9	0	9	0,000	0,0000	0,528	9	2,011
CN_L	11	9	20	0,250	0,0026	0,258	15	1,482
RNPON_L	11	47	58	0,184	0,0061	0,297	24	0,648
CSR_L	22	37	59	0,229	0,0230	0,293	24	0,888
SOC_L	8	6	14	0,400	0,0013	0,305	13	1,522
VTA	45	51	96	0,524	0,0909	0,191	24	1,228
PAG	46	52	98	0,485	0,0616	0,264	24	1,180

Table 4.2: Graph-theory metrics for Matrix C, with pons subdivided into 14 sub-nuclei. Left-hemisphere and midline regions are shown. Abbreviations: In, in-degree; Out, out-degree; Tot, total degree; Recip., reciprocity; Betw., normalized betweenness centrality; Clust., clustering coefficient; Core, coreness; Trophic, trophic level.

4.2.2 Degrees and network hubs

Figure 4.4 depicts the in-degree and the out-degree for selected regions. The total degree of the regions was $k = k_{\text{in}} + k_{\text{out}}$. The most connected regions were the LC (k = 111), the PAG (k = 98), VTA (k = 96), the PPN (k = 79), the Ve (k = 72) and the PB (k = 70), highlighting these structures as the principal hubs of the network. When direction of the connection was taken into account, the LC showed by far the highest out-degree (90), followed by the PPN (56), the PAG (52), the VTA (51), the RNPON (47) and the PB (45), marking these regions as the main brainstem broadcasters, regions that distribute their efferent connections most widely. The highest in-degrees were observed in the PAG (46) and the VTA (45), followed then by the mRT, the VN and finally the PnO, indicating that these regions have a role as major convergence sites in the human brain.

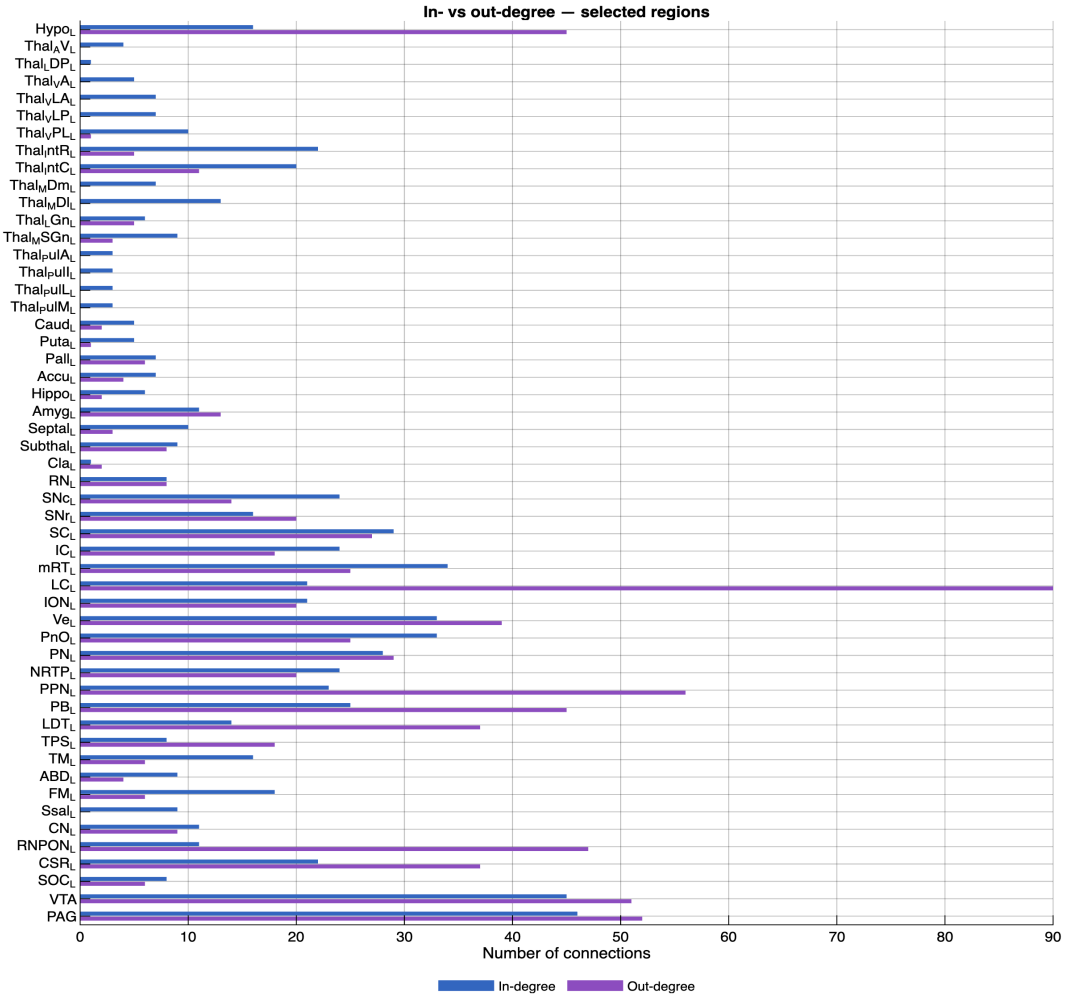


Figure 4.4: In-degree versus out-degree for the selected regions of Matrix C. For each region, the number of incoming connections (in-degree, colored in blue) and outgoing connections (out-degree, colored in purple) is shown.

4.2.3 Betweenness centrality

The highest values of the normalized betweenness were found for the VTA (0.091), the PAG (0.062), and the LC (0.055), followed by the Ve (0.034), the SC (0.033), and the PPN (0.026). These regions therefore act as key relays for communication across the network. Figure 4.5 depicts the normalized values of betweenness centrality of the selected brainstem regions.

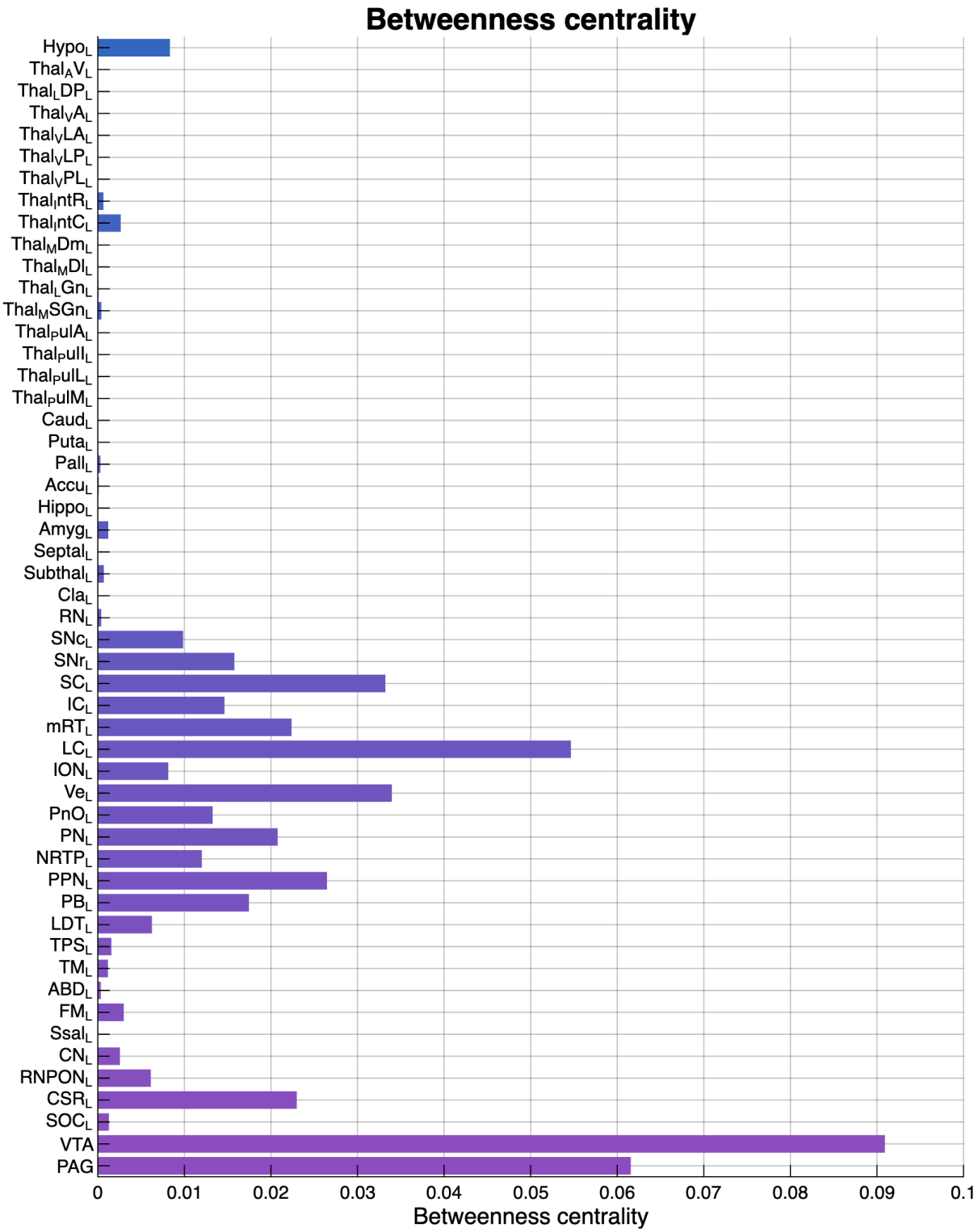
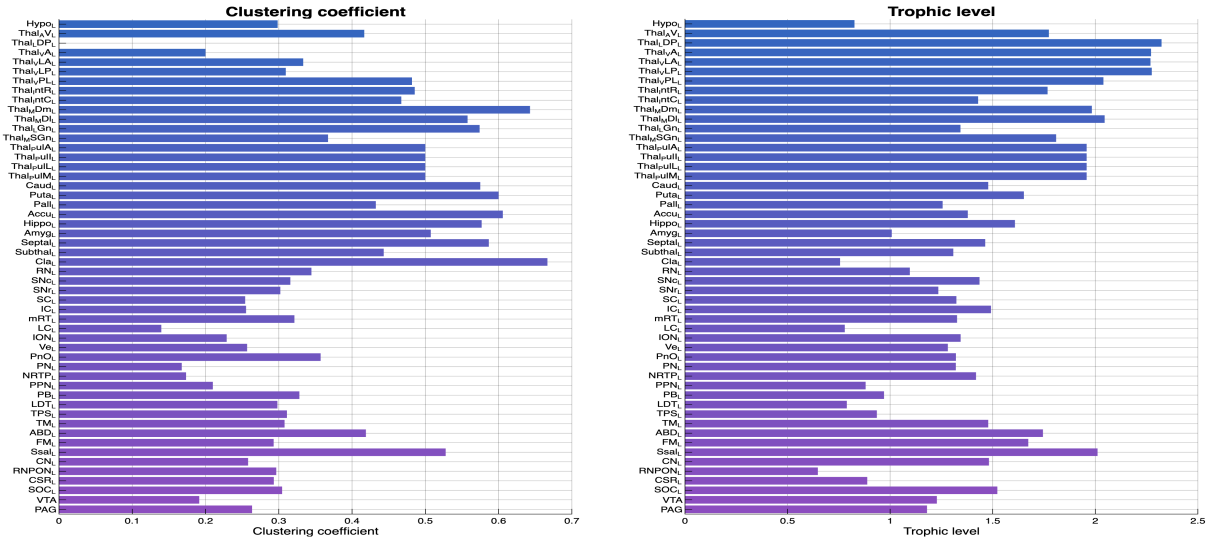


Figure 4.5: Normalized betweenness centrality of each region from Matrix C.

4.2.4 Clustering coefficient, coreness and trophic level

The directed clustering coefficient as shown in Figure 4.6a was highest for regions that were embedded in densely interconnected local circuits, such as the Clau (c=0.667), the Thal_MDm (c=0.643), the Accu (c=0.606), the Put (c=0.60) and the Septal (c=0.587), and lowest for the main broadcasting hubs, including the LC (c=0.14), the PN (c=0.17), the NRTP (c=0.17) and the VTA (c=0.19), whose very wide distributed projections are not locally clustered. It should be noted that these high clustering regions are low-degree nodes, so a high clustering coefficient is expected, since the few existing neighbors are more likely to be mutually connected. In contrast, the main broadcasting hubs, regions with efferent projections that go to many separate targets, combine a very high degree with low clustering, thus reflecting their wide distributed projections. The k-core decomposition resulted in a maximum coreness of 24. Regions that belong to this maximum coreness set, comprised of regions such as the hypothalamus, the intralaminar thalamic nuclei, the SC and IC and the mRT, thus defining the densely interconnected structural core of the network.



(a) (b)

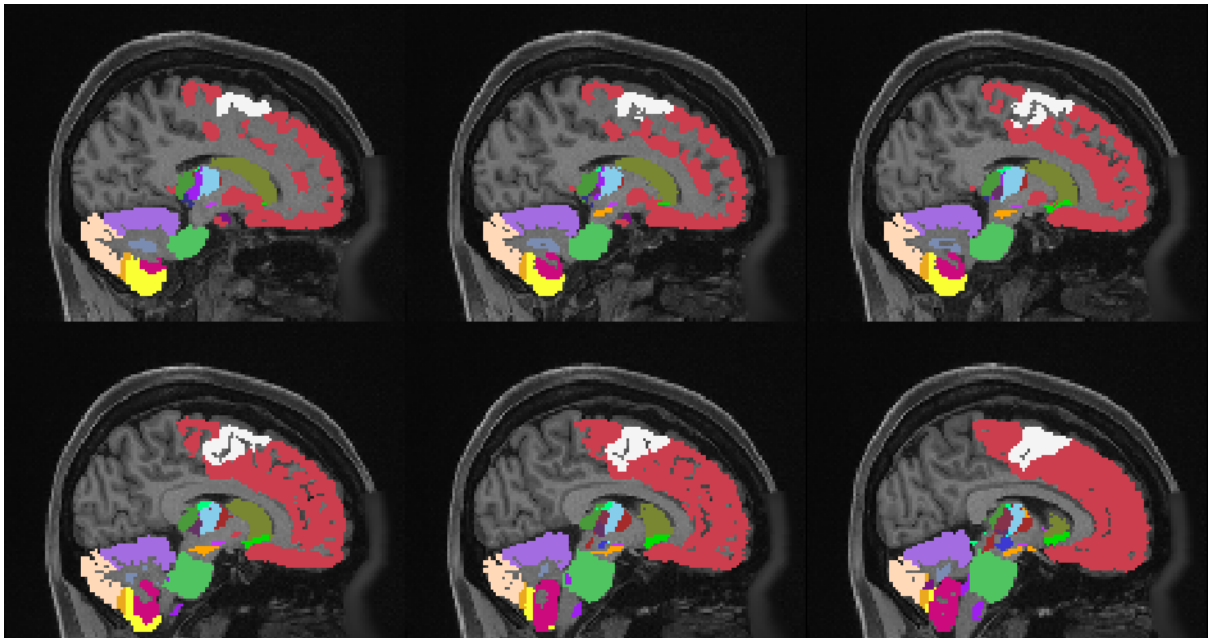
Figure 4.6: **(a)** Clustering coefficient of each region from Matrix C. **(b)** Trophic level of each region from Matrix C.

The trophic level metric analysis, as shown in Figure 4.6b revealed a clear source-to-sink hierarchy of the brainstem regions. The lowest trophic levels derived by the RNPON (0.65), the Clau (0.76), the LC (0.78), the LDT (0.79), and the Hypo (0.83). The highest trophic levels came from the relay thalamic nuclei, particularly the laterodorsal (2.32), ventral lateral posterior (2.28), ventral anterior (2.27), ventral lateral anterior (2.27), and mediodorsal (2.05) nuclei. Consistently, the thalamic nuclei behaved as pure sinks in this network, receiving connections but not sending any. This confirms their position as terminal targets of the brainstem and subcortical afferents included in this work, along with the superior salivatory nucleus.

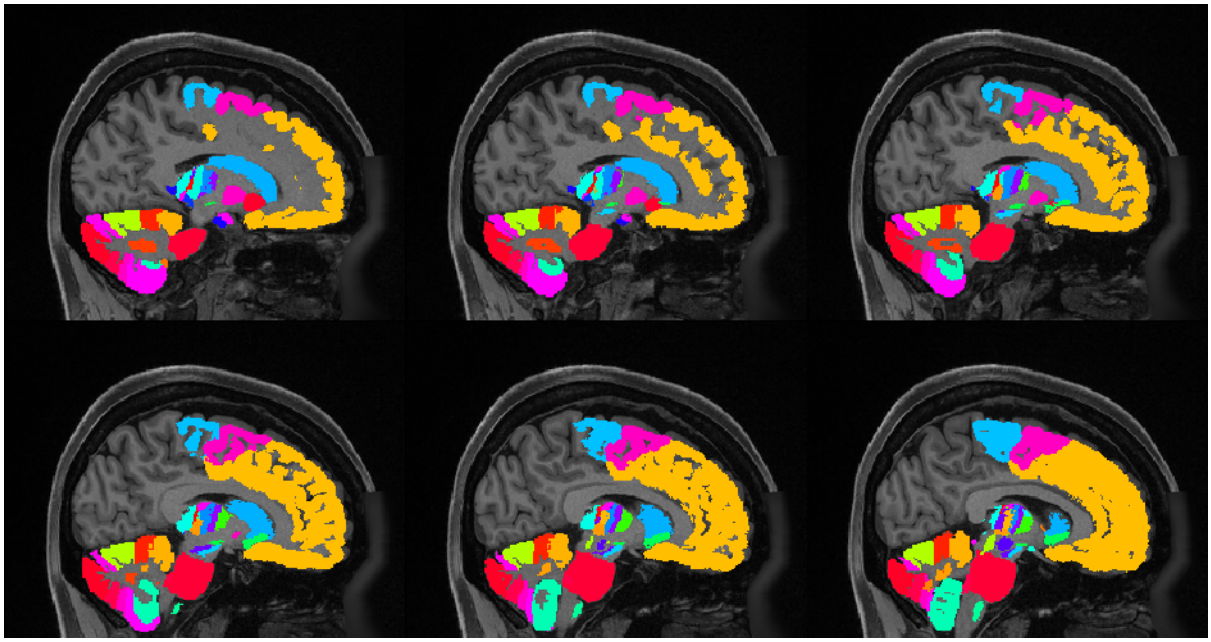
4.3 Atlas and segmentation

4.3.1 Brain Atlases at 1.5 mm and 0.8 mm isotropic resolution

The subject specific atlases were constructed for the subject HCA6053758. The same atlas is presented at two different spatial resolutions, that differ only in voxel size.



(a) 1.5 mm isotropic resolution



(b) 0.8 mm isotropic resolution

Figure 4.7: Labeled atlas overlaid on the subject T1-weighted image, shown across the same six sagittal slices at (a) 1.5 mm and (b) 0.8 mm isotropic resolution. Colors denote the individual atlas regions. Visualized in FSLEyes.

Figure 4.7(a) shows the labeled atlas overlaid on the subject T1-weighted image in the axial, coronal and sagittal planes, at 1.5 mm isotropic resolution. Figure 4.7(b) shows the labeled atlas overlaid on the subject T1-weighted image in the axial, coronal and sagittal planes, at 0.8 mm isotropic resolution. At 0.8 mm the regional boundaries were sharper, and the smaller brainstem nuclei were more finely outlined, whereas at 1.5 mm the labels appeared to be roughly shaped. The atlas comprised 112 regions distributed across five anatomical systems: 6 cortical, 32 thalamic, 20 subcortical, 23 brainstem and 31 cerebellar regions. These regions have a wide range of sizes, from large cortical and cerebellar structures to small brainstem nuclei. Figure 4.8 shows a three-dimensional rendering of the 0.8 mm atlas, with the labeled regions reconstructed as surfaces on the subject's T1-weighted volume.

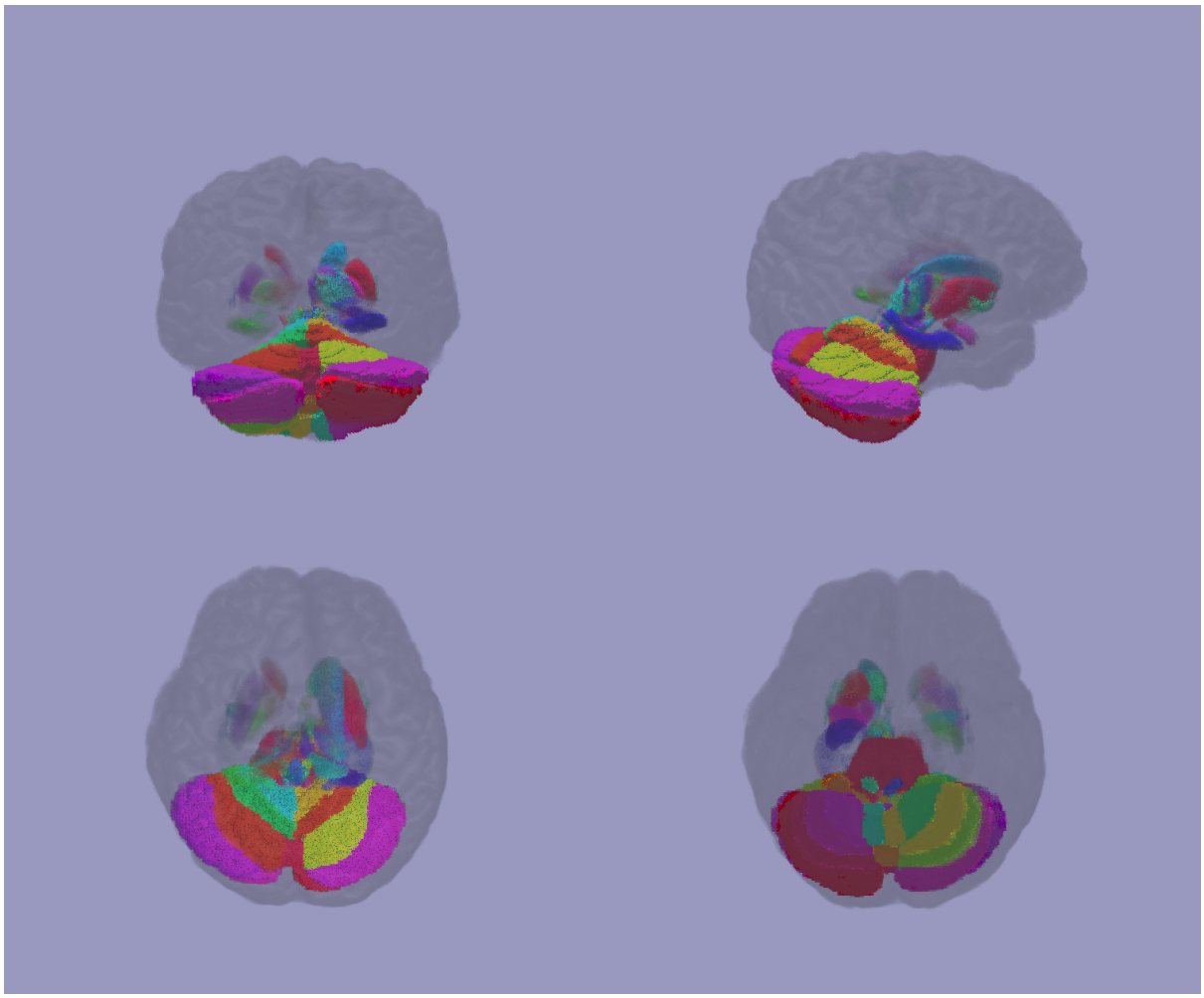
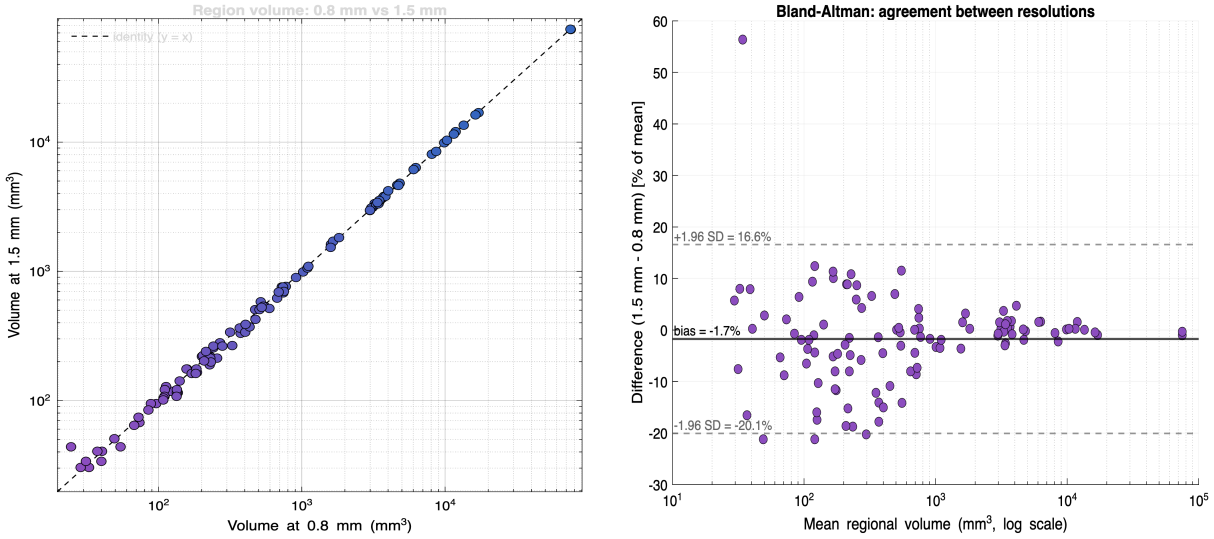


Figure 4.8: Labeled atlas visualized on the subject T1-weighted image at 0.8 mm isotropic resolution as a 3D picture. Visualized in FSLeyes.

4.3.2 Volume analysis at 1.5 mm and 0.8 mm isotropic resolution

Figure 4.9 (a) shows the comparison of the volume of each region measured at 0.8 mm and 1.5 mm isotropic resolution. Overall, the two resolutions yielded highly consistent volume estimates, although the largest relative differences were observed in the smallest regions. Volumes measured at the two resolutions were almost perfectly correlated (ρ = 0.997). The mean percentage difference between the volumes measured at the two resolutions was −1.7% (95% limits of agreement −20.1% to +16.6%). The absolute difference of volume increased with the mean region size between the two resolutions (ρ = +0.62), while the relative difference (%) of volume decreased with region size (ρ = −0.59). Larger regions differed more in absolute numbers but less as a proportion of their size. This underlines that the smallest regions are less reliably measured, as their volumes vary strongly between resolutions relatively to their size.

This agreement is summarized in Figure 4.9 (b).



(a) (b)

Figure 4.9: **(a)** Scatter plot of each region's volume measured at 0.8 mm isotropic resolution (x-axis) against 1.5 mm isotropic resolution (y-axis). **(b)** Bland-Altman plot of the agreement between the two resolutions: each point is one region, the x-axis is the mean of its 0.8 mm and 1.5 mm volumes and the y-axis the percentage difference between them. The solid line marks the mean difference (bias, -1.7%) and the dashed lines the 95% limits of agreement (-20.1% to $+16.6\%$).

Figure 4.10 depicts the percentage volume difference between the two resolutions for each region, expressed relative to the mean of the two measurements. The regions are ordered from smallest to largest based on their volume. The differences are relatively small in larger regions, while the smallest reach variations up to 57%.

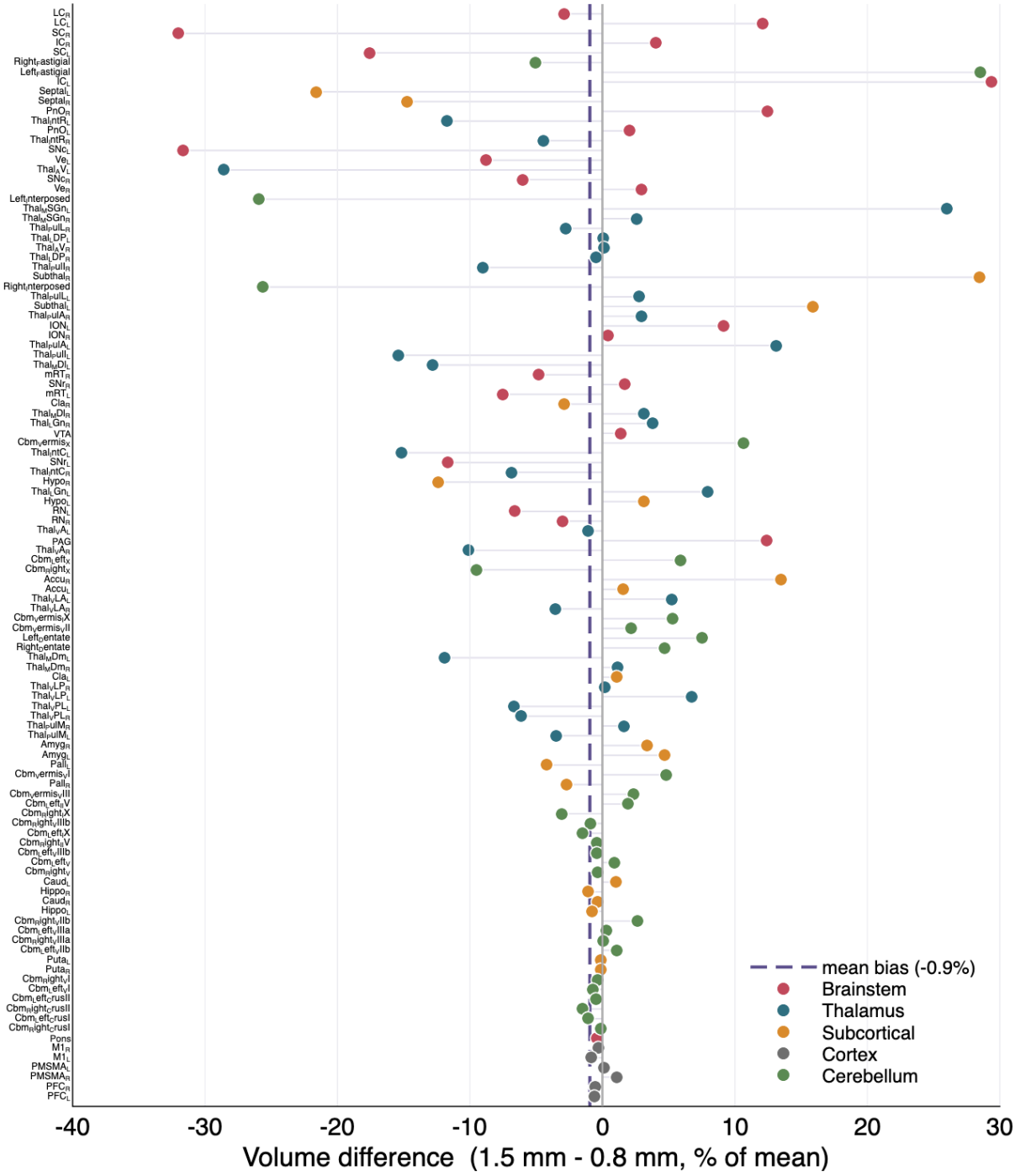


Figure 4.10: Per-region volume difference between the 1.5 mm and 0.8 mm resolutions, expressed relative to the mean of the two measurements, ordered from smallest to largest region.

4.4 Analysis and comparison across tractography configurations

Each of the seven tractography configurations was compared against the literature-based structural connectivity matrix using the confusion-matrix framework described. The results are reported at two levels. The first, considers the whole reconstructed connectome, that is all $N = 9750$ possible directed connections, of which $P = 1119$ are present in the matrix B. Secondly, the brainstem-subcortical set is considered, with $N_Brainstem = 2898$ and $P_Brainstem = 608$.

Across the different configurations, a small set of regions was highlighted for its disproportionate number of missed connections. Ranking regions by their absolute number of missed connections underlined these regions. The LC, both IC and SC, and the deep cerebellar nuclei are the most affected regions, as shown in Figure 4.11.

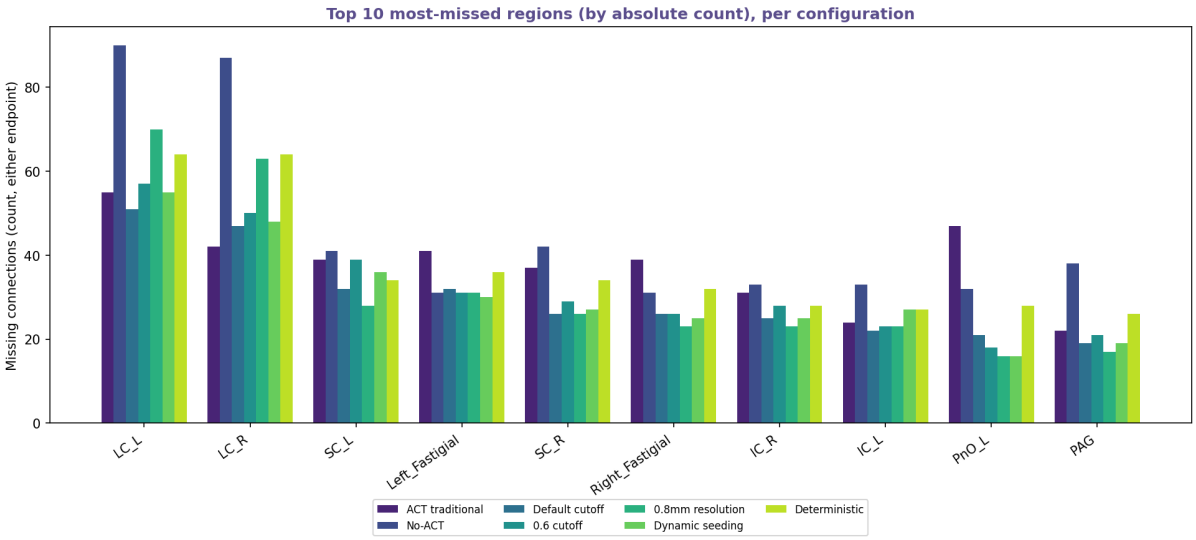


Figure 4.11: The ten regions that hold the highest absolute number of missed connections, shown for each of the seven tractography configurations. The bars give the raw count of a region's matrix B connections that were not reconstructed.

4.4.1 Deterministic tractography analysis

Using the deterministic tractography configuration, 538 of the 1119 (48.07%) Matrix B connections were correctly reconstructed at the all-region level, Table 4.3. While its sensitivity was moderate at 0.481, this configuration had the highest all-region connectome precision of 0.50 and an F1 score of 0.49, Table 4.6. In the brainstem subset as shown in the Table 4.4, precision reached 0.67 and F1 0.594, with an MCC of 0.506, Table 4.8. As in every other configuration, missed connections were concentrated in the brainstem, at 58%, depicted in Figure 4.12, followed by the cerebellum with 23%.

	Tractog +	**Tractog -**
Matrix +	538 (TP)	581 (FN)
Matrix -	535 (FP)	8096 (TN)

Table 4.3: Deterministic: all-region confusion matrix. Matrix +/- indicated presence or absence from the matrix B, while Tractog +/- indicates presence or absence from the reconstructed tracts.

	Tractog +	**Tractog -**
Matrix +	325 (TP)	283 (FN)
Matrix -	160 (FP)	2130 (TN)

Table 4.4: Deterministic: brainstem-subset confusion matrix. Matrix +/- indicated presence or absence from the matrix B, while Tractog +/- indicates presence or absence from the reconstructed tracts.

Metric	**Sens.**	**Prec.**	**Spec.**	**F1**	**MCC**
Value	0.481	0.501	0.938	0.491	0.426

Table 4.6: Deterministic: all-region performance metrics.

Metric	**Sens.**	**Prec.**	**Spec.**	**F1**	**MCC**
Value	0.534	0.670	0.93	0.594	0.506

Table 4.8: Deterministic: brainstem-subset performance metrics.

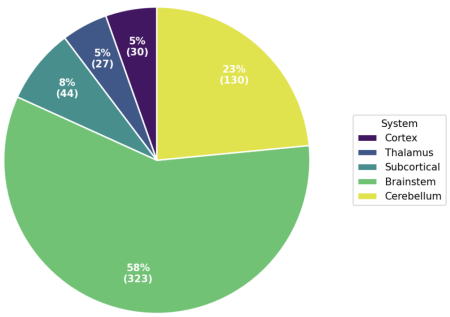


Figure 4.12: Missing connections across different subsets. Region are color-coded by anatomical system: cortex (purple), thalamus (blue), subcortical (teal), brainstem (green) and cerebellum (yellow).

4.4.2 No-ACT tractography analysis

With the No-ACT configuration, 468 of the 1119 (41.82%) Matrix B connections were correctly reconstructed at the all-region connectome level Table 4.9, giving a sensitivity of 0.418, a precision of 0.374 and an F1 score of 0.395 as shown in the Table 4.12. When the analysis was restricted to the 75 region brainstem subset shown in in the Table 4.10, sensitivity was calculated at 0.389 but precision rose to 0.792, resulting in a higher F1 score of 0.522 and MCC of 0.485 than the all-region metrics, Table 4.14. The distribution of missed connections by source system, Figure 4.13 shows that the brainstem accounted for the largest part of failures with 63% of the missed connections coming from brainstem regions, followed by the cerebellum with 17%.

	Tractog +	**Tractog -**
Matrix +	468 (TP)	651 (FN)
Matrix -	784 (FP)	7847 (TN)

Table 4.9: No-ACT: all-region confusion matrix. Matrix +/- indicated presence or absence from the matrix B, while Tractog +/- indicates presence or absence from the reconstructed tracts.

	Tractog +	**Tractog -**
Matrix +	237 (TP)	371 (FN)
Matrix -	62 (FP)	2228 (TN)

Table 4.10: No-ACT: brainstem-subset confusion matrix. Matrix +/- indicated presence or absence from the matrix B, while Tractog +/- indicates presence or absence from the reconstructed tracts.

Metric	**Sens.**	**Prec.**	**Spec.**	**F1**	**MCC**
Value	0.418	0.374	0.909	0.395	0.311

Table 4.12: No-ACT: all-region performance metrics.

Metric	**Sens.**	**Prec.**	**Spec.**	**F1**	**MCC**
Value	0.389	0.792	0.972	0.522	0.485

Table 4.14: No-ACT: brainstem-subset performance metrics.

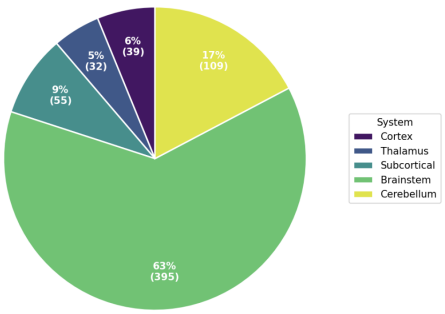


Figure 4.13: No-ACT: Missing connections across different subsets of regions. Region are color-coded by anatomical system: cortex (purple), thalamus (blue), subcortical (teal), brainstem (green) and cerebellum (yellow).

4.4.3 ACT tractography analysis

With the ACT configuration, 507 of the 1119 (45.3%) Matrix B connections were correctly reconstructed at the all-region connectome level Table 4.15, corresponding to a sensitivity of 0.453, a precision of 0.293 and an F1 score of 0.355, as shown in Table 4.20. When the analysis was restricted to the 75 region brainstem subset, Table 4.16, sensitivity was similar at 0.409 but precision rose to 0.684, raising the F1 to 0.512 and the MCC to 0.441, Table 4.20. Missed connections were dominated by the brainstem regions again with 58% and the cerebellum with 23%, shown in Figure 4.14.

	Tractog +	**Tractog -**
Matrix +	507 (TP)	612 (FN)
Matrix -	1223 (FP)	7408 (TN)

Table 4.15: ACT: all-region confusion matrix. Matrix +/- indicated presence or absence from the matrix B, while Tractog +/- indicates presence or absence from the reconstructed tracts.

	Tractog +	**Tractog -**
Matrix +	249 (TP)	359 (FN)
Matrix -	115 (FP)	2175 (TN)

Table 4.16: ACT: brainstem-subset confusion matrix. Matrix +/- indicated presence or absence from the matrix B, while Tractog +/- indicates presence or absence from the reconstructed tracts.

Metric	**Sens.**	**Prec.**	**Spec.**	**F1**	**MCC**
Value	0.453	0.293	0.858	0.355	0.259

Table 4.18: ACT: all-region performance metrics.

Metric	**Sens.**	**Prec.**	**Spec.**	**F1**	**MCC**
Value	0.409	0.684	0.949	0.512	0.441

Table 4.20: ACT: brainstem-subset performance metrics.

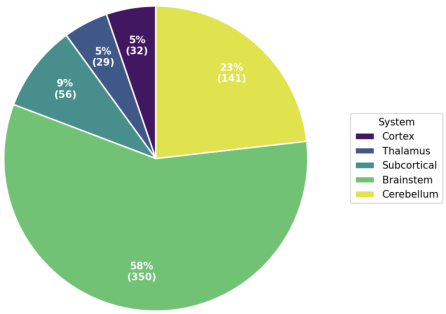


Figure 4.14: ACT: Missing connections across different subsets. Region are color-coded by anatomical system: cortex (purple), thalamus (blue), subcortical (teal), brainstem (green) and cerebellum (yellow).

4.4.4 Default cutoff tractography analysis

With the default-cutoff configuration, 715 of the 1119 (63.89%) Matrix B connections were correctly reconstructed at the all-region connectome level, Table 4.21. It presented the highest sensitivity of any configuration at 0.639, with precision of 0.426 and F1 score of 0.511, Table 4.24. Restricting the analysis to the brainstem subset, Table 4.22 raised precision to 0.582 and F1 to 0.628 with an MCC of 0.522, as shown in Table 4.26, the strongest brainstem performance among the fixed cutoff variants. Missed connections again concentrated in the brainstem and the cerebellum, depicted in Figure 4.15.

	Tractog +	**Tractog -**
Matrix +	715 (TP)	404 (FN)
Matrix -	962 (FP)	7669 (TN)

Table 4.21: Default cutoff: all-region confusion matrix. Matrix +/- indicated presence or absence from the matrix B, while Tractog +/- indicates presence or absence from the reconstructed tracts.

	Tractog +	**Tractog -**
Matrix +	415 (TP)	193 (FN)
Matrix -	298 (FP)	1992 (TN)

Table 4.22: Default cutoff: brainstem-subset confusion matrix. Matrix +/- indicated presence or absence from the matrix B, while Tractog +/- indicates presence or absence from the reconstructed tracts.

Metric	**Sens.**	**Prec.**	**Spec.**	**F1**	**MCC**
Value	0.639	0.426	0.889	0.511	0.446

Table 4.24: Default cutoff: all-region performance metrics.

Metric	**Sens.**	**Prec.**	**Spec.**	**F1**	**MCC**
Value	0.682	0.582	0.869	0.628	0.522

Table 4.26: Default cutoff: brainstem-subset performance metrics.

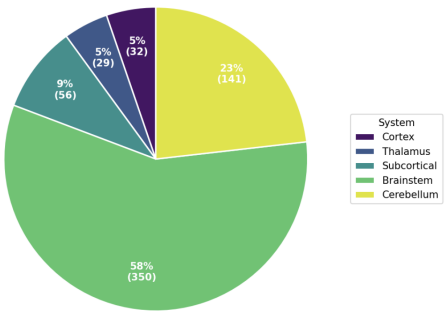


Figure 4.15: Default cutoff: Missing connections across subsets. Region are color-coded by anatomical system: cortex (purple), thalamus (blue), subcortical (teal), brainstem (green) and cerebellum (yellow).

4.4.5 0.06 cutoff tractography analysis

With the configuration using a cutoff value of 0.06, 686 of the 1119 (61.3%) Matrix B connections were correctly reconstructed at the all-region connectome level, Table 4.27, giving a sensitivity of 0.613, a precision of 0.427 and an F1 score of 0.504, Table 4.30. Restricting the analysis to the brainstem subset, as shown in Table 4.28 raised precision to 0.575, sensitivity to 0.646 and F1 to 0.608, with an MCC of 0.498, Table 4.32. As in the other configurations, missed connections were concentrated in the brainstem with 57%, as depicted in Figure 4.16.

	Tractog +	**Tractog -**
Matrix +	686 (TP)	433 (FN)
Matrix -	919 (FP)	7712 (TN)

Table 4.27: 0.6 cutoff: all-region confusion matrix. Matrix +/- indicated presence or absence from the matrix B, while Tractog +/- indicates presence or absence from the reconstructed tracts.

	Tractog +	**Tractog -**
Matrix +	393 (TP)	215 (FN)
Matrix -	290 (FP)	2000 (TN)

Table 4.28: 0.6 cutoff: brainstem-subset confusion matrix. Matrix +/- indicated presence or absence from the matrix B, while Tractog +/- indicates presence or absence from the reconstructed tracts.

Metric	**Sens.**	**Prec.**	**Spec.**	**F1**	**MCC**
Value	0.613	0.427	0.894	0.504	0.435

Table 4.30: 0.6 cutoff: all-region performance metrics.

Metric	**Sens.**	**Prec.**	**Spec.**	**F1**	**MCC**
Value	0.646	0.575	0.873	0.608	0.498

Table 4.32: 0.6 cutoff: brainstem-subset performance metrics.

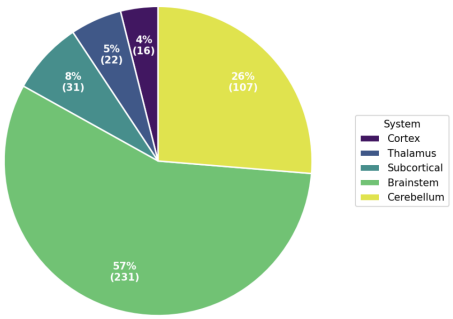


Figure 4.16: Missing connections across different subsets. Region are color-coded by anatomical system: cortex (purple), thalamus (blue), subcortical (teal), brainstem (green) and cerebellum (yellow).

4.4.6 Dynamic seed tractography analysis

With the dynamic seed tractography configuration, 656 of the 1119 (58.62%) Matrix B connections were correctly reconstructed at the all-region connectome level, Table 4.33, giving a sensitivity of 0.586, a precision of 0.478, which is the highest all-region connectome precision of any configuration, and an F1 score of 0.527, as shown in Table 4.36. Restricting the analysis to the 75 region brainstem subset Table 4.34 resulted in the strongest performance of all configurations, with a precision of 0.677, an F1 of 0.668 and an MCC of 0.581, Table 4.38. Missed connections remained concentrated in the brainstem 55%, as shown in Figure 4.17.

	Tractog +	**Tractog -**
Matrix +	656 (TP)	463 (FN)
Matrix -	716 (FP)	7915 (TN)

Table 4.33: Dynamic seeding: all-region confusion matrix. Matrix +/- indicated presence or absence from the matrix B, while Tractog +/- indicates presence or absence from the reconstructed tracts.

	Tractog +	**Tractog -**
Matrix +	401 (TP)	207 (FN)
Matrix -	191 (FP)	2099 (TN)

Table 4.34: Dynamic seeding: brainstem-subset confusion matrix. Matrix +/- indicated presence or absence from the matrix B, while Tractog +/- indicates presence or absence from the reconstructed tracts.

Metric	**Sens.**	**Prec.**	**Spec.**	**F1**	**MCC**
Value	0.586	0.478	0.918	0.527	0.462

Table 4.36: Dynamic seeding: all-region performance metrics.

Metric	**Sens.**	**Prec.**	**Spec.**	**F1**	**MCC**
Value	0.659	0.677	0.916	0.668	0.581

Table 4.38: Dynamic seeding: brainstem-subset performance metrics.

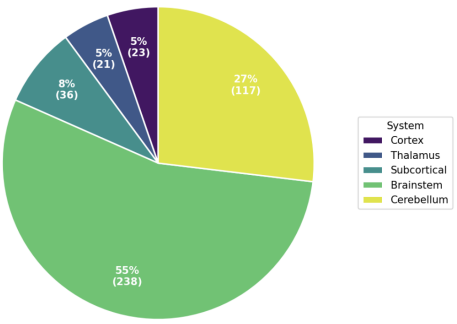


Figure 4.17: Missing connections across different subsets. Region are color-coded by anatomical system: cortex (purple), thalamus (blue), subcortical (teal), brainstem (green) and cerebellum (yellow).

4.4.7 0.8 mm resolution tractography analysis

When the ACT was combined with resolution of 0.8 mm, 663 of the 1119 (59.24%) Matrix B connections were correctly reconstructed at the all-region connectome level, Table 4.39, resulting in a sensitivity of 0.592, a precision of 0.441 and an F1 score of 0.505 summarized in Table 4.42. When the analysis was restricted to the brainstem regions, as shown in Table 4.40, only 410 tracts were reconstructed correctly. This raised sensitivity to 0.674, precision to 0.604 and the F1 score to 0.637, with an MCC of 0.536, Table 4.44. Missed connections remained concentrated in the brainstem with 58%, depicted in Figure 4.18.

	Tractog +	**Tractog -**
Matrix +	663 (TP)	456 (FN)
Matrix -	840 (FP)	7791 (TN)

Table 4.39: 0.8 mm resolution: all-region confusion matrix. Matrix +/- indicated presence or absence from the matrix B, while Tractog +/- indicates presence or absence from the reconstructed tracts.

	Tractog +	**Tractog -**
Matrix +	410 (TP)	198 (FN)
Matrix -	268 (FP)	2022 (TN)

Table 4.40: 0.8 mm resolution: brainstem-subset confusion matrix. Matrix +/- indicated presence or absence from the matrix B, while Tractog +/- indicates presence or absence from the reconstructed tracts.

Metric	**Sens.**	**Prec.**	**Spec.**	**F1**	**MCC**
Value	0.592	0.441	0.902	0.505	0.437

Table 4.42: 0.8 mm resolution: all-region performance metrics.

Metric	**Sens.**	**Prec.**	**Spec.**	**F1**	**MCC**
Value	0.674	0.604	0.882	0.637	0.536

Table 4.44: 0.8 mm resolution: brainstem-subset performance metrics.

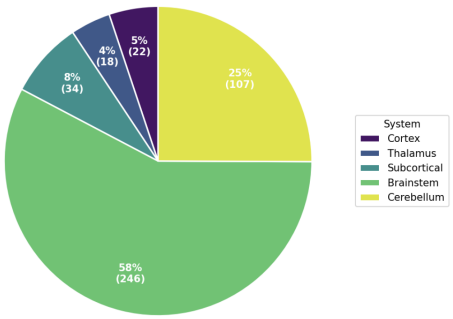


Figure 4.18: Missing connections across different subsets. Region are color-coded by anatomical system: cortex (purple), thalamus (blue), subcortical (teal), brainstem (green) and cerebellum (yellow).

To identify which regions were most difficult to reconstruct, the proportion of each region's reference connections that were missed was computed for all 75 brainstem-subset regions and every configuration, Figure 4.19. Several thalamic nuclei were missed almost entirely, with miss rates approaching 100% across all configurations, whereas the larger brainstem nuclei were more consistently reconstructed.

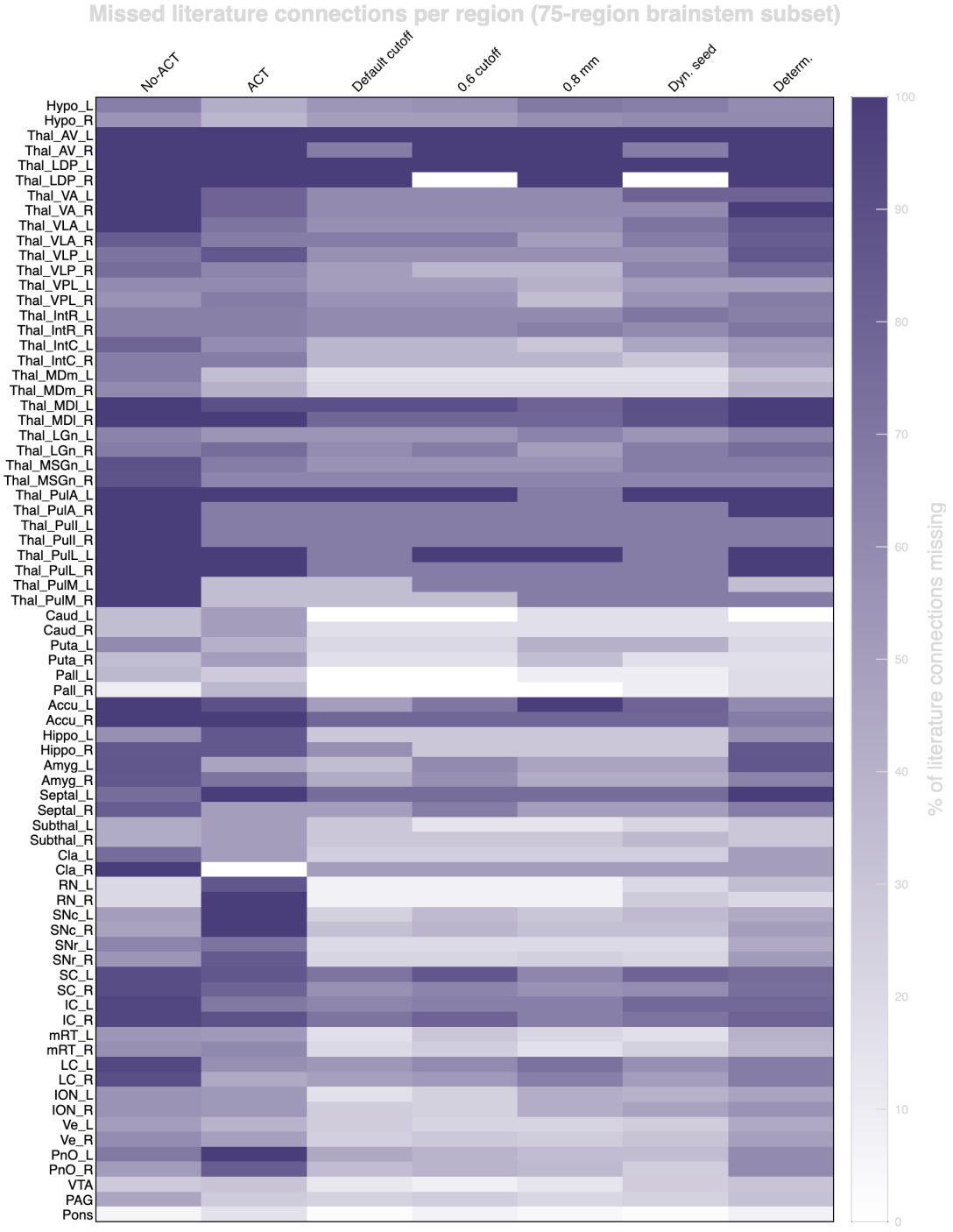


Figure 4.19: Percentage of literature derived connections that were missed for each region of the brainstem-subcortical subset (75 regions) across the seven tractography configurations. Each cell gives the proportion of a region's reference connections that were not reconstructed (missed / expected × 100).Darker shading indicates a higher missing rate.

4.4.8 Region volume as reconstruction failure predictor analysis

The relationship between region volume and the proportion of missed literature-reported connections was assessed across all 112 regions using the best-performing tractography configuration. A significant negative relationship was found: the proportion of missed connections decreased as region volume increased ($\beta_1 = -0.155$ per $\log_{10}$ unit of volume, p = 2.71e-08). This result indicates that larger regions tended to have a lower proportion of missed connections.

The slope quantifies the size of the effect. Because region volume is expressed on a logarithmic scale with base 10, the coefficient $\beta_1 = -0.155$ indicates that each ten fold of increase in region volume is associated with a decrease of approximately 0.15 in the predicted proportion of missed connections. In plain terms, a region ten times larger is expected to have a proportion of missed literature-reported connections that is about 15% points lower.

The coefficient of determination, $R^2 = 0.246$, indicates that the region volume explains about 24% of why the proportion of missed connections is different between regions. The remaining 76% of the variability reflects factors not captured by size. A moderate R^2 of 0.246 indicates that region size is an important but it does not fully account for differences in the proportion of missed connections across regions.

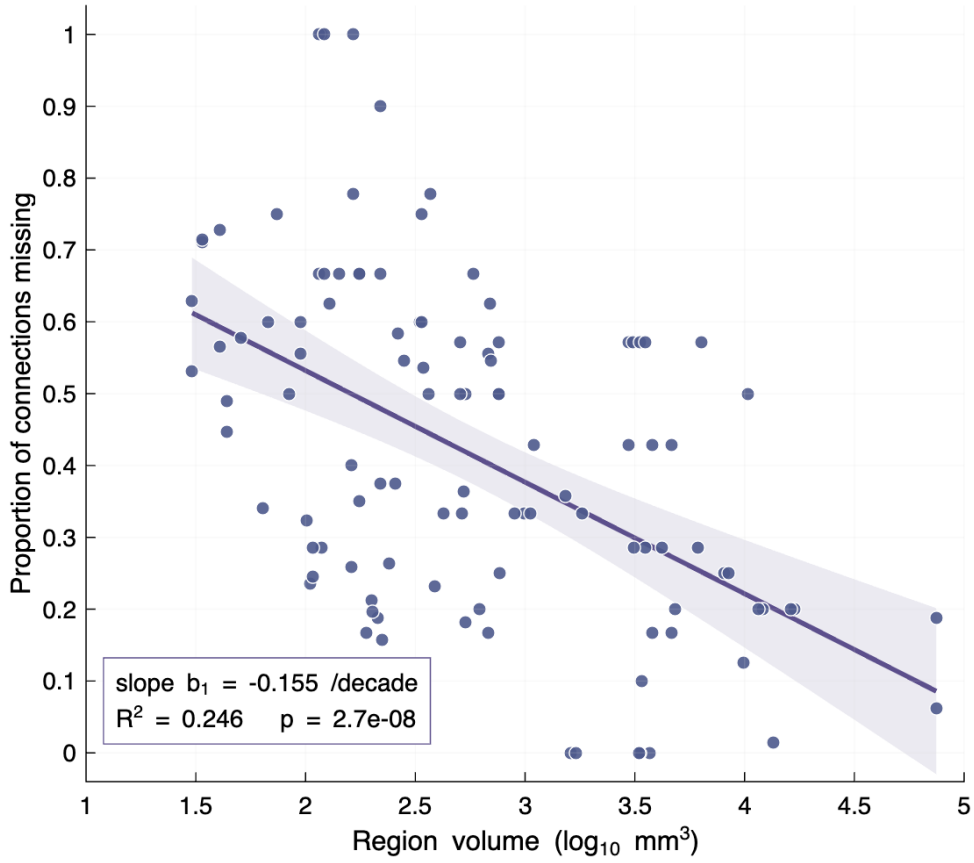


Figure 4.20: Proportion of missed literature connections versus region volume across all 112 regions for the default-cutoff configuration. Each point is one region, the solid line is the least-squares fit and the shaded band is the 95 % confidence interval. ($\beta_1 = -0.155, R^2 = 0.246, p = 2.71e-08$)

This pattern is evident in Figure 4.20. Smaller regions tend to cluster in the upper left of the plot where the proportions of missed connections is higher, whereas larger regions are in the lower right, where the proportion is lower. The fitted regression line captures this negative association, and the scatter of individual regions around it corresponds to the unexplained variance mentioned before.

Chapter 5

Discussion

The brainstem is a significant region of the central nervous system that contains numerous small nuclei that modulate arousal, autonomic regulation, while also being the relay of motor and sensory information between the cerebrum, cerebellum and spinal cord, thus shaping whole-brain dynamics [1] [130]. The brainstem nuclei though, are small, densely interconnected and structurally bilateral, located deep inside the brain, thus making them a difficult target for imaging techniques [130]. Due to its importance as the origin of major neuromodulatory systems, an accurate map of brainstem structural connectivity is of high scientific and clinical value, as its disruption has been linked to a wide range of neurodegenerative, motor and mood disorders. To study these connections non invasively, diffusion weighted MRI can be used [131]. To date, a comprehensive connectome of the human brainstem based only on anatomical evidence has yet to be established. The creation of an anatomy based structural connectivity matrix is an essential scope of this thesis as it provides a directed structural connectivity map of the brainstem, retaining in such way the information about the directionality of the connections.

Existing connectivity models largely derive from diffusion tractography itself. The reconstruction of streamlines from tractography can generate a large number of false positives, i.e., reconstructed connections that biologically don't exist. This limitation is especially severe in the brainstem, where the small size of the nuclei, their close packing, and the proximity to cerebrospinal fluid and bone tissue, decrease the accuracy of the reconstruction. It is evident that assessing how faithfully tractography reproduces true brainstem connectivity and under which acquisition and reconstruction settings is an essential step in neuro-scientific research [132].

To address these problems, this thesis work first assembled the directed, anatomically-informed structural connectivity matrices of the brainstem from literature evidence. Afterwards, a subject specific atlas of brainstem nuclei along with thalamic nuclei, subcortical, cerebellar and some cortical regions, was built in the native T1-weighted space. The literature derived connectome was then used as a reference against seven diffusion tractography configurations, which were

evaluated on their ability to reconstruct accurately tracts, both on the all-regions connectome level and within the brainstem itself. The following sections focus on the interpretation of these results.

5.1 Building an anatomically grounded brainstem connectome

The main finding of the first part of this thesis is the development of an anatomically informed, directed structural connectivity matrix of the brainstem, built entirely from anatomical evidence from literature collection rather than from diffusion MRI data. The literature evidence was derived from human, non-human primates and rodent data, from mainly post-mortem and dissection tract-tracing studies. Its main value lies in the incorporation of information about directionality.

Constructing the matrix at three levels of complexity made it possible to examine brainstem connectivity at increasing anatomical detail. The first level captured the intrinsic connections of the brainstem and its links with subcortical structures (Matrix A). The second level integrated the brainstem and subcortical regions with the cerebellum and few selected cerebral cortical regions (Matrix B). Finally, the third level explored the representation of the pons, by segmenting it to its subnuclei (Matrix C). This parcellation was informative because it exposed differences in connectivity that were hidden when the pons is treated as one region, as distinct nuclei participate in different pathways. The laterality composition of the connectome is consistent with the known organization of the brainstem's pathways. The majority of connections were ipsilateral, which is consistent with the predominantly same sided organization of many brainstem circuits, while a smaller proportion of the projections were contralateral or bilateral, reflecting the decussating and midline crossing pathways that characterize structures such as the colliculi and the pontine systems.

Taken together, these matrices, matrix B and C provide something that has not been provided yet, a directed, anatomically informed matrix of the brainstem's connectivity including intrinsic, subcortical, cerebellar and cerebral connections belonging to the prefrontal and motor cortices. Beyond its descriptive value, this reference makes the following evaluation of tractography possible, since it supplies the anatomical benchmark against which reconstructed connectivity can be compared to. This is a valid contribution with respect to existing work. To date, the most detailed in-vivo connectome of the human brainstem derived straight from diffusion data [131], and therefore comes with the limitations of diffusion MRI. The matrix presented here, is free of those limitations, thus making it suitable as a reference for evaluating diffusion tractography reconstructions.

5.2 Emerging nodes from graph theory

Applying graph theory analysis to the anatomically derived connectome made it possible to move beyond a description of individual connections and to characterize the role of each region within the wider network. In particular, the degree indices allowed us to identify a small set of regions as strong hubs, dominated by the pons, the VTA, the PAG and the LC, regions that are known to serve as major integrative and neuromodulatory centers of the brainstem [133]. The directed nature of the connectome allowed a distinction to be drawn between the roles these hubs play. The LC emerged as a node that sends many more connections than it receives, shown by its high out-degree combined with a low in-degree, and correspondingly occupied the lowest trophic level of the network. This places it at the source end of the connectivity hierarchy and is fully consistent with its known role as the origin of the diffuse noradrenergic system, projecting widely throughout the brain while receiving comparatively few inputs [134]. At the opposite end, the thalamic relay nuclei behaved as pure sinks, with an out-degree of zero and the highest trophic levels, confirming their position as terminal targets of ascending brainstem and subcortical afferents [135]. It should be stressed that this classification is relative to the connections represented in the matrix. In particular, the thalamic relay nuclei appear as pure sinks because their efferent projections are not represented in this work, rather than because they lack outputs in the brain.

The betweenness centrality index further highlighted the VTA, PAG and LC as the principal relay points through which the largest number of shortest paths pass. This is consistent with their known anatomy. The VTA distributes dopaminergic projections from the brainstem to limbic and cortical targets [136], the PAG integrates descending inputs from the forebrain and relays them to lower brainstem circuits controlling pain and autonomic function [137], and the LC broadcasts noradrenergic signals from the brainstem to the entire brain [134].

The clustering coefficient and the k-core decomposition described the local and core organization of the network. Clustering was the highest for small regions embedded in tightly interconnected local circuits, for example Clau, Accu and Put, and the lowest for the main broadcasting hubs, such as LC, PN, PAG and NRTP, whose wide and distributed projections are by definition not locally clustered, Figure 4.6a. The k-core analysis identified a densely interconnected structural core, comprising the Hypo, the intralaminar thalamic nuclei, the SC, the IC and the mRT.

Taken together, these metrics reproduce the known functional organization of the brainstem from anatomical data alone, since the roles these metrics assign to each region agree with the roles known from physiological evidence. In conclusion, all these graph theoretical results demonstrate that the directed connectome captures biologically meaningful roles, distinguishing neuromodulatory broadcasters, integrative relays and terminal targets [138].

5.3 How resolution limits the definition of small brainstem nuclei

A subject-specific atlas of the 112 regions of interest was reconstructed at two different isotropic resolutions, having a voxel of 1.5 mm or 0.8 mm per side. The regional volumes were calculated for all the parcellations and compared between the different resolutions, in order to assess how strongly it affects the definition of these structures. The two resolutions were in close agreement: the mean difference was −1.7%, with 95% limits of agreement from −20.1% to +16.6%. Specifically, the difference per region decreased with increasing region size, Figure 4.9b. The largest structures were measured almost identical, while the smallest nuclei, such as the LC, differed by up to 57%. This behavior indicates the fact that, in a very small region, an inconsistency of a few voxels represents a large fraction of its total volume. In conclusion, the segmentation of small brainstem nuclei is sensitive to acquisition resolution as shown by the analysis. This is consistent with recent studies that suggest that the optimal resolution depends on the size of the structure of interest [139]. Large pathways can be captured at coarse resolutions, but the small brainstem nuclei require finer spatial sampling, as it was highlighted by the differences found here.

5.4 Choosing the proper tractography configuration based on performance

The comparison of the seven configurations against the anatomical reference matrix showed that no single setting was optimal across all criteria, and that “the best configuration” depends on what is being prioritized. In this work, the main goal was the identification of the configuration that maximizes the reconstruction of true anatomical connections. Thus, the default-cutoff configuration performed best. It produced the largest number of correctly reconstructed connections, Tables 4.21 and 4.22, and the highest sensitivity, Figures 4.24 and 4.26. However, this came at the cost of a large number of false positives, so its precision was moderate. At the same time, the dynamic seed configuration, emerged as the best, if the goal was to identify the best balance between recovering true connections and rejecting false ones. It scored the highest precision and the highest F1 score and MCC of all configurations at both all-region connectome and brainstem levels, Figures 4.36 and 4.38. Dynamic seeding represents the most ”reliable” overall performance, producing a connectome in which a reconstructed connection is most likely to be genuinely true, even though it recovers slightly fewer true connections than the default cutoff.

These two configurations reflect the two competing demands placed on tractography. The default cutoff favors completeness of the reconstruction recovering the greatest number of connections, while dynamic seeding favors confidence, ensuring that the connections it retains are most likely

trustworthy. At the opposite extreme, traditional ACT and tracking without ACT performed worst, with the former producing an excess of false positives and the other failing to recover a large part of the true connections.

A consistent finding across every configuration was that reconstruction was more precise within the brainstem-brainstem and brainstem-subcortical subset than across the all-region connectome. This indicates that a substantial share of the false positives came from false connections between the brainstem and regions outside this subset, rather than from within the brainstem itself, and that once the analysis was restricted to brainstem-brainstem and brainstem-subcortical connectivity the reconstructions became more trustworthy. Nevertheless, this improvement in precision was accompanied by only modest sensitivity, meaning that many true brainstem involved connections were still missed.

The most important problem highlighted by this analysis is that the tracts of a specific group of structures were systematically ”under-reconstructed” regardless of the configuration used. In absolute numbers, the largest number of missed connections involved the LC, both the SC and IC, the PnO and the deep cerebellar nuclei. In relative numbers, the miss rates per region, Figure 4.19, show that tracts from several thalamic nuclei were hardly reconstructed at all, with their miss rates approaching 100% across every configuration. This failure is explained by the size of each region. The regions with the most missed connections are among the smallest structures in the subject atlas, and smaller regions were missed significantly more often ($\rho = -0.49$, Section 4.4.8). The fact that the high rate of missed connections is found across all configurations points to the resolution limit as the main cause, rather than to any single tractography configuration setting.

5.5 Limitations

Two main limitations should be taken into account when interpreting the previous results. First, the tractography evaluation was performed on a single subject, so the reported performance figures cannot yet account for inter-individual variability, and the conclusions regarding the optimal configuration will require confirmation in a larger cohort. Second, the anatomical reference matrix, although assembled carefully from the literature, it is not completely reliable. A big part of the available connectivity evidence derives from animal tracer studies, while human anatomical data remain sparse. For this reason, the absence of a connection in the reference does not guarantee its absence also in the human brain and its existence does not guarantee that pathways described in animals are biologically conserved across species. This cross-species uncertainty is more relevant for structures and pathways that are not evolutionarily conserved across different species.

Furthermore, a significant limitation derives from the small size of the brainstem nuclei them-

selves. Even at 0.8 mm isotropic resolution, these structures occupy only a few voxels and lie close to cerebrospinal fluid and bone tissue (clivus bone, for certain pontine nuclei), so they are strongly affected by partial volume effects and low signal-to-noise ratio. The volume comparison that was conducted confirmed this susceptibility to spatial resolution, with the smallest nuclei showing the largest differences between the two resolutions. These findings suggest that uncertainty in defining the regions of interest may contribute to some of the reconstruction failures reported in this work, rather than these reflecting a true absence of a brain pathway.

5.6 Future perspectives

A first direction for future work comes directly from the observation that none of the examined tractography configurations was able to reconstruct the full set of connections that are present in the anatomical reference matrix. Before an optimal configuration can be confidently identified, it is worth establishing how much of this incomplete reconstruction is caused by the fine segmentation of the atlas and the small size of the regions. When a region is only a few voxels, seeding and streamline termination become less reliable, and genuine connections may be eventually missed. Then a next step would be to test a less fine parcellation, with fewer and larger regions, for example the thalamus subdivided into fewer nuclei. Then, assess whether this improves the reconstruction of known anatomical connections. This would ensure that later comparisons between the configurations will reflect genuine differences in tractography performance, rather than the influence of region size.

Having identified which tractography configuration best reproduces the anatomical reference, i.e., the default cutoff configuration, the next step is to apply that optimal extraction method to a larger cohort of subjects, so that the findings obtained here in a single subject can be generalized. Because tractography inevitably produces a large number of false positives, each connection would be checked against the literature-derived connectome and against known anatomical priors, and those that are biologically implausible would be removed. Performed systematically across many subjects, this curation can be formalized into an automated, anatomy rule based procedure, removing the need to inspect every tract individually. Because the plausibility rules will be applied automatically, each reconstructed connection no longer has to be checked manually, one tract at a time. This makes the curation faster, more objective and reproducible across subjects. The longer term aim is to develop a standardized and reproducible framework for directed structural connectivity reconstruction of the hindbrain, in which diffusion MRI supplies subject specific connection strengths while anatomical and physiological evidence supplies the information diffusion cannot recover, such as directionality, laterality and the synaptic nature of each connection. Encoding excitatory and inhibitory characteristics directly in the connectome would extend the model beyond topology towards a more physiologically bounded representation of the brainstem's circuits.

Then, the next step is to move from the binary connectome produced here to a weighted one, in which quantitative connection strengths are assigned to the surviving connections. This would allow the anatomically curated and weighted connectome to be compared against signal-based state-of-the-art filtering methods such as SIFT and COMMIT [140][141], using the literature directed matrix as the anatomical reference and a panel of graph theory metrics. Such a comparison would clarify whether anatomical filtering and signal-based weighting are competitive approaches or complementary stages of a single optimal pipeline.

Finally, the functional impact of these refinements can be assessed through biophysical whole-brain simulation. Virtual brain models, such as The Virtual Brain [142], simulate large scale neural dynamics from a structural connectome and generate the corresponding functional connectivity, which can then be compared with empirically measured functional connectivity. Using a standard symmetric connectome versus an anatomically constrained directed connectome as structural inputs to the Virtual Brain [142], it would be possible to test quantitatively whether the physiological corrections, improve the agreement between simulated and empirical brain dynamics. This would establish whether more accurate hindbrain connectivity translates into more faithful simulated brain dynamics. Figure 5.1 depicts the order of the previously mentioned steps.

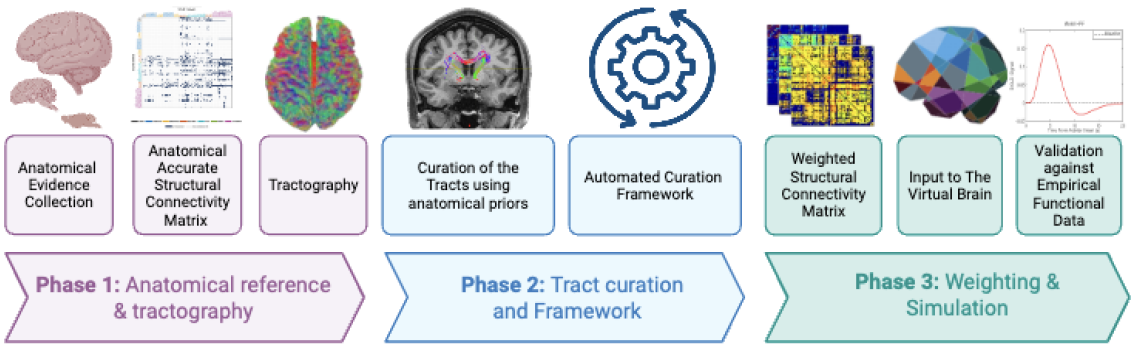


Figure 5.1: Proposed pipeline for building and validating an anatomically-informed brainstem connectome. The workflow is organized into three phases. In Phase 1 (anatomical reference and tractography), anatomical evidence is collected from the literature to assemble a directed, anatomically-accurate structural connectivity matrix, which serves as the reference against which diffusion tractography is evaluated. In Phase 2 (tract curation), the reconstructed tracts are curated using anatomical priors within an automated curation framework. In Phase 3 (weighting and simulation), the matrix is weighted and used as input to The Virtual Brain for whole-brain simulation, whose output is validated against empirical functional data. Created with BioRender.com.

Chapter 6

Conclusions

This thesis aimed to build a directed, anatomically informed structural connectome of the human brainstem and to use it as a reference against which diffusion tractography could be evaluated. The work produced three main findings.

1. An extensive review of tracer based and anatomical literature that was transferred into a binary, directed connectivity matrix of the brainstem and its subcortical connections, which was then integrated with brainstem-cerebellum, cerebellum-cerebellum and brainstem-cortex connections into a whole brain matrix. This reference retains the directionality and laterality of each projection and to our knowledge, represents one of the most detailed anatomically grounded directed matrices of hindbrain connectivity.

2. A graph theory analysis of this connectome, which reflected the biologically meaningful organization of the brainstem/hindbrain.

3. The comparison of seven tractography configurations against the anatomical reference. Based on this work's aim, the thesis showed that the best performing configurations achieve a good compromise between True Positive and False Positive reconstructions, with the default-cutoff configuration giving the most complete reconstruction of tracts. Overall, a specific group of small structures (i.e., the LC, the SC and IC, the PN and the deep cerebellar nuclei) had the highest rate of missed tracts, which were not reconstructed by tractography. The volume analysis confirmed that the definition of these small nuclei is sensitive to spatial resolution, identifying region size as a possible predictor of reconstruction failure.

Acknowledgements

I would like to express my sincere gratitude to my supervisor, Prof.ssa Fulvia Palesi, for giving me the opportunity to work on this project and for her guidance and support throughout this thesis.

I am also grateful to my co-supervisors, Dott.ssa Marta Gaviraghi and Dott.ssa Eleonora Lupi, for their help, their detailed feedback and the time they dedicated during every stage of this work.

Finally, I wish to thank my family and my friends, for their unconditional support and encouragement throughout my studies as this achievement would not have been possible without them.

''As long as the brain is a mystery, the universe, the reflection of the structure of the brain, will also be a mystery.''

- Santiago Ramón y Cajal

References

[1] Hayden Basinger and Jeffery P. Hogg. ‘‘Neuroanatomy, Brainstem’’. eng. In: *StatPearls*. Treasure Island (FL): StatPearls Publishing, 2026. URL: http://www.ncbi.nlm.nih.gov/books/NBK544297/.

[2] Rudolf Nieuwenhuys, Jan Voogd, and Christiaan van Huijzen. ‘‘The Human Central Nervous System, 4th ed.’’ In: *American Journal of Neuroradiology* 29.5 (2008). Ed. by American Society of Neuroradiology, e39–e39. ISSN: 0195-6108. DOI: 10.3174/ajnr.A0991. URL: https://www.ajnr.org/content/29/5/e39.

[3] ‘‘Essential Clinical Neuroanatomy’’. en. In: *Essential Clinical Neuroanatomy*. Ed. by Thomas H. Champney. 1st ed. Wiley, Aug. 2023. ISBN: 978-1-394-32204-6. DOI: 10.1002/9781394322046.fmatter. URL: https://onlinelibrary.wiley.com/doi/10.1002/9781394322046.fmatter.

[4] Sara Sciacca et al. ‘‘Midbrain, pons, and medulla: Anatomy and syndromes’’. In: *Radiographics* 39.4 (July 2019), pp. 1110–1125. ISSN: 15271323. DOI: 10.1148/rg.2019180126.

[5] Barbara E. Jones. ‘‘Arousal and sleep circuits’’. en. In: *Neuropsychopharmacology* 45.1 (Jan. 2020), pp. 6–20. ISSN: 0893-133X, 1740-634X. DOI: 10.1038/s41386-019-0444-2. URL: https://www.nature.com/articles/s41386-019-0444-2.

[6] Clifford B Saper and Patrick M Fuller. ‘‘Wake–sleep circuitry: an overview’’. en. In: *Current Opinion in Neurobiology* 44 (June 2017), pp. 186–192. ISSN: 09594388. DOI: 10.1016/j.conb.2017.03.021. URL: https://linkinghub.elsevier.com/retrieve/pii/S095943881630246X.

[7] Vijay P.B. Grover et al. ‘‘Magnetic Resonance Imaging: Principles and Techniques: Lessons for Clinicians’’. en. In: *Journal of Clinical and Experimental Hepatology* 5.3 (Sept. 2015), pp. 246–255. ISSN: 09736883. DOI: 10.1016/j.jceh.2015.08.001. URL: https://linkinghub.elsevier.com/retrieve/pii/S0973688315004156.

[8] Joseph Yuan-Mou Yang et al. ‘‘Diffusion MRI tractography for neurosurgery: the basics, current state, technical reliability and challenges’’. In: *Physics in Medicine & Biology* 66.15 (Aug. 2021), 15TR01. ISSN: 0031-9155, 1361-6560. DOI: 10.1088/1361-6560/ac0d90. URL: https://iopscience.iop.org/article/10.1088/1361-6560/ac0d90.

[9] M. Horbruegger et al. ‘‘Anatomically constrained tractography facilitates biologically plausible fiber reconstruction of the optic radiation in multiple sclerosis’’. en. In: *NeuroImage: Clinical* 22 (2019), p. 101740. ISSN: 22131582. DOI: 10.1016/j.nicl.2019.101740. URL: https://linkinghub.elsevier.com/retrieve/pii/S2213158219300907.

[10] Robert E. Smith et al. ‘‘Anatomically-constrained tractography: Improved diffusion MRI streamlines tractography through effective use of anatomical information’’. en. In: *NeuroImage* 62.3 (Sept. 2012), pp. 1924–1938. ISSN: 10538119. DOI: 10.1016/j.neuroimage.2012.06.005. URL: https://linkinghub.elsevier.com/retrieve/pii/S1053811912005824.

[11] Danielle S Bassett and Olaf Sporns. ‘‘Network neuroscience’’. en. In: *Nature Neuroscience* 20.3 (Mar. 2017), pp. 353–364. ISSN: 1097-6256, 1546-1726. DOI: 10.1038/nn.4502. URL: https://www.nature.com/articles/nn.4502.

[12] Mikail Rubinov and Olaf Sporns. ‘‘Complex network measures of brain connectivity: Uses and interpretations’’. en. In: *NeuroImage* 52.3 (Sept. 2010), pp. 1059–1069. ISSN: 10538119. DOI: 10.1016/j.neuroimage.2009.10.003. URL: https://linkinghub.elsevier.com/retrieve/pii/S105381190901074X.

[13] Vikram Shenoy Handiru et al. ‘‘Graph-theoretical analysis of EEG functional connectivity during balance perturbation in traumatic brain injury: A pilot study’’. en. In: *Human Brain Mapping* 42.14 (Oct. 2021), pp. 4427–4447. ISSN: 1065-9471, 1097-0193. DOI: 10.1002/hbm.25554. URL: https://onlinelibrary.wiley.com/doi/10.1002/hbm.25554.

[14] N. Ulfig and W. Y. Chan. ‘‘Differential expression of calcium-binding proteins in the red nucleus of the developing and adult human brain’’. eng. In: *Anatomy and Embryology* 203.2 (Feb. 2001), pp. 95–108. ISSN: 0340-2061.

[15] Gianpaolo Antonio Basile et al. ‘‘Red nucleus structure and function: from anatomy to clinical neurosciences’’. eng. In: *Brain Structure & Function* 226.1 (Jan. 2021), pp. 69–91. ISSN: 1863-2661. DOI: 10.1007/s00429-020-02171-x.

[16] Y. Yasui et al. ‘‘Projections from the red nucleus to the parvicellular reticular formation and the cervical spinal cord in the rat, with special reference to innervation by branching axons’’. eng. In: *Brain Research* 923.1-2 (Dec. 2001), pp. 187–192. ISSN: 0006-8993. DOI: 10.1016/s0006-8993(01)03196-1.

[17] Xun-Bei Shi et al. ‘‘Whole-brain monosynaptic outputs and presynaptic inputs of GABAergic neurons in the vestibular nuclei complex of mice’’. In: *Frontiers in Neuroscience* 16 (Aug. 2022), p. 982596. ISSN: 1662-453X. DOI: 10.3389/fnins.2022.982596. URL: https://www.frontiersin.org/articles/10.3389/fnins.2022.982596/full.

[18] S.J. Shammah-Lagnado et al. ‘‘Afferent connections of the nuclei reticularis pontis oralis and caudalis: A horseradish peroxidase study in the rat’’. en. In: *Neuroscience* 20.3 (Mar. 1987), pp. 961–989. ISSN: 03064522. DOI: 10.1016/0306-4522(87)90256-9. URL: https://linkinghub.elsevier.com/retrieve/pii/0306452287902569.

[19] Yi He et al. ‘‘A red nucleus–VTA glutamate pathway underlies exercise reward and the therapeutic effect of exercise on cocaine use’’. In: *Science Advances* 8.35 (Mar. 2026), eabo1440. DOI: 10.1126/sciadv.abo1440. URL: https://doi.org/10.1126/sciadv.abo1440.

[20] Deviana David, Hugo Nusselder, and Marylka Yoe Uusisaari. ‘‘Anatomical and functional examination of superior colliculus projections to the inferior olivary in mice’’. en. In: *Brain Structure and Function* 231.1 (Dec. 2025), p. 2. ISSN: 1863-2661. DOI: 10.1007/s00429-025-03032-1. URL: https://link.springer.com/10.1007/s00429-025-03032-1.

[21] Tadashi Isa et al. ‘‘The tectum/superior colliculus as the vertebrate solution for spatial sensory integration and action’’. en. In: *Current Biology* 31.11 (June 2021), R741–R762. ISSN: 09609822. DOI: 10.1016/j.cub.2021.04.001. URL: https://linkinghub.elsevier.com/retrieve/pii/S0960982221004796.

[22] Jeffery A. Winer et al. ‘‘Descending projections to the inferior colliculus from the posterior thalamus and the auditory cortex in rat, cat, and monkey’’. eng. In: *Hearing Research* 168.1-2 (June 2002), pp. 181–195. ISSN: 0378-5955. DOI: 10.1016/s0378-5955(02)00489-6.

[23] Tetsufumi Ito and Manuel S Malmierca. ‘‘Neurons, Connections, and Microcircuits of the Inferior Colliculus’’. In: *The Mammalian Auditory Pathways: Synaptic Organization and Microcircuits*. Ed. by Douglas L Oliver et al. Cham: Springer International Publishing, 2018, pp. 127–167. ISBN: 978-3-319-71798-2. DOI: 10.1007/978-3-319-71798-2{_}6. URL: https://doi.org/10.1007/978-3-319-71798-2_6.

[24] R. A. Burne et al. ‘‘The tectopontine projection the the rat with comments on visual pathways to the basilar pons’’. eng. In: *The Journal of Comparative Neurology* 202.2 (Oct. 1981), pp. 287–307. ISSN: 0021-9967. DOI: 10.1002/cne.902020212.

[25] R. Matsuzaki and S. Kyuhou. ‘‘Pontine neurons which relay projections from the superior colliculus to the posterior vermis of the cerebellum in the cat: distribution and visual properties’’. eng. In: *Neuroscience Letters* 236.2 (Oct. 1997), pp. 99–102. ISSN: 0304-3940. DOI: 10.1016/s0304-3940(97)00779-9.

[26] Tsutomu Hashikawa and Koki Kawamura. ‘‘Identification of cells of origin of tectopontine fibers in the cat superior colliculus: An experimental study with the horseradish peroxidase method’’. en. In: *Brain Research* 130.1 (July 1977), pp. 65–79. ISSN: 00068993. DOI: 10.1016/0006-8993(77)90842-3. URL: https://linkinghub.elsevier.com/retrieve/pii/0006899377908423.

[27] Koki Kawamura. ‘‘The pontine projection from the inferior colliculus in the cat. An experimental anatomical study’’. en. In: *Brain Research* 95.2-3 (Sept. 1975), pp. 309–322. ISSN: 00068993. DOI: 10.1016/0006-8993(75)90109-2. URL: https://linkinghub.elsevier.com/retrieve/pii/0006899375901092.

[28] R S Swenson and A J Castro. *THE AFFERENT CONNECTIONS OF THE INFERIOR OLIVARY COMPLEX IN RATS. AN ANTEROGRADE STUDY USING AUTORADIOGRAPHIC AND AXONAL DEGENERATION TECHNIQUES*. Tech. rep. 2. 1983, pp. 259–275.

[29] Xue Liu et al. ‘‘The Superior Colliculus: Cell Types, Connectivity, and Behavior’’. eng. In: *Neuroscience Bulletin* 38.12 (Dec. 2022), pp. 1519–1540. ISSN: 1995-8218. DOI: 10.1007/s12264-022-00858-1.

[30] Motoi Kudo et al. ‘‘Direct projections to the pretectum and the midbrain reticular formation from auditory relay nuclei in the lower brainstem of the cat’’. en. In: *Brain Research* 288.1-2 (Dec. 1983), pp. 13–19. ISSN: 00068993. DOI: 10.1016/0006-8993(83)90077-X. URL: https://linkinghub.elsevier.com/retrieve/pii/000689938390077X.

[31] Peter Redgrave et al. ‘‘Interactions between the Midbrain Superior Colliculus and the Basal Ganglia’’. English. In: *Frontiers in Neuroanatomy* 4 (Sept. 2010). ISSN: 1662-5129. DOI: 10.3389/fnana.2010.00132. URL: https://www.frontiersin.org/journals/neuroanatomy/articles/10.3389/fnana.2010.00132/full.

[32] Eliane Comoli et al. ‘‘A direct projection from superior colliculus to substantia nigra for detecting salient visual events’’. eng. In: *Nature Neuroscience* 6.9 (Sept. 2003), pp. 974–980. ISSN: 1097-6256. DOI: 10.1038/nn1113.

[33] G. D. Partlow, M. Colonnier, and J. Szabo. ‘‘Thalamic projections of the superior colliculus in the rhesus monkey, Macaca mulatta. A light and electron microscopic study’’. eng. In: *The Journal of Comparative Neurology* 72.3 (Feb. 1977), pp. 285–318. ISSN: 0021-9967. DOI: 10.1002/cne.901710302.

[34] Samuel D. Gale and Gabe J. Murphy. ‘‘Distinct cell types in the superficial superior colliculus project to the dorsal lateral geniculate and lateral posterior thalamic nuclei’’. en. In: *Journal of Neurophysiology* 120.3 (Sept. 2018), pp. 1286–1292. ISSN: 0022-3077, 1522-1598. DOI: 10.1152/jn.00248.2018. URL: https://www.physiology.org/doi/10.1152/jn.00248.2018.

[35] Brett R. Schofield, Jeffrey G. Mellott, and Susan D. Motts. ‘‘Subcollicular projections to the auditory thalamus and collateral projections to the inferior colliculus’’. In: *Frontiers in Neuroanatomy* 8 (July 2014). ISSN: 1662-5129. DOI: 10.3389/fnana.2014.00070. URL: http://journal.frontiersin.org/article/10.3389/fnana.2014.00070/abstract.

[36] J. K. Harting et al. ‘‘Neuroanatomical studies of the nigrotectal projection in the cat’’. eng. In: *The Journal of Comparative Neurology* 278.4 (Dec. 1988), pp. 615–631. ISSN: 0021-9967. DOI: 10.1002/cne.902780412.

[37] Zheng Zhou et al. ‘‘A VTA GABAergic Neural Circuit Mediates Visually Evoked Innate Defensive Responses’’. en. In: *Neuron* 103.3 (Aug. 2019), 473–488.e6. ISSN: 08966273. DOI: 10.1016/j.neuron.2019.05.027. URL: https://linkinghub.elsevier.com/retrieve/pii/S0896627319304805.

[38] A. J. Beitz et al. ‘‘Differential origin of brainstem serotoninergic projections to the midbrain periaqueductal gray and superior colliculus of the rat’’. eng. In: *The Journal of Comparative Neurology* 250.4 (Aug. 1986), pp. 498–509. ISSN: 0021-9967. DOI: 10.1002/cne.902500408.

[39] S T Meller and B J Denntst. *EFFERENT PROJECTIONS OF THE PERIAQUEDUCTAL GRAY IN THE RABBIT*. Tech. rep. 1. 1991, pp. 191–216.

[40] V V Stezhka and T A Lovick. *Projections from dorsal raphe nucleus to the periaqueductal grey matter: studies in slices of rat midbrain maintained in vitro*. Tech. rep. 1997.

[41] M. T. Stechison, J. A. Saint-Cyr, and S. J. Spence. ‘‘Projections from the nuclei prepositus hypoglossi and intercalatus to the superior colliculus in the cat: an anatomical study using WGA-HRP’’. en. In:

Experimental Brain Research 59.1 (June 1985), pp. 139–150. ISSN: 1432-1106. DOI: 10.1007/BF00237674. URL: https://doi.org/10.1007/BF00237674.

[42] Eddie Perkins, Susan Warren, and Paul J. May. ‘‘The Mesencephalic Reticular Formation as a Conduit for Primate Collicular Gaze Control: Tectal Inputs to Neurons Targeting the Spinal Cord and Medulla’’. en. In: *The Anatomical Record* 292.8 (Aug. 2009), pp. 1162–1181. ISSN: 1932-8486, 1932-8494. DOI: 10.1002/ar.20935. URL: https://anatomypubs.onlinelibrary.wiley.com/doi/10.1002/ar.20935.

[43] Vinod Jangir Kumar, Klaus Scheffler, and Wolfgang Grodd. ‘‘The structural connectivity mapping of the intralaminar thalamic nuclei’’. en. In: *Scientific Reports* 13.1 (July 2023), p. 11938. ISSN: 2045-2322. DOI: 10.1038/s41598-023-38967-0. URL: https://www.nature.com/articles/s41598-023-38967-0.

[44] Karl E. Krout et al. ‘‘Superior colliculus projections to midline and intralaminar thalamic nuclei of the rat’’. In: *The Journal of Comparative Neurology* 431.2 (2001), p. 198. ISSN: 0021-9967. DOI: 10.1002/1096-9861(20010305)431:2<198::AID-CNE1065>3.0.CO;2-8. URL: https://www.academia.edu/48744656/Superior_colliculus_projections_to_midline_and_intralaminar_thalamic_nuclei_of_the_rat.

[45] A. Tortelly and F. Reinoso-Suárez. ‘‘Projections to the superior colliculus from the dorsal hypothalamic area and other prosencephalic structures derived from the embryonic subthalamic longitudinal band of the diencephalon’’. eng. In: *Neuroscience Letters* 18.3 (July 1980), pp. 257–260. ISSN: 0304-3940. DOI: 10.1016/0304-3940(80)90294-3.

[46] Claudius F. Kratochwil, Upasana Maheshwari, and Filippo M. Rijli. ‘‘The Long Journey of Pontine Nuclei Neurons: From Rhombic Lip to Cortico-Ponto-Cerebellar Circuitry’’. In: *Frontiers in Neural Circuits* 11 (May 2017), p. 33. ISSN: 1662-5110. DOI: 10.3389/fncir.2017.00033. URL: http://journal.frontiersin.org/article/10.3389/fncir.2017.00033/full.

[47] Duane E Haines. ‘‘Neuroanatomy in Clinical Context: An Atlas of Structures, Sections, Systems, and Syndromes, 9th Edition’’. en. In: ().

[48] Hao Liu and Gregory A. Mihailoff. ‘‘Hypothalamopontine projections in the rat: Anterograde axonal transport studies utilizing light and electron microscopy’’. en. In: *The Anatomical Record* 255.4 (Aug. 1999), pp. 428–451. ISSN: 0003-276X, 1097-0185. DOI: 10.1002/(SICI)1097-0185(19990801)255:4<428::AID-AR9>3.0.CO;2-S. URL: https://onlinelibrary.wiley.com/doi/10.1002/(SICI)1097-0185(19990801)255:4%3C428::AID-AR9%3E3.0.CO;2-S.

[49] Hunter E. Halverson and John H. Freeman. ‘‘Ventral lateral geniculate input to the medial pons is necessary for visual eyeblink conditioning in rats’’. In: *Learning & Memory* 17.2 (Feb. 2010), pp. 80–85. ISSN: 1072-0502. DOI: 10.1101/lm.1572710. URL: https://pmc.ncbi.nlm.nih.gov/articles/PMC2825698/.

[50] Ramakrishnan Bhuvanasundaram, Joanna Krzyspiak, and Kamran Khodakhah. ‘‘Subthalamic Nucleus Modulation of the Pontine Nuclei and Its Targeting of the Cerebellar Cortex’’. en. In: *The Journal of Neuroscience* 42.28 (July 2022), pp. 5538–5551. ISSN: 0270-6474, 1529-2401. DOI: 10.1523/JNEUROSCI.2388-19.2022. URL: https://www.jneurosci.org/lookup/doi/10.1523/JNEUROSCI.2388-19.2022.

[51] Manika S. Paul and Joe M. Das. ‘‘Neuroanatomy, Superior and Inferior Olivary Nucleus (Superior and Inferior Olivary Complex)’’. eng. In: *StatPearls*. Treasure Island (FL): StatPearls Publishing, 2026. URL: http://www.ncbi.nlm.nih.gov/books/NBK542242/.

[52] Alberto Cacciola et al. ‘‘The cortico-rubral and cerebello-rubral pathways are topographically organized within the human red nucleus’’. In: *Scientific Reports* 9.1 (2019), p. 12117. ISSN: 2045-2322. DOI: 10.1038/s41598-019-48164-7. URL: https://doi.org/10.1038/s41598-019-48164-7.

[53] Josef Turecek and Wade G. Regehr. ‘‘Cerebellar and vestibular nuclear synapses in the inferior olive have distinct release kinetics and neurotransmitters’’. eng. In: *eLife* 9 (Dec. 2020), e61672. ISSN: 2050-084X. DOI: 10.7554/eLife.61672.

[54] Ramakrishnan Bhuvanasundaram et al. ‘‘Zona incerta modulation of the inferior olive and the pontine nuclei’’. In: *Network Neuroscience* 8.1 (Apr. 2024), pp. 260–274. ISSN: 2472-1751. DOI: 10.1162/netn_a_00350. URL: https://doi.org/10.1162/netn_a_00350.

[55] F. Walberg. ‘‘Olivary afferents from the brain stem reticular formation’’. en. In: *Experimental Brain Research* 47.1 (July 1982). ISSN: 0014-4819, 1432-1106. DOI: 10.1007/BF00235894. URL: http://link.springer.com/10.1007/BF00235894.

[56] Niping Wang et al. ‘‘Reticular Formation Connections Underlying Horizontal Gaze: The Central Mesencephalic Reticular Formation (cMRF) as a Conduit for the Collicular Saccade Signal’’. In: *Frontiers in Neuroanatomy* 11 (Apr. 2017), p. 36. ISSN: 1662-5129. DOI: 10.3389/fnana.2017.00036. URL: http://journal.frontiersin.org/article/10.3389/fnana.2017.00036/full.

[57] Grethe Hellstrøm Hoddevik, Alf Brodal, and Fred Walberg. ‘‘The reticulovestibular projection in the cat. An experimental study with silver impregnation methods’’. In: *Brain Research* 94.3 (1975), pp. 383–399. ISSN: 0006-8993. DOI: https://doi.org/10.1016/0006-8993(75)90224-3. URL: https://www.sciencedirect.com/science/article/pii/0006899375902243.

[58] B. W. Peterson and C. Abzug. ‘‘Properties of projections from vestibular nuclei to medial reticular formation in the cat’’. In: *Journal of Neurophysiology* 38.6 (Nov. 1975), pp. 1421–1435. ISSN: 0022-3077. DOI: 10.1152/jn.1975.38.6.1421. URL: https://journals.physiology.org/doi/abs/10.1152/jn.1975.38.6.1421.

[59] A. J. Tellegen, J. J. Arends, and J. L. Dubbeldam. ‘‘The vestibular nuclei and vestibuloreticular connections in the mallard (Anas platyrhynchos L.). An anterograde and retrograde tracing study’’. eng. In: *Brain, Behavior and Evolution* 58.4 (2001), pp. 205–217. ISSN: 0006-8977. DOI: 10.1159/000057564.

[60] G. R. Holstein et al. ‘‘Direct projections from the caudal vestibular nuclei to the ventrolateral medulla in the rat’’. eng. In: *Neuroscience* 175 (Feb. 2011), pp. 104–117. ISSN: 1873-7544. DOI: 10.1016/j.neuroscience.2010.12.011.

[61] Donna L. Gruol et al., eds. *Essentials of Cerebellum and Cerebellar Disorders*. en. Cham: Springer International Publishing, 2016. ISBN: 978-3-319-24549-2 978-3-319-24551-5. DOI: 10.1007/978-3-319-24551-5. URL: http://link.springer.com/10.1007/978-3-319-24551-5.

[62] T. Shiroyama et al. ‘‘Projections of the vestibular nuclei to the thalamus in the rat: a Phaseolus vulgaris leucoagglutinin study’’. eng. In: *The Journal of Comparative Neurology* 407.3 (Dec. 1999), pp. 318–332. ISSN: 0021-9967.

[63] Françoise Condé and Hendi Condé. ‘‘Thalamic projections of the vestibular nuclei in the cat as revealed by retrograde transport of horseradish peroxidase’’. In: *Neuroscience Letters* 9.2 (Sept. 1978), pp. 141–146. ISSN: 0304-3940. DOI: 10.1016/0304-3940(78)90062-9. URL: https://www.sciencedirect.com/science/article/pii/0304394078900629.

[64] Rajiv Wijesinghe, Dario A. Protti, and Aaron J. Camp. ‘‘Vestibular Interactions in the Thalamus’’. In: *Frontiers in Neural Circuits* 9 (Dec. 2015), p. 79. ISSN: 1662-5110. DOI: 10.3389/fncir.2015.00079. URL: https://pmc.ncbi.nlm.nih.gov/articles/PMC4667082/.

[65] S.J. Fung et al. ‘‘Differential labeling of the vestibular complex following unilateral injections of horseradish peroxidase into the cat and rat locus coeruleus’’. en. In: *Brain Research* 401.2 (Jan. 1987), pp. 347–352. ISSN: 00068993. DOI: 10.1016/0006-8993(87)91419-3. URL: https://linkinghub.elsevier.com/retrieve/pii/0006899387914193.

[66] Kavita Singh et al. ‘‘Structural connectivity of autonomic, pain, limbic, and sensory brainstem nuclei in living humans based on 7 Tesla and 3 Tesla MRI’’. en. In: *Human Brain Mapping* 43.10 (July 2022), pp. 3086–3112. ISSN: 1065-9471, 1097-0193. DOI: 10.1002/hbm.25836. URL: https://onlinelibrary.wiley.com/doi/10.1002/hbm.25836.

[67] Simone Cauzzo et al. ‘‘Functional connectome of brainstem nuclei involved in autonomic, limbic, pain and sensory processing in living humans from 7 Tesla resting state fMRI’’. en. In: *NeuroImage* 250 (Apr. 2022), p. 118925. ISSN: 10538119. DOI: 10.1016/j.neuroimage.2022.118925. URL: https://linkinghub.elsevier.com/retrieve/pii/S1053811922000544.

[68] Steven C Carleton and Malcolm B Carpenter. ‘‘Afferent and efferent connections of the medial, inferior and lateral vestibular nuclei in the cat and monkey’’. In: *Brain Research* 278.1 (1983), pp. 29–51. ISSN:

0006-8993. DOI: https://doi.org/10.1016/0006-8993(83)90223-8. URL: https://www.sciencedirect.com/science/article/pii/0006899383902238.

[69] Juichi Ito et al. ''Commissural and ipsilateral internuclear connection of vestibular nuclear complex of the cat''. In: *Brain Research* 341.1 (1985), pp. 73–81. ISSN: 0006-8993. DOI: https://doi.org/10.1016/0006-8993(85)91474-X. URL: https://www.sciencedirect.com/science/article/pii/000689938591474X.

[70] M B Carpenter. ''Chapter 1 Vestibular nuclei: afferent and efferent projections''. In: *Progress in Brain Research*. Ed. by O Pompeiano and J H J Allum. Vol. 76. Elsevier, 1988, pp. 5–15. ISBN: 0079-6123. DOI: https://doi.org/10.1016/S0079-6123(08)64487-8. URL: https://www.sciencedirect.com/science/article/pii/S0079612308644878.

[71] S.J. Shammah-Lagnado et al. ''Afferent connections of the mesencephalic reticular formation: A horseradish peroxidase study in the rat''. en. In: *Neuroscience* 9.2 (June 1983), pp. 391–409. ISSN: 03064522. DOI: 10.1016/0306-4522(83)90302-0. URL: https://linkinghub.elsevier.com/retrieve/pii/0306452283903020.

[72] Marie-Francoise Chesselet. ''Mapping the Basal Ganglia''. en. In: *Brain Mapping: The Systems*. Elsevier, 2000, pp. 177–206. ISBN: 978-0-12-692545-6. DOI: 10.1016/B978-012692545-6/50009-X. URL: https://linkinghub.elsevier.com/retrieve/pii/B978012692545650009X.

[73] Ysbrand D. Van der Werf, Menno P. Witter, and Henk J. Groenewegen. ''The intralaminar and midline nuclei of the thalamus. Anatomical and functional evidence for participation in processes of arousal and awareness''. eng. In: *Brain Research. Brain Research Reviews* 39.2-3 (Sept. 2002), pp. 107–140. DOI: 10.1016/s0165-0173(02)00181-9.

[74] Robert P. Vertes and George F. Martin. ''Autoradiographic analysis of ascending projections from the pontine and mesencephalic reticular formation and the median raphe nucleus in the rat''. en. In: *Journal of Comparative Neurology* 275.4 (Sept. 1988), pp. 511–541. ISSN: 0021-9967, 1096-9861. DOI: 10.1002/cne.902750404. URL: https://onlinelibrary.wiley.com/doi/10.1002/cne.902750404.

[75] Harold H. Traurig. ''The Brain Stem Reticular Formation''. en. In: *Neuroscience in Medicine*. Ed. by P. Michael Conn. Totowa, NJ: Humana Press, 2008, pp. 273–286. ISBN: 978-1-60327-455-5. DOI: 10.1007/978-1-60327-455-5_17. URL: https://doi.org/10.1007/978-1-60327-455-5_17.

[76] Barbara E. Jones. ''Neurobiology of waking and sleeping''. en. In: *Handbook of Clinical Neurology*. Vol. 98. Elsevier, 2011, pp. 131–149. ISBN: 978-0-444-52006-7. DOI: 10.1016/B978-0-444-52006-7.00009-5. URL: https://linkinghub.elsevier.com/retrieve/pii/B9780444520067000095.

[77] A. Robbins, S. Schwartz-Giblin, and D.W. Pfaff. ''Ascending and descending projections to medullary reticular formation sites which activate deep lumbar hack muscles in the rat''. en. In: *Experimental Brain Research* 80.3 (May 1990). ISSN: 0014-4819, 1432-1106. DOI: 10.1007/BF00227988. URL: http://link.springer.com/10.1007/BF00227988.

[78] Lauren E McElvain et al. ''Specific populations of basal ganglia output neurons target distinct brain stem areas while collateralizing throughout the diencephalon''. In: *Neuron* 109.10 (2021), pp. 1721–1738. ISSN: 0896-6273. DOI: https://doi.org/10.1016/j.neuron.2021.03.017. URL: https://www.sciencedirect.com/science/article/pii/S0896627321001872.

[79] Nicolás A. Morgenstern and Maria S. Esposito. ''The Basal Ganglia and Mesencephalic Locomotor Region Connectivity Matrix''. In: *Current Neuropharmacology* 22.9 (2024), pp. 1454–1472. ISSN: 1570-159X. DOI: 10.2174/1570159X21666230809112840. URL: https://pmc.ncbi.nlm.nih.gov/articles/PMC11097982/.

[80] K. Takakusaki et al. ''Basal ganglia efferents to the brainstem centers controlling postural muscle tone and locomotion: a new concept for understanding motor disorders in basal ganglia dysfunction''. en. In: *Neuroscience* 119.1 (June 2003), pp. 293–308. ISSN: 03064522. DOI: 10.1016/S0306-4522(03)00095-2. URL: https://linkinghub.elsevier.com/retrieve/pii/S0306452203000952.

[81] Simon J. Fung et al. ''Projection neurons from the central nucleus of the amygdala to the nucleus pontis oralis''. en. In: *Journal of Neuroscience Research* 89.3 (Mar. 2011), pp. 429–436. ISSN: 03604012. DOI: 10.1002/jnr.22554. URL: https://onlinelibrary.wiley.com/doi/10.1002/jnr.22554.

[82] Jared M. Cregg et al. ‘‘Basal ganglia–spinal cord pathway that commands locomotor gait asymmetries in mice’’. en. In: *Nature Neuroscience* 27.4 (Apr. 2024), pp. 716–727. ISSN: 1097-6256, 1546-1726. DOI: 10.1038/s41593-024-01569-8. URL: https://www.nature.com/articles/s41593-024-01569-8.

[83] P. W. Mantyh. ‘‘Connections of midbrain periaqueductal gray in the monkey. II. Descending efferent projections’’. en. In: *Journal of Neurophysiology* 49.3 (Mar. 1983), pp. 582–594. ISSN: 0022-3077, 1522-1598. DOI: 10.1152/jn.1983.49.3.582. URL: https://www.physiology.org/doi/10.1152/jn.1983.49.3.582.

[84] Cristian González-Cabrera et al. *A VTA-pontine GABA pathway biases backward locomotion via local and distal inhibition*. en. Feb. 2026. DOI: 10.64898/2026.02.17.706301. URL: http://biorxiv.org/lookup/doi/10.64898/2026.02.17.706301.

[85] Nikolaus R. McFarland and Suzanne N. Haber. ‘‘Thalamic Relay Nuclei of the Basal Ganglia Form Both Reciprocal and Nonreciprocal Cortical Connections, Linking Multiple Frontal Cortical Areas’’. en. In: *The Journal of Neuroscience* 22.18 (Sept. 2002), pp. 8117–8132. ISSN: 0270-6474, 1529-2401. DOI: 10.1523/JNEUROSCI.22-18-08117.2002. URL: https://www.jneurosci.org/lookup/doi/10.1523/JNEUROSCI.22-18-08117.2002.

[86] Carmen Alonso-Martínez et al. ‘‘Cerebellar and basal ganglia inputs define three main nuclei in the mouse ventral motor thalamus’’. In: *Frontiers in Neuroanatomy* 17 (Aug. 2023), p. 1242839. ISSN: 1662-5129. DOI: 10.3389/fnana.2023.1242839. URL: https://www.frontiersin.org/articles/10.3389/fnana.2023.1242839/full.

[87] A J Beitz. ‘‘The organization of afferent projections to the midbrain periaqueductal gray of the rat’’. In: *Neuroscience* 7 (Jan. 1982), pp. 133–159.

[88] Robert M Beckstead, Valerie B Domesick, and Walle J H Nauta. ‘‘Efferent connections of the substantia nigra and ventral tegmental area in the rat’’. In: *Brain Research* 175.2 (1979), pp. 191–217. ISSN: 0006-8993. DOI: https://doi.org/10.1016/0006-8993(79)91001-1. URL: https://www.sciencedirect.com/science/article/pii/0006899379910011.

[89] Carolina Cebrián, André Parent, and Lucía Prensa. ‘‘Patterns of axonal branching of neurons of the substantia nigra pars reticulata and pars lateralis in the rat’’. en. In: *Journal of Comparative Neurology* 492.3 (Nov. 2005), pp. 349–369. ISSN: 0021-9967, 1096-9861. DOI: 10.1002/cne.20741. URL: https://onlinelibrary.wiley.com/doi/10.1002/cne.20741.

[90] Susan R Sesack and Anthony A Grace. ‘‘Cortico-Basal Ganglia Reward Network: Microcircuitry’’. en. In: *Neuropsychopharmacology* 35.1 (Jan. 2010), pp. 27–47. ISSN: 0893-133X, 1740-634X. DOI: 10.1038/npp.2009.93. URL: https://www.nature.com/articles/npp200993.

[91] Juarez A. Ricardo. ‘‘Efferent connections of the subthalamic region in the rat. I. The subthalamic nucleus of luys’’. en. In: *Brain Research* 202.2 (Dec. 1980), pp. 257–271. ISSN: 00068993. DOI: 10.1016/0006-8993(80)90140-7. URL: https://linkinghub.elsevier.com/retrieve/pii/0006899380901407.

[92] A.J. Mcdonald. ‘‘Topographical organization of amygdaloid projections to the caudatoputamen, nucleus accumbens, and related striatal-like areas of the rat brain’’. en. In: *Neuroscience* 44.1 (Jan. 1991), pp. 15–33. ISSN: 03064522. DOI: 10.1016/0306-4522(91)90248-M. URL: https://linkinghub.elsevier.com/retrieve/pii/030645229190248M.

[93] Elena Borra et al. ‘‘Involvement of the claustrum in the cortico-basal ganglia circuitry: connectional study in the non-human primate’’. en. In: *Brain Structure and Function* 229.5 (Apr. 2024), pp. 1143–1164. ISSN: 1863-2661. DOI: 10.1007/s00429-024-02784-6. URL: https://link.springer.com/10.1007/s00429-024-02784-6.

[94] Stephen T Mason and Hans C Fibiger. ‘‘Regional topography within noradrenergic locus coeruleus as revealed by retrograde transport of horseradish peroxidase’’. In: *Journal of Comparative Neurology* 187.4 (Oct. 1979), pp. 703–724. ISSN: 0021-9967. DOI: https://doi.org/10.1002/cne.901870405. URL: https://doi.org/10.1002/cne.901870405.

[95] J.-P Adèr et al. *Bilaterally Diverging Axon Collaterals and Contralateral Projections from Rat Locus Coeruleus Neurons, Demonstrated by Fluorescent Retrograde Double Labeling and Norepinephrine Metabolism*. Tech. rep. 1980, pp. 207–218.

[96] Ke Deng et al. ''Whole-brain mapping of projection from mice lateral septal nucleus''. en. In: *Biology Open* (Jan. 2019), bio.043554. ISSN: 2046-6390. DOI: 10.1242/bio.043554. URL: https://journals.biologists.com/bio/article/doi/10.1242/bio.043554/258512/Whole-brain-mapping-of-projection-from-mice.

[97] Jennifer Isaac et al. ''Organization of Brainwide Inputs to Discrete Lateral Septum Projection Populations''. en. In: *The Journal of Neuroscience* 45.37 (Sept. 2025), e0797252025. ISSN: 0270-6474, 1529-2401. DOI: 10.1523/JNEUROSCI.0797-25.2025. URL: https://www.jneurosci.org/lookup/doi/10.1523/JNEUROSCI.0797-25.2025.

[98] Mei Hao et al. ''Neural Circuit Connections and Functions of Locus Coeruleus–Norepinephrine System''. en. In: *International Journal of Molecular Sciences* 26.22 (Nov. 2025), p. 11163. ISSN: 1422-0067. DOI: 10.3390/ijms262211163. URL: https://www.mdpi.com/1422-0067/26/22/11163.

[99] Gabriel S. Rocha et al. ''Basal ganglia for beginners: the basic concepts you need to know and their role in movement control''. In: *Frontiers in Systems Neuroscience* 17 (Aug. 2023), p. 1242929. ISSN: 1662-5137. DOI: 10.3389/fnsys.2023.1242929. URL: https://www.frontiersin.org/articles/10.3389/fnsys.2023.1242929/full.

[100] Connor D. Courtney, Arin Pamukcu, and C. Savio Chan. ''Cell and circuit complexity of the external globus pallidus''. en. In: *Nature Neuroscience* 26.7 (July 2023), pp. 1147–1159. ISSN: 1097-6256, 1546-1726. DOI: 10.1038/s41593-023-01368-7. URL: https://www.nature.com/articles/s41593-023-01368-7.

[101] D Joel and I Weiner. ''The connections of the primate subthalamic nucleus: indirect pathways and the open-interconnected scheme of basal ganglia-thalamocortical circuitry''. en. In: *Brain Research Reviews* 23.1-2 (Feb. 1997), pp. 62–78. ISSN: 01650173. DOI: 10.1016/S0165-0173(96)00018-5. URL: https://linkinghub.elsevier.com/retrieve/pii/S0165017396000185.

[102] Bao N. T. Hoang et al. ''Topographic organisation of the claustrum–amygdala–prefrontal circuitry in the common marmoset (Callithrix jacchus)''. en. In: *Brain Structure and Function* 230.9 (Nov. 2025), p. 176. ISSN: 1863-2661. DOI: 10.1007/s00429-025-03026-z. URL: https://link.springer.com/10.1007/s00429-025-03026-z.

[103] V RajMohan and E Mohandas. ''The limbic system''. en. In: *Indian Journal of Psychiatry* 49.2 (2007), p. 132. ISSN: 0019-5545. DOI: 10.4103/0019-5545.33264. URL: https://journals.lww.com/10.4103/0019-5545.33264.

[104] Tilat A. Rizvi et al. ''Connections between the central nucleus of the amygdala and the midbrain periaqueductal gray: Topography and reciprocity''. en. In: *Journal of Comparative Neurology* 303.1 (Jan. 1991), pp. 121–131. ISSN: 0021-9967, 1096-9861. DOI: 10.1002/cne.903030111. URL: https://onlinelibrary.wiley.com/doi/10.1002/cne.903030111.

[105] Daniel S. Zahm et al. ''Direct comparison of projections from the central amygdaloid region and nucleus accumbens shell''. en. In: *European Journal of Neuroscience* 11.4 (Apr. 1999), pp. 1119–1126. ISSN: 0953-816X, 1460-9568. DOI: 10.1046/j.1460-9568.1999.00524.x. URL: https://onlinelibrary.wiley.com/doi/10.1046/j.1460-9568.1999.00524.x.

[106] P.-H. Luppi et al. ''Afferent projections to the rat locus coeruleus demonstrated by retrograde and anterograde tracing with cholera-toxin B subunit and Phaseolus vulgaris leucoagglutinin''. In: *Neuroscience* 65.1 (1995), pp. 119–160. ISSN: 0306-4522. DOI: https://doi.org/10.1016/0306-4522(94)00481-J. URL: https://www.sciencedirect.com/science/article/pii/030645229400481J.

[107] O T Phillipson. ''Afferent projections to the ventral tegmental area of Tsai and interfascicular nucleus: A horseradish peroxidase study in the rat''. In: *Journal of Comparative Neurology* 187.1 (Sept. 1979), pp. 117–143. ISSN: 0021-9967. DOI: https://doi.org/10.1002/cne.901870108. URL: https://doi.org/10.1002/cne.901870108.

[108] F.-J. Chen and S.J. Sara. ‘‘Locus coeruleus activation by foot shock or electrical stimulation inhibits amygdala neurons’’. en. In: *Neuroscience* 144.2 (Jan. 2007), pp. 472–481. ISSN: 03064522. DOI: 10.1016/j.neuroscience.2006.09.037. URL: https://linkinghub.elsevier.com/retrieve/pii/S0306452206013017.

[109] Esther Asan. *The Catecholaminergic Innervation of the Rat Amygdala*. Ed. by F. Beck et al. Vol. 142. Advances in Anatomy Embryology and Cell Biology. Berlin, Heidelberg: Springer Berlin Heidelberg, 1998. ISBN: 978-3-540-63903-9 978-3-642-72085-7. DOI: 10.1007/978-3-642-72085-7. URL: http://link.springer.com/10.1007/978-3-642-72085-7.

[110] Wei Tang et al. *Dopamine in the basal amygdala signals salient somatosensory events during fear learning*. en. July 2019. DOI: 10.1101/716589. URL: http://biorxiv.org/lookup/doi/10.1101/716589.

[111] Mei Hao et al. *Neural Circuit Connections and Functions of Locus Coeruleus–Norepinephrine System*. Nov. 2025. DOI: 10.3390/ijms262211163.

[112] Shaoshan Wang et al. ‘‘Dopaminergic neurons in the ventral periaqueductal gray projecting to the dorsal lateral septum regulate comorbid pain and anxiety’’. en. In: *Brain Research Bulletin* 228 (Aug. 2025), p. 111409. ISSN: 03619230. DOI: 10.1016/j.brainresbull.2025.111409. URL: https://linkinghub.elsevier.com/retrieve/pii/S0361923025002217.

[113] Qian Zhang et al. ‘‘Locus Coeruleus-Dorsolateral Septum Projections Modulate Depression-Like Behaviors via BDNF But Not Norepinephrine’’. en. In: *Advanced Science* 11.10 (Mar. 2024), p. 2303503. ISSN: 2198-3844, 2198-3844. DOI: 10.1002/advs.202303503. URL: https://advanced.onlinelibrary.wiley.com/doi/10.1002/advs.202303503.

[114] Barbara W. Adams and Bita Moghaddam. ‘‘Tactile stimulation activates dopamine release in the lateral septum’’. en. In: *Brain Research* 858.1 (Mar. 2000), pp. 177–180. ISSN: 00068993. DOI: 10.1016/S0006-8993(99)02473-7. URL: https://linkinghub.elsevier.com/retrieve/pii/S0006899399024737.

[115] Karl E. Krout, Rebecca E. Belzer, and Arthur D. Loewy. ‘‘Brainstem projections to midline and intralaminar thalamic nuclei of the rat’’. en. In: *Journal of Comparative Neurology* 448.1 (June 2002), pp. 53–101. ISSN: 0021-9967, 1096-9861. DOI: 10.1002/cne.10236. URL: https://onlinelibrary.wiley.com/doi/10.1002/cne.10236.

[116] L.F. Kromer and R.Y. Moore. ‘‘A study of the organization of the locus coeruleus projections to the lateral geniculate nuclei in the albino rat’’. en. In: *Neuroscience* 5.2 (Feb. 1980), pp. 255–271. ISSN: 03064522. DOI: 10.1016/0306-4522(80)90102-5. URL: https://linkinghub.elsevier.com/retrieve/pii/0306452280901025.

[117] James Timothy McKenna and Robert P. Vertes. ‘‘Afferent projections to nucleus reuniens of the thalamus’’. en. In: *Journal of Comparative Neurology* 480.2 (Dec. 2004), pp. 115–142. ISSN: 0021-9967, 1096-9861. DOI: 10.1002/cne.20342. URL: https://onlinelibrary.wiley.com/doi/10.1002/cne.20342.

[118] F.M Semenenko and B.M Lumb. ‘‘Excitatory projections from the anterior hypothalamus to periaqueductal gray neurons that project to the medulla: a functional anatomical study’’. en. In: *Neuroscience* 94.1 (Sept. 1999), pp. 163–174. ISSN: 03064522. DOI: 10.1016/S0306-4522(99)00317-6. URL: https://linkinghub.elsevier.com/retrieve/pii/S0306452299003176.

[119] Beverly A. S. Reyes et al. ‘‘Hypothalamic projections to locus coeruleus neurons in rat brain’’. en. In: *European Journal of Neuroscience* 22.1 (July 2005), pp. 93–106. ISSN: 0953-816X, 1460-9568. DOI: 10.1111/j.1460-9568.2005.04197.x. URL: https://onlinelibrary.wiley.com/doi/10.1111/j.1460-9568.2005.04197.x.

[120] Susan M. Tyree and Luis De Lecea. ‘‘Lateral Hypothalamic Control of the Ventral Tegmental Area: Reward Evaluation and the Driving of Motivated Behavior’’. In: *Frontiers in Systems Neuroscience* 11 (July 2017), p. 50. ISSN: 1662-5137. DOI: 10.3389/fnsys.2017.00050. URL: http://journal.frontiersin.org/article/10.3389/fnsys.2017.00050/full.

[121] D.M.L. Vianna and M.L. Brandão. ‘‘Anatomical connections of the periaqueductal gray: specific neural substrates for different kinds of fear’’. en. In: *Brazilian Journal of Medical and Biological Research*

36.5 (May 2003), pp. 557–566. ISSN: 0100-879X. DOI: 10.1590/S0100-879X2003000500002. URL: http://www.scielo.br/scielo.php?script=sci_arttext&pid=S0100-879X2003000500002&lng=en&tlng=en.

[122] Filippo Sean Giorgi et al. ''The connections of Locus Coeruleus with hypothalamus: potential involvement in Alzheimer's disease''. en. In: *Journal of Neural Transmission* 128.5 (May 2021), pp. 589–613. ISSN: 0300-9564, 1435-1463. DOI: 10.1007/s00702-021-02338-8. URL: https://link.springer.com/10.1007/s00702-021-02338-8.

[123] Niels R. Ntamati et al. ''Periaqueductal efferents to dopamine and GABA neurons of the VTA''. eng. In: *PloS One* 13.1 (2018), e0190297. ISSN: 1932-6203. DOI: 10.1371/journal.pone.0190297.

[124] Susan T. Lubejko et al. ''Inputs to the locus coeruleus from the periaqueductal gray and rostroventral medulla shape opioid-mediated descending pain modulation''. en. In: *Science Advances* 10.17 (Apr. 2024), eadj9581. ISSN: 2375-2548. DOI: 10.1126/sciadv.adj9581. URL: https://www.science.org/doi/10.1126/sciadv.adj9581.

[125] Natalia Omelchenko and Susan R. Sesack. ''Periaqueductal gray afferents synapse onto dopamine and GABA neurons in the rat ventral tegmental area''. en. In: *Journal of Neuroscience Research* 88.5 (Apr. 2010), pp. 981–991. ISSN: 0360-4012, 1097-4547. DOI: 10.1002/jnr.22265. URL: https://onlinelibrary.wiley.com/doi/10.1002/jnr.22265.

[126] Erika K. Harding et al. ''Locus coeruleus microcircuitry processes periaqueductal gray inputs into distinct outputs for regulation of pain and anxiety''. en. In: *Cell Reports* 44.12 (Dec. 2025), p. 116699. ISSN: 22111247. DOI: 10.1016/j.celrep.2025.116699. URL: https://linkinghub.elsevier.com/retrieve/pii/S2211124725014718.

[127] Susan Y. Bookheimer et al. ''The Lifespan Human Connectome Project in Aging: An overview''. en. In: *NeuroImage* 185 (Jan. 2019), pp. 335–348. ISSN: 10538119. DOI: 10.1016/j.neuroimage.2018.10.009. URL: https://linkinghub.elsevier.com/retrieve/pii/S1053811918319682.

[128] Michael P. Harms et al. ''Extending the Human Connectome Project across ages: Imaging protocols for the Lifespan Development and Aging projects''. en. In: *NeuroImage* 183 (Dec. 2018), pp. 972–984. ISSN: 10538119. DOI: 10.1016/j.neuroimage.2018.09.060. URL: https://linkinghub.elsevier.com/retrieve/pii/S1053811918318652.

[129] Brian B. Avants et al. ''A reproducible evaluation of ANTs similarity metric performance in brain image registration''. en. In: *NeuroImage* 54.3 (Feb. 2011), pp. 2033–2044. ISSN: 10538119. DOI: 10.1016/j.neuroimage.2010.09.025. URL: https://linkinghub.elsevier.com/retrieve/pii/S1053811910012061.

[130] Marta Bianciardi et al. ''Toward an *In Vivo* Neuroimaging Template of Human Brainstem Nuclei of the Ascending Arousal, Autonomic, and Motor Systems''. en. In: *Brain Connectivity* 5.10 (Dec. 2015), pp. 597–607. ISSN: 2158-0014, 2158-0022. DOI: 10.1089/brain.2015.0347. URL: https://journals.sagepub.com/doi/full/10.1089/brain.2015.0347.

[131] María Guadalupe García-Gomar et al. ''In vivo structural connectome of arousal and motor brainstem nuclei by 7 Tesla and 3 Tesla MRI''. en. In: *Human Brain Mapping* 43.14 (Oct. 2022), pp. 4397–4421. ISSN: 1065-9471, 1097-0193. DOI: 10.1002/hbm.25962. URL: https://onlinelibrary.wiley.com/doi/10.1002/hbm.25962.

[132] Kurt G. Schilling et al. ''Limits to anatomical accuracy of diffusion tractography using modern approaches''. en. In: *NeuroImage* 185 (Jan. 2019), pp. 1–11. ISSN: 10538119. DOI: 10.1016/j.neuroimage.2018.10.029. URL: https://linkinghub.elsevier.com/retrieve/pii/S1053811918319888.

[133] Anand Venkatraman, Brian L. Edlow, and Mary Helen Immordino-Yang. ''The Brainstem in Emotion: A Review''. In: *Frontiers in Neuroanatomy* 11 (Mar. 2017). ISSN: 1662-5129. DOI: 10.3389/fnana.2017.00015. URL: http://journal.frontiersin.org/article/10.3389/fnana.2017.00015/full.

[134] Lindsay A. Schwarz and Liqun Luo. ''Organization of the Locus Coeruleus-Norepinephrine System''. en. In: *Current Biology* 25.21 (Nov. 2015), R1051–R1056. ISSN: 09609822. DOI: 10.1016/j.cub.2015.09.039. URL: https://linkinghub.elsevier.com/retrieve/pii/S0960982215011501.

[135] Brian L. Edlow et al. ‘‘Neuroanatomic connectivity of the human ascending arousal system critical to consciousness and its disorders’’. eng. In: *Journal of Neuropathology and Experimental Neurology* 71.6 (June 2012), pp. 531–546. ISSN: 1554-6578. DOI: 10.1097/NEN.0b013e3182588293.

[136] Marisela Morales and Elyssa B. Margolis. ‘‘Ventral tegmental area: cellular heterogeneity, connectivity and behaviour’’. en. In: *Nature Reviews Neuroscience* 18.2 (Feb. 2017), pp. 73–85. ISSN: 1471-003X, 1471-0048. DOI: 10.1038/nrn.2016.165. URL: https://www.nature.com/articles/nrn.2016.165.

[137] Eduardo E. Benarroch. ‘‘Periaqueductal gray: An interface for behavioral control’’. en. In: *Neurology* 78.3 (Jan. 2012), pp. 210–217. ISSN: 0028-3878, 1526-632X. DOI: 10.1212/WNL.0b013e31823fcdee. URL: https://www.neurology.org/doi/10.1212/WNL.0b013e31823fcdee.

[138] Martijn P. Van Den Heuvel and Olaf Sporns. ‘‘Rich-Club Organization of the Human Connectome’’. en. In: *The Journal of Neuroscience* 31.44 (Nov. 2011), pp. 15775–15786. ISSN: 0270-6474, 1529-2401. DOI: 10.1523/JNEUROSCI.3539-11.2011. URL: https://www.jneurosci.org/lookup/doi/10.1523/JNEUROSCI.3539-11.2011.

[139] Tim B. Dyrby, Laurent Petit, and Christian Beaulieu. ‘‘Rethinking tractography and neuroanatomy: does image resolution hold the key?’’ eng. In: *Brain Structure & Function* 230.8 (Oct. 2025), p. 163. ISSN: 1863-2661. DOI: 10.1007/s00429-025-03025-0.

[140] Robert E. Smith et al. ‘‘SIFT: Spherical-deconvolution informed filtering of tractograms’’. en. In: *NeuroImage* 67 (Feb. 2013), pp. 298–312. ISSN: 10538119. DOI: 10.1016/j.neuroimage.2012.11.049. URL: https://linkinghub.elsevier.com/retrieve/pii/S1053811912011615.

[141] Alessandro Daducci et al. ‘‘COMMIT: Convex Optimization Modeling for Microstructure Informed Tractography’’. In: *IEEE Transactions on Medical Imaging* 34.1 (Jan. 2015), pp. 246–257. ISSN: 0278-0062, 1558-254X. DOI: 10.1109/TMI.2014.2352414. URL: https://ieeexplore.ieee.org/document/6884830.

[142] Paula Sanz Leon et al. ‘‘The Virtual Brain: a simulator of primate brain network dynamics’’. In: *Frontiers in Neuroinformatics* 7 (2013). ISSN: 1662-5196. DOI: 10.3389/fninf.2013.00010. URL: http://journal.frontiersin.org/article/10.3389/fninf.2013.00010/abstract.